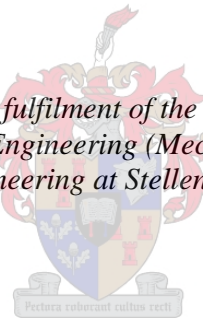


# Aiming strategies for small central receiver systems

by  
Annemarie Grobler

*Thesis presented in partial fulfilment of the requirements for the degree  
of Master of Engineering (Mechanical) in the  
Faculty of Engineering at Stellenbosch University*



Supervisors:  
Mr Paul Gauché  
Dr Willie Smit

March 2015

# Declaration

By submitting this thesis electronically, I declare that the entirety of the work contained therein is my own, original work, that I am the sole author thereof (save to the extent explicitly otherwise stated), that reproduction and publication thereof by Stellenbosch University will not infringe any third party rights and that I have not previously in its entirety or in part submitted it for obtaining any qualification.

Date: .....

Copyright © 2015 Stellenbosch University  
All rights reserved.

# Abstract

## **Aiming strategies for small central receiver systems**

A. Grobler

*Department of Mechanical Engineering  
Stellenbosch University  
Private Bag X1, 7602 Matieland, South Africa*

Thesis: MEng (Mech)

March 2015

Concentrating solar power as a sustainable energy technology is considered favourable in South Africa due to the high solar resource and the integration possibilities with the current electricity grid. Considering the various concentrating solar power technologies, the central receiver system is thought to be one of the most promising due to its high capacity factor and cost-efficient thermal storage capabilities.

These thermal systems are able to reach high temperatures (more than 1000 °C have been shown), and to obtain such temperatures, a high solar flux is required. This is achievable by aiming all of the heliostats at the centre of the target. High flux gradients over the receiver surface area and between the outer and inner surfaces of the receiver material can exist. These thermal gradients account for differences in temperatures on the receiver which result in thermal stresses leading to elastic and potentially plastic deformation of the material.

To eradicate the thermal stresses, the aim points of the heliostats can be managed such that the flux density distribution over the receiver aperture is decreased and homogenised. The primary objective of this thesis is to develop an aiming strategy specifically for small experimental heliostat fields. To reach this objective, a simulation platform was developed to model any heliostat field and receiver, and an analysis was conducted to compare analytical flux prediction methods to ray tracing.

At high incidence angles of between 30 ° and 60 °, the standard deviations of the circular Gaussian flux approximation methods were found to differ between approximately 10 % and 30 % from the ray traced results. A novel method, the Gaussian mixture model, was suggested and deviated less than 4 % from the ray traced results when considering the standard deviation of the flux profile.

Two basic aiming strategies were developed using the Tabu search and Genetic

algorithm optimisation methods. These two strategies make use of approximate method of flux prediction. Experiments were conducted to investigate static aiming strategies on physical systems and to identify factors that could have an effect on the experimental results. Finally a method of implementing the aiming strategy on a dynamic system was proposed.

By implementing both optimisation methods to complement each other, a new aiming strategy was developed that proved to provide better homogenisation of the flux distribution than either of the two methods alone. The accuracy of the final predicted flux distribution was improved by using the Gaussian mixture model as the flux distribution approximation method.

# Uittreksel

## Mikstrategieë vir klein sentrale ontvangerstelsels

*(“Aiming strategies for small central receiver systems”)*

A. Grobler

*Departement Meganiese Ingenieurswese  
Stellenbosch Universiteit  
Privaatsak X1, 7602 Matieland, Suid Afrika*

Tesis: MIng (Meg)

Maart 2015

Gekonsentreerde sonenergie as 'n hernubare energie bron, word in Suid-Afrika as uitvoerbaar beskou weens die hoë stralingsdigtheid asook die moontlikheid om hierdie tegnologie te koppel aan die huidige energienetwerk. As die verskeie gekonsentreerde sonenergie tegnologieë in ag geneem word, word sentrale ontvangerstelsels beskou as die mees belowende sonenergie konsep as gevolg van die hoë energie kapasiteit en die vermoë om termiese energie te stoor.

Hierdie termiese stelsels besit die vermoë om hoë temperature te bereik (meer as 1000 °C is al opgemerk), en om hierdie temperature te verkry word 'n hoë termiese vloed benodig. Dit is bereikbaar deur al die heliostate op die middel van die ontvanger te rig. Hoë termiese vloedgradiënte oor die oppervlakte van die opvanger en tussen die buite- en binne laag van die opvanger materiaal kan ontstaan. Termiese vloedgradiënte kan verskille in temperatuur op die ontvanger veroorsaak wat termiese spanning tot gevolg het kan lei tot elastiese en potensieel plastiese vervorming van die materiaal.

Om van die termiese spanning ontslae te raak kan die heliostate deur beheerstelsels na ander dele van die ontvanger gerig word om sodoende 'n laer en meer egalige termiese vloed oor die oppervlak van die ontvanger te verkry. Die hoofdoel van hierdie tesis is die ontwikkeling van 'n mikstrategie, hoofsaaklik bedoel vir klein eksperimentele heliostaatvelde. Om hierdie hoofdoel te bereik, was 'n simulasiplatform ontwikkel waardeur heliostaatvelde en opvangerstelsels gemodelleer kan word, en 'n analise is gedoen om die verskeidenheid benaderende analitiese metodes te vergelyk met die straalopsporingsmetode.

By hoë invalshoeke tussen 30 ° en 60 ° is daar gevind dat die benaderende modelle wat die termiese vloed as 'n normale Gaussiese verspreiding beskou, 'n afwyking

van die straalopsporingsresultate toon van ongeveer 10 % tot 30 %. 'n Nuwe metode, die Gaussiese mengsel model, was voorgestel en het minder as 4 % van die straalopsporings resultate afgewyk, met die standaard afwyking van die termiese vloed profiel in ag geneem.

Twee basiese mikstrategieë is ontwikkel deur gebruik te maak van die Tabu soek en Genetiese algoritme optimeringsmetodes. Hierdie strategieë maak gebruik van die benaderende metodes om termiese vloed te voorspel. Eksperimente is uitgevoer om die implementering van statiese mikstrategieë op 'n fisiese stelsel te beskou en die faktore wat 'n invloed op die eksperimentele resultate sal hê te identifiseer. Ten laaste word 'n metode voorgestel vir die implementering van die mikstrategieë op 'n dinamiese stelsel.

Deur beide optimeringsmetodes te implementeer sodat hul mekaar komplimenteer, word 'n nuwe mikstrategie ontwikkel wat beter homogenisering van die termiese vloed verspreiding bewys het as enige van die alleen staande metodes. Die akkuraatheid van die finale voorgestelde termiese vloed verspreiding was verbeter deur gebruik te maak van die Gaussiese mengsel model as die benaderende metode van die termiese vloed verspreiding.

# Acknowledgements

I would like to express my sincere gratitude to the following people and organisations who have contributed to making this work possible:

- My parents and siblings for encouraging me to live out my passion and giving me their love and support.
- Paul Gauché and Willie Smit as my study leaders for guiding me into becoming both a better researcher and engineer. I would also like to thank them for providing the resources which made this study possible.
- Willem Landman for being an excellent mentor and colleague.
- Jacques van den Munckhof, Sebastian Bode and Henk Laubscher for their assistance during the experimental setup.
- All my colleagues at STERG whom have uplifted my spirits and encouraged me to keep moving forward.
- SASOL for providing financial support.

# Dedications

*I dedicate this thesis to my Lord Jesus Christ in whom all things are possible.*

# Contents

<b>Declaration</b>	<b>i</b>
<b>Abstract</b>	<b>ii</b>
<b>Uittreksel</b>	<b>iv</b>
<b>Acknowledgements</b>	<b>vi</b>
<b>Dedications</b>	<b>vii</b>
<b>Contents</b>	<b>viii</b>
<b>List of Figures</b>	<b>xi</b>
<b>List of Tables</b>	<b>xv</b>
<b>Nomenclature</b>	<b>xvi</b>
<b>1 Introduction</b>	<b>1</b>
1.1 Background . . . . .	1
1.2 Motivation . . . . .	2
1.3 Research objectives . . . . .	4
1.4 Delineation and limitations . . . . .	4
1.5 Chapter overview . . . . .	5
<b>2 Literature Review</b>	<b>6</b>
2.1 Introduction . . . . .	6
2.2 Central receiver systems . . . . .	7
2.3 The collector system . . . . .	8
2.4 Aiming strategies . . . . .	10
2.5 Conclusion . . . . .	14
<b>3 Method</b>	<b>15</b>
3.1 Research design . . . . .	15
3.2 Methodology . . . . .	16
3.3 Analysed systems . . . . .	25
3.4 Computer specifications . . . . .	30
3.5 Conclusion . . . . .	30

<b>4</b>	<b>Analysis of flux distribution prediction methods</b>	<b>31</b>
4.1	Ray tracing . . . . .	31
4.2	Computational expense . . . . .	33
4.3	The one-point fitting model . . . . .	34
4.4	The Landman-Grobler improvement method . . . . .	34
4.5	Analysis of a single heliostat . . . . .	35
4.6	Conclusion . . . . .	39
<b>5</b>	<b>Optimisation methods for aiming strategies</b>	<b>41</b>
5.1	Tabu search optimisation . . . . .	41
5.2	Genetic algorithm . . . . .	48
5.3	Conclusion . . . . .	55
<b>6</b>	<b>Aiming strategy results</b>	<b>56</b>
6.1	Improvements on previous methods . . . . .	56
6.2	Assumptions . . . . .	57
6.3	Combined optimisation for case study 1: Helio40 . . . . .	57
6.4	Combined optimisation for case study 2: Helio100 . . . . .	58
6.5	Combined optimisation for case study 3: PS10 . . . . .	59
6.6	Conclusion . . . . .	61
<b>7</b>	<b>Experimentation</b>	<b>63</b>
7.1	Experimental setup . . . . .	63
7.2	Experimental flux distribution models . . . . .	65
7.3	Conclusion . . . . .	69
<b>8</b>	<b>Analysis and discussion</b>	<b>70</b>
8.1	Factors affecting static aiming strategies . . . . .	70
8.2	Factors affecting dynamic aiming strategies . . . . .	71
8.3	Dynamic aiming . . . . .	75
8.4	Implementation of the proposed aiming strategy . . . . .	76
8.5	Conclusion . . . . .	76
<b>9</b>	<b>Conclusions</b>	<b>77</b>
9.1	Summary of findings . . . . .	77
9.2	Conclusions . . . . .	78
9.3	Summary of contributions . . . . .	78
9.4	Suggestions for further research . . . . .	79
	<b>Appendices</b>	<b>81</b>
<b>A</b>	<b>Supporting mathematical functions</b>	<b>82</b>
A.1	Delaunay triangulation . . . . .	82
A.2	Vector rotation . . . . .	83
A.3	Gaussian mixture model fitting . . . . .	83
<b>B</b>	<b>Factors affecting the flux profile</b>	<b>86</b>
B.1	Sunshape . . . . .	86
B.2	Surface slope error . . . . .	88

*CONTENTS*

x

B.3 Incidence angle . . . . .	88
<b>C Tracking methods</b>	<b>92</b>
C.1 Azimuth elevation tracking . . . . .	92
C.2 Fixed horizontal tracking . . . . .	92
C.3 Target aligned tracking . . . . .	92
<b>List of References</b>	<b>94</b>

# List of Figures

1.1	The SUNSPOT cycle (adapted from Kröger, 2012)	3
2.1	Typical molten salt central receiver system process	7
2.2	Heliostat components (adapted from Stine and Geyer (2001))	8
2.3	Example of Gaussian distributed flux map of a single heliostat	9
2.4	Side view of panel with optimised flux profile	11
2.5	The receiver aim point and standby point positions (adapted from Garcia-Martin, 1999)	12
2.6	Representation of the possible "pheromone" intensities for a single heliostat (by author)	13
2.7	Flux distribution over the Ivanpah receiver (adapted from Koretz, 2014)	14
3.1	Research flow diagram	16
3.2	Coordinate system used in the model	17
3.3	Example of contour plot of bivariate Gaussian model	21
3.4	Reflected image of experimental heliostat	21
3.5	Example of superimposing of bivariate Gaussian models (Solid lines) to form a Gaussian mixture model (Dotted lines)	22
3.6	Example of contour plot of Gaussian mixture model	22
3.7	An example of the receiver aim point positions with the aim area in gray	24
3.8	Flow diagram of combined optimisation strategy	25
3.9	Layout of the experimental Helio40 heliostat field	26
3.10	A proposed layout for the Helio100 system (not to scale)	28
3.11	A proposed Helio100 layout (rendering by James Larmuth)	28
3.12	PS10 field layout (Anon., 2008)	29
4.1	The three stages in the heliostat field and receiver model	32
4.2	Illustration of binning box position over a receiver aperture	33
4.3	Standard deviations of radial images for different sunshapes	35
4.4	The normalized intensity distributions of different sunshapes (adapted from Schwarzbözl, 2009)	36
4.5	Standard deviations of radial images for different sunshapes	37
4.6	Standard deviation on the y-axis for a surface slope error variation at an incidence angle of $10^\circ$	38
4.7	Peak flux for a surface slope error variation at an incidence angle of $10^\circ$	38
4.8	Standard deviations of flux images for incidence angle variation for surface slope error of 2 mrad in the sagittal plane	40

4.9	Standard deviations of flux images for incidence angle variation for surface slope error of 2 mrad in the tangential plane . . . . .	40
5.1	Algorithm for the Tabu optimisation method . . . . .	42
5.2	An example of the Tabu chart . . . . .	43
5.3	Illustration of the positioning of heliostats according to the Tabu model .	43
5.4	Flux map of the Helio40 system on 21 December at 12h00 before (left) and after (right) Tabu optimisation for the Collado approximation (HF) and the ray tracer (RT) . . . . .	44
5.5	Contour plot of the Helio40 system on 21 December at 12h00 before (left) and after (right) Tabu optimisation . . . . .	44
5.6	Flux map of the Helio40 system on 21 December at 9h00 before (left) and after (right) Tabu optimisation . . . . .	45
5.7	Contour plot of the Helio40 system on 21 December at 9h00 before (left) and after (right) Tabu optimisation . . . . .	46
5.8	Flux map of the Helio100 system on 21 December at 12h00 before (left) and after (right) Tabu optimisation . . . . .	46
5.9	Contour plot of the Helio100 system on 21 December at 12h00 before (left) and after (right) Tabu optimisation . . . . .	47
5.10	Flux map of the Helio100 system on 21 December at 9h00 before (left) and after (right) Tabu optimisation . . . . .	47
5.11	Contour plot of the Helio100 system on 21 December at 9h00 before (left) and after (right) Tabu optimisation . . . . .	48
5.12	An example of randomly generated populations . . . . .	49
5.13	The receiver surface with the various aim point squares on the aim area	51
5.14	Flux map of the Helio40 system on 21 December at 12h00 before (left) and after (right) GA optimisation . . . . .	52
5.15	Contour plot of the Helio40 system on 21 December at 12h00 before (left) and after (right) GA optimisation . . . . .	52
5.16	Flux map of the Helio40 system on 21 December at 9h00 before (left) and after (right) GA optimisation . . . . .	52
5.17	Contour plot of the Helio40 system on 21 December at 9h00 before (left) and after (right) GA optimisation . . . . .	53
5.18	Flux map of the Helio100 system on 21 December at 12h00 before (left) and after (right) GA optimisation . . . . .	53
5.19	Contour plot of the Helio100 system on 21 December at 12h00 before (left) and after (right) GA optimisation . . . . .	54
5.20	Flux map of the Helio100 system on 21 December at 9h00 before (left) and after (right) GA optimisation . . . . .	54
5.21	Contour plot of the Helio100 system on 21 December at 9h00 before (left) and after (right) GA optimisation . . . . .	55
6.1	Flux map of the Helio40 system on 21 December at 12h00 before (left) and after (right) combined optimisation for the ray tracer (RT) and Gaussian mixture model (GM) . . . . .	57
6.2	Contour plot of the Helio40 system on 21 December at 12h00 before (left) and after (right) combined optimisation . . . . .	58

6.3	Flux map of the Helio40 system on 21 December at 9h00 before (left) and after (right) combined optimisation . . . . .	58
6.4	Contour plot of the Helio40 system on 21 December at 9h00 before (left) and after (right) combined optimisation . . . . .	59
6.5	Flux map of the Helio100 system on 21 December at 12h00 before (left) and after combined optimisation (right) . . . . .	59
6.6	Contour plot of the Helio100 system on 21 December at 12h00 before (left) and after combined optimisation (right) . . . . .	60
6.7	Flux map of the Helio100 system on 21 December at 9h00 before (left) and after (right) combined optimisation . . . . .	60
6.8	Contour plot of the Helio100 system on 21 December at 9h00 before (left) and after (right) combined optimisation . . . . .	61
6.9	Flux map of the PS10 system on 21 December at 12h00 before (left) and after (right) combined optimisation . . . . .	61
6.10	Contour plot of the PS10 system on 21 December at 12h00 before (left) and after (right) combined optimisation . . . . .	62
7.1	Experimental setup . . . . .	64
7.2	A Helio40 heliostat showing warping of the reflected image . . . . .	64
7.3	Flux image of a single heliostat created by image processing . . . . .	66
7.4	Comparison of measured flux from flux sensor and interpolated flux from image processing . . . . .	66
7.5	Processed flux image (left) and GMM determined for the experimental image (right) . . . . .	67
7.6	Flux distribution of aiming strategy before (left) and after (right) the aiming strategy was implemented . . . . .	68
7.7	Thermal measurements for central aiming (top left), 5 point aiming strategy (top right), after three minutes (bottom left) and after six minutes (bottom right) . . . . .	69
8.1	An illustration of drift affecting the position of the aimpoint on the target for a stationary heliostat . . . . .	72
8.2	Aim point positions (left) and an example of the simulated aim positions of the heliostats (right) . . . . .	74
8.3	Statistical representation of homogenisation factors for various standard deviations of tracking errors . . . . .	74
8.4	Statistical representation of power loss for various standard deviations of tracking errors . . . . .	75
A.1	Delaunay triangulation (de Berg <i>et al.</i> , 2008) . . . . .	82
A.2	Edge flip of two triangles (Adapted from de Berg <i>et al.</i> , 2008) . . . . .	83
A.3	Vector rotation of aim points . . . . .	84
A.4	Gaussian model fitting procedure . . . . .	85
B.1	Photograph of the solar aureole with the solar disc blocked out (Fleet, 2013) . . . . .	86
B.2	Flux distribution of ideal heliostat with Gaussian sunshape (left) and pillbox sunshape (right) . . . . .	87

B.3	Flux distribution of heliostat with surface slope error of 0.5 for Gaussian sunshape (left) and pillbox sunshape (right) . . . . .	88
B.4	Flux distribution of heliostat with surface slope error of 1 for Gaussian sunshape (left) and pillbox sunshape (right) . . . . .	89
B.5	Illustration of optical aberration of astigmatism . . . . .	89
B.6	Flux profiles for various surface slope errors and incidence angles . . . . .	90
B.7	Image size for the tangential plane (a) and the sagittal plane (b) at small and large incidence angles (Courtesy of Landman <i>et al.</i> , 2014) . . . . .	91
C.1	Azimuth elevation rotational axes . . . . .	93
C.2	Fixed horizontal rotation axes . . . . .	93
C.3	Target aligned rotational axes . . . . .	93

# List of Tables

3.1	Inputs used in the Helio40 model . . . . .	26
3.2	Inputs used in the Helio100 model . . . . .	27
3.3	Inputs used in the PS10 model . . . . .	29
3.4	Computer specifications . . . . .	30
4.1	Inputs used in the evaluation model . . . . .	36
7.1	List of experimental instrumentation . . . . .	63

# Nomenclature

## Variables

$A$	Azimuth . . . . .	[ $^{\circ}$ ]
$A_m$	Mirror area . . . . .	[m]
$B$	Heliostat position . . . . .	[m]
$D$	Slant range . . . . .	[m]
$d$	Effective diameter . . . . .	[m]
$FD$	Flux . . . . .	[W/m <sup>2</sup> ]
$F$	Fitness function . . . . .	[W/m <sup>2</sup> ]
$f$	Focal length . . . . .	[m]
$f$	Cost function . . . . .	[W/m <sup>2</sup> ]
$f_{at}$	Attenuation factor . . . . .	[–]
$G$	Objective function . . . . .	[W/m <sup>2</sup> ]
$H_F$	Homogenisation factor . . . . .	[–]
$h$	Height . . . . .	[m]
$I_d$	Direct normal irradiance . . . . .	[W/m <sup>2</sup> ]
$I_{max}$	Maximum number of mutations and crossovers . . . . .	[–]
$i$	Iteration . . . . .	[–]
$iter$	Maximum number of iterations . . . . .	[–]
$M_p$	Mating pool size . . . . .	[–]
$m$	Number of aimpoints . . . . .	[–]
$N_p$	Number of populations . . . . .	[–]
$n$	Number of heliostats . . . . .	[–]
$P$	Total power . . . . .	[W]
$PL$	Total power loss . . . . .	[W]
$P_c$	Crossover probability . . . . .	[–]
$P_h$	Power per heliostat . . . . .	[W]
$P_j$	Probability of each population . . . . .	[–]
$P_m$	Mutation probability . . . . .	[–]
$Q$	Sum of fitness functions . . . . .	[W/m <sup>2</sup> ]
$r$	Radius of curvature . . . . .	[m]
$T$	Target centre position . . . . .	[m]

$V$	Loss function . . . . .	[ – ]
$w$	Width . . . . .	[ m ]
$x$	x-coordinate . . . . .	[ m ]
$y$	y-coordinate . . . . .	[ m ]
$Z$	Zenith . . . . .	[ ° ]
$z$	z-coordinate . . . . .	[ m ]
$z$	Random number . . . . .	[ – ]
$\beta_s$	Subtending angle . . . . .	[ mrad ]
$\epsilon$	Small value . . . . .	[ – ]
$\mu$	Mean . . . . .	[ mrad ]
$\mu_x$	Mean in x direction . . . . .	[ mrad ]
$\mu_y$	Mean deviation in y direction . . . . .	[ mrad ]
$\rho$	Reflectivity . . . . .	[ – ]
$\rho$	Bivariate normal distribution parameter . . . . .	[ – ]
$\Sigma$	Covariance . . . . .	[ mrad ]
$\sigma$	Standard deviation . . . . .	[ mrad ]
$\sigma_{ast}$	Astigmatic error . . . . .	[ mrad ]
$\sigma_{bq}$	Beam quality . . . . .	[ mrad ]
$\sigma_{HF}$	Standard deviation for HFLCAL approximation . . . . .	[ mrad ]
$\sigma_{SSE}$	Surface slope error . . . . .	[ mrad ]
$\sigma_{sun}$	Sunshape standard deviation . . . . .	[ mrad ]
$\sigma_t$	Tracking error . . . . .	[ mrad ]
$\sigma_x$	Standard deviation in x direction . . . . .	[ mrad ]
$\sigma_y$	Standard deviation in y direction . . . . .	[ mrad ]
$\phi$	Incidence angle . . . . .	[ ° ]
$\phi_{rec}$	Receiver incidence angle . . . . .	[ ° ]
$\psi$	Field rotation angle . . . . .	[ ° ]

**Vectors and Tensors**

<b>A</b>	Target normal vector
<b>H</b>	Heliostat normal vector
<b>R</b>	Vector from heliostat to target aimpoint
<b>S</b>	Solar vector

**Subscripts**

GM	Gaussian mixture
h	Heliostat
HF	HFLCAL flux approximation method
$j$	Population

max	Maximum
min	Minimum
RT	Ray tracer
$x,y,z$	Coordinates

**Abbreviations**

AIC	Akaike information criteria
ASME	American Society of Mechanical Engineers
CGD	Circular Gaussian distribution
CSP	Concentrating solar power
FD	Flux distribution
HTF	Heat transfer fluid
HFLCAL	Heliostat field layout calculator (German Aerospace Centre)
GM	Gaussian mixture
SFINCS	Solar field integrated control
SSE	Surface slope errors
STERG	Solar Thermal Energy Research Group
SUNSPOT	Stellenbosch University Solar Power Thermodynamic (cycle)

# Chapter 1

## Introduction

*"I'd put my money on the Sun and Solar Energy, what a source of Power! I hope we don't have to wait until oil and coal run out, before we tackle that."*

- Thomas Edison in conversation with Henry Ford and Harvey Firestone (1931)

### 1.1 Background

The US Energy Information Administration (2011) predicted that between 2008 and 2035 the global energy demand will grow by 53 %. While energy demand is rising due to population and economic growth, fossil reserves are diminishing.

Besides the increasing demand in energy, environmental issues related to the use of fossil fuels for power generation are also a concern. Emissions from the combustion of fossil fuels are acknowledged to cause global warming and can be detrimental to human and animal health, crops and structures (Barbir *et al.*, 1990). Should these emissions continue, a temperature increase of 2 °C and even up to 4 °C is predicted to occur by the 2060's (World Bank, 2012). Some of the effects of a temperature increase of this magnitude are floods, drought, forest fires, water and food shortages; and heat waves. Consequently, alternative energy sources are required to mitigate the effects of fossil fuels on the environment.

Renewable energy sources are replenishable and generally thought to have little impact on the environment (Intergovernmental panel on climate change, 2011). Renewable technologies include wind, solar, geothermal, hydro and biomass energy. Solar energy is a clean energy source that provides energy in abundance. Barlev *et al.* (2011) state that the annual consumption of energy on earth could be provided by the sun in one hour. However, because of the diurnal movement of the sun, the energy supply is intermittent. Electricity generation using the sun's energy is done by means of photovoltaic technology or by concentrating solar energy and converting it into thermal energy for use in a heat engine.

Technologies of the latter method are called concentrating solar power (CSP) systems. Technologies for these systems include the line focus parabolic trough and linear Fresnel technology as well as the point focus Stirling solar dishes and central receiver systems (Behar *et al.*, 2013). Central receiver systems, otherwise known

as solar towers, consist of a central receiver surrounded by thousands of reflective mirrors tracking the sun. These mirrors, known as heliostats, reflect and concentrate solar energy onto a central receiver where it is converted into thermal energy by means of a heat transfer fluid (HTF). The thermal energy is then either stored or directly used to generate electricity.

One advantage of this technology is the ability to be integrated with fossil fuel generators (Barlev *et al.*, 2011). During peak hours, these systems would be able to provide the excess power needed by making use of storage. If storage is not used, this technology produces electricity on an intermittent basis (The CSP Alliance, 2012). For this reason, central receiver systems become attractive auxiliary power generation technologies when combined with thermal storage because of the availability of power at high demand periods.

The SANDIA Power Tower Technology Roadmap and Cost Reduction Plan has identified several technology improvement opportunities with a focus on cost reduction and increased efficiency (Kolb *et al.*, 2011). For higher thermal efficiency a higher thermal input temperature is required. The highest temperature and minimum power loss occurs when all heliostats are aimed at the centre of the receiver (Gallego *et al.*, 2014). However, higher temperatures on the receiver can introduce thermal stresses and reduce the lifetime of the receiver (Rodríguez-Sánchez *et al.*, 2013). It is believed that thermal stresses may be reduced by means of aiming strategies by which heliostat aim points are redistributed in order to obtain lower thermal gradients on the receiver surface (Belhomme *et al.*, 2013). The objective of aiming strategies is to lower peak flux and homogenise the flux distribution over the receiver while maximising the collected power (Gallego *et al.*, 2014).

## 1.2 Motivation

Static aiming strategies require an approximation of the flux distribution over the receiver because optimisation is done before the implementation of the aiming strategy. Ray tracing is often used to predict the flux distribution, but it is computationally expensive. Therefore methods of approximating flux profiles as circular Gaussian distributions (CGD) are favoured. Aiming strategies incorporating CGD flux mapping have been previously developed, but little information is given by the authors on the implications of using these approximate methods (Salomé *et al.*, 2013; Besarati *et al.*, 2014). Opinions of other researchers vary regarding the use of CGD methods of flux predictions. Schwarzbözl *et al.* (2009) state that approximation methods such as HFLCAL do not provide enough accuracy for determining flux distributions and suggest using ray tracing instead. Collado (2010) claims that the HFLCAL model serves as a suitable method for optimisation, provided information regarding the dynamic images of the heliostats are known. An investigation into these approximate flux mapping methods is required.

This research ties in with several other research topics at Stellenbosch University Mechanical Engineering Department which revolves around the power operation cycle by the late professor Detlev Kröger. Named the SUNSPOT (Stellenbosch Uni-

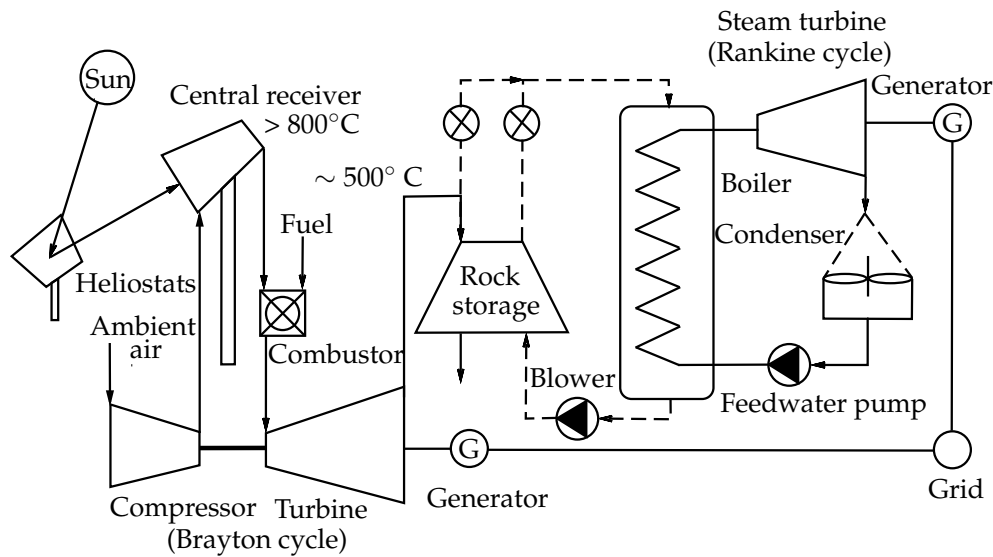


**Figure 1.1:** The SUNSPOT cycle (adapted from Kröger, 2012)

versity Solar Power Thermodynamic) cycle, this system represents a combined cycle thermodynamic system which incorporates concentrating solar power through the use of a heliostat and receiver system. An illustration of this system is shown in Figure 1.1. Air is used as working fluid and heated up to  $800\text{ }^{\circ}\text{C}$  in the receiver. The heated air is used in a Brayton cycle and steam in a Rankine cycle to generate electricity. The system includes thermal storage through a packed rock bed. This research in aiming strategies will be the first at Stellenbosch University and will contribute to the research done pertaining to the SUNSPOT cycle.

The Solar Thermal Energy Research Group (STERG) has built an experimental heliostat and target facility funded by Sasol, named Helio40. This  $40\text{ m}^2$  20 heliostat facility provides a platform for researchers to do experimental work pertaining mostly to heliostat optics, controls and receivers.

Currently, research and development is also done at STERG on the Helio100 project funded by the Technology Innovation Agency (TIA). This project will include the construction of a  $100\text{ kW}$  pilot facility to be completed in September 2015.

Previous topics in the research group include the development of a ray tracer and the optimisation of heliostat surface profiles. The next step in optical research is the development of an aiming strategy, especially because of its novelty to both STERG and Stellenbosch University. Aiming strategies are influenced by several components in the central receiver system; therefore, any research done in this field would potentially provide the researcher with knowledge in other fields such as optics, tracking, controls and receiver theory.

### 1.3 Research objectives

The objectives of this research are to investigate flux approximation methods and develop an aiming strategy that could be used on small central receiver systems. The aiming strategy would be the first aiming strategy in STERG and be applicable to the Helio40 and Helio100 heliostat and receiver systems. The proposed aiming strategy should be able to homogenize the flux on the target while limiting the amount of thermal power lost due to spillage. In order to reach the main objectives, the following methodology is set:

- Understand optics of heliostat systems and aiming strategies through a literature review
- Develop a model which could be used for any unique heliostat field and receiver system with the purpose of determining the flux density distribution at any specific time
- Investigate and compare numerical and analytical flux approximation techniques
- Develop an aiming strategy by using flux density approximation methods
- Compare theoretical and experimental results for the Helio40 heliostats
- Analyse and interpret findings
- Conclude and make recommendations

### 1.4 Delineation and limitations

Aiming strategies influence and are influenced by many different components in central receiver systems. However, because this is the first study of the topic in the research group, the content has been prioritised, and the method developed in this thesis is limited to fulfil the following requirements:

- Determine the position of the sun for any time and location
- Model any heliostat field size or layout
- Determine the flux density distribution on the receiver by means of ray tracing or CGD methods
- Optimise the flux density distribution by homogenising the flux over the receiver aperture for a maximum power loss

The scope of this study is limited to the following:

- Evaluation of current methods of predicting flux distribution
- Optimisation of small heliostat fields using limited computational capacity
- Modelling of flux distribution on flat plane and single sections of cylindrical receivers

- Vertical and two-dimensional aiming
- Analyses and discussion of factors influencing aiming strategies such as wind loads, tracking errors and cloud cover
- Analysis and interpretation of factors influencing flux distribution profiles through experimentation
- Assume static aiming only

The scope of this study does not include the following:

- HelioStat characterisation by means of a coordinate measurement machine
- Modelling of temperature on the aperture of the receiver
- Modelling of volumetric and cavity receivers
- Modelling of multiple heliostat facets and canting strategies
- Closed loop aiming strategies, errors and other dynamic effects
- Receivers angled beyond the vertical plane
- Blocking and shadowing
- Developing a graphical user interface for the aiming strategy
- Surrounding heliostat fields
- Three-dimensional aiming

## 1.5 Chapter overview

Chapter 2: A review is done regarding the fundamentals of central receiver systems, particularly the collector system, optical analysis methods and aiming strategies.

Chapter 3: The research method is presented, which details the methodology and research design behind this thesis.

Chapter 4: Numerical and analytical flux approximation models are discussed and compared as a basis for the aiming strategy.

Chapter 5: The Tabu search and Genetic algorithm optimisation methods are explained and simulations run for the Helio40 and Helio100 cases.

Chapter 6: The developed aiming strategy is implemented on the Helio40, Helio100 and PS10 cases and the results discussed.

Chapter 7: Methods of obtaining flux distributions experimentally are discussed. An experimental investigation of aiming strategies is also included.

Chapter 8: An analysis and discussion of the factors which affect aiming strategies is presented, followed by suggestions for continuous aiming and a proposal for the implementation of an aiming strategy.

Chapter 9: Finally a summary of the findings and contributions as well as suggestions for further research are given.

## Chapter 2

# Literature Review

The literature review aims to give a broad overview of the central receiver system and provides a comprehensive introduction to published aiming strategies. The following chapter contains significant parts of the review paper *A review of aiming strategies for central receivers* (Grobler and Gauché, 2014). The paper focuses on the review of various aiming strategies and the corresponding receivers they pertain to.

### 2.1 Introduction

As the commercialisation of central receiver systems becomes a reality, advancements in this field are necessary to keep lowering the costs and raising the efficiency of these plants. The function of a central receiver is interception and conversion of the solar light concentrated by the heliostat field. Typically thousands of heliostats are arranged around a central receiver tower and aim solar light at the receiver aperture.

Aiming all heliostats at the centre of the receiver would create a non-uniform high flux density on the aperture. In such a scenario, thermal gradients and high temperatures would occur on the receiver due to the uneven distribution of flux, likely leading to deterioration of the receiver and lowering the receiver thermal efficiency and lifetime (Salomé *et al.*, 2013).

This problem is typically solved by introducing aiming strategies to distribute flux more evenly on the receiver while obtaining maximum power within the temperature and flux limitations (Belhomme *et al.*, 2013). Aiming strategies differ for each unique central receiver system due to the receiver geometry and limitations and heliostat field design.

The following section reviews central receiver systems focusing on heliostats and receivers. Finally, literature on aiming strategies are reviewed and summarised.

## 2.2 Central receiver systems

According to the International Renewable Energy Agency (IRENA), the ability of central receivers to reach very high temperatures, particularly with molten salt as HTF, could make it the CSP technology of choice in the future (IRENA, 2012). The basic concept of central receiver systems is similar to conventional coal and gas power stations. In all cases, a thermodynamic cycle is used to convert thermal energy into electric energy. The difference between conventional power technology and central receiver systems is the method by which the thermal energy is obtained.

Central receiver systems typically consist of heliostats, one or multiple receivers and an electric power generation system. Thermal storage is used because of the intermittent nature of the solar resource; this allows dispatchable electric energy generation even when sunlight is unavailable (Denholm and Hummon). Figure 2.1 illustrates the process of a molten salt central receiver system with storage.

The heliostats surrounding the receiver are able to track the sun on two rotational axes in order to reflect the incident solar light on the receiver aperture. The reflected light is absorbed by the receiver and converted to thermal energy with HTF temperatures reaching more than 1000 °C, depending on the receiver design and HTF (Pitz-Paal *et al.*, 2005). After being heated in the receiver, the HTF is used to generate electricity either directly or indirectly. The conversion of energy from thermal to electric is done by means of a Rankine, Brayton or combined cycle (Behar *et al.*, 2013).

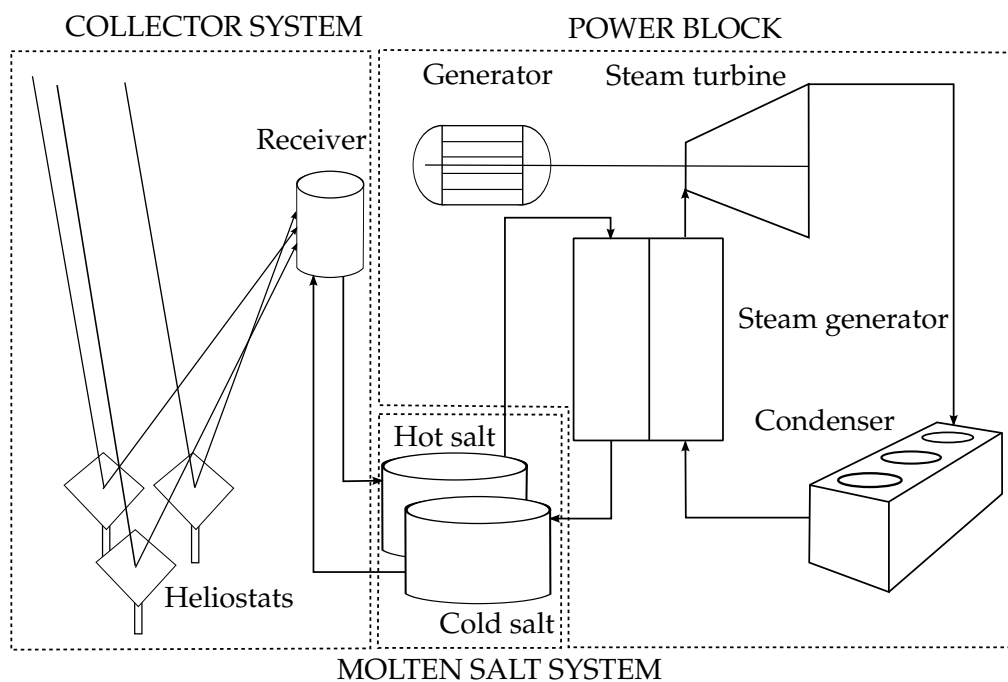


Figure 2.1: Typical molten salt central receiver system process

CSP generation systems are typically sized between 10 and 200 MW (Romero *et al.*, 2002). The other components in the central receiver system are designed according to the size of the power block using an iterative design process (Zavoico, 2001). After the sizing of the power block and storage, the heliostat field layout with its collective area is determined.

### 2.3 The collector system

According to the heliostat cost reduction study by Sandia National Laboratories, heliostats contribute roughly 50% to the total power plant costs (Kolb *et al.*, 2007). Research and development has, therefore, been focussed on improving the quality and efficiency of the solar field while lowering costs. The design of the heliostats, the quality of the tracking system and the heliostat field layout contribute to the total performance of the central receiver system (Behar *et al.*, 2013).

Conventional heliostats consist of single or multiple facets mounted on a pedestal with two rotational axes and control system as shown in Figure 2.2. The reflective surface of the heliostat is rotated around two axes relative to the position of the sun such that an image is reflected onto the receiver aperture. The angle between the heliostat normal vector and the incident solar vector is known as the incidence angle. The size of the image reflected onto the receiver aperture will be a minimum at an incidence angle of zero (Igel and Hughes).

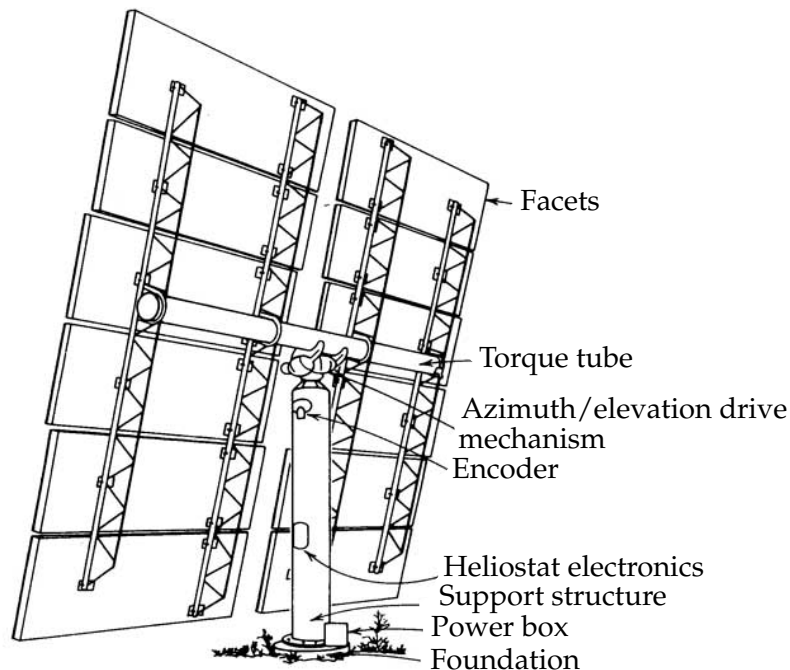
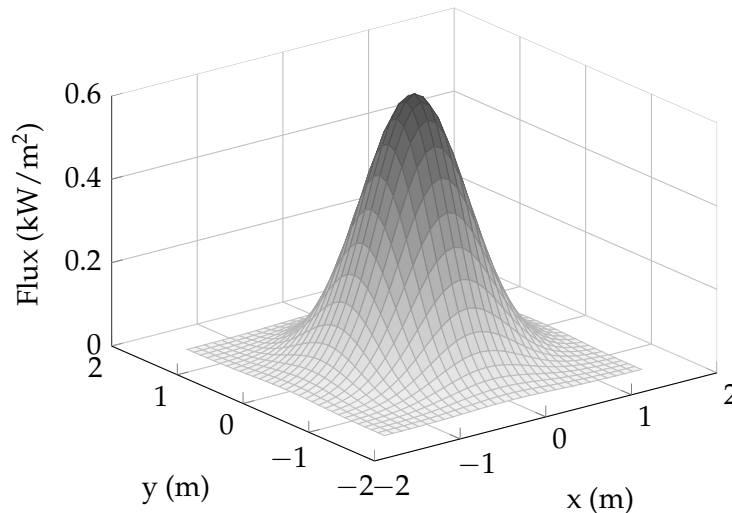


Figure 2.2: Heliostat components (adapted from Stine and Geyer (2001))

The optical quality of the facets and sunshape distribution account for the change in the reflected image at different times (Schwarzbözl *et al.*, 2009). When an image is reflected onto a receiver, the insolation reaching the receiver varies in density. The radiation per square meter on any point of the receiver aperture is known as the flux density. The flux distribution of the solar light reflected onto a flat receiver often approximates a near Gaussian distribution as seen in Figure 2.3 (Boese *et al.*, 1981). The flux distribution over the receiver can be predicted by using optical modelling methods. These modelling methods can generally be divided into two groups: analytical and numerical flux prediction.



**Figure 2.3:** Example of Gaussian distributed flux map of a single heliostat

Analytical models are used for field layout analysis and optimisation where the flux density is approximated through simplified convolution models (Garcia *et al.*, 2008). These modelling methods include HFLCAL, DELSOL and URC-RCCELL (Bode and Gauché, 2013). A disadvantage of using convolution models is the low precision with which the maximum flux density and distribution are predicted (Garcia *et al.*, 2008). However, approximation methods are justified for large fields due to the central limit theorem, which states that the superposition of a large number of random distribution functions will converge towards a Gaussian distribution (Schmitz *et al.*, 2006).

Ray tracing is a numerical optical method that uses random samples of data to provide an accurate representation of the flux distribution (Bode and Gauché, 2013). SolTrace, Tonatiuh, STRAL and TieSol are some of the ray tracing codes used in optical analysis. Accurate optical codes are necessary when designing both the receiver and heliostat optical system (Garcia *et al.*, 2008). The flux image produced on the receiver is influenced by error sources such as time, the sun model, location, heliostat field positions, solar position, atmospheric refraction, processor accuracy and installation tolerances (Berenguel *et al.*, 2004).

Receivers are designed for high thermal capacity and resistance to thermal stresses and shock (Ho and Iverson, 2012). Typically the temperature on metal and ceramic receivers can reach 700 °C to 800 °C and more than 1000 °C respectively (Gallego *et al.*, 2014). Large thermal gradients introduce thermal stresses, which can result in elastic and potentially plastic deformation (Liao *et al.*, 2014). Additionally, material degradation can occur in these conditions causing reduction of receiver life (Lata *et al.*, 2008). Typical causes of large thermal gradients are passage of clouds, start-up and shut-down and high incident fluxes (Liao *et al.*, 2014; Augsburger and Favrat, 2013).

According to Vant-Hull (2002) high incident fluxes could be reduced through the increase of the receiver size, field modifications or redistributing the flux on the surface of the receiver. The first two approaches result in increased costs due to increased receiver materials and a decrease in heliostat efficiency respectively. The third approach is generally known as ‘optimised aiming strategies’ and has the advantage of reducing peak flux without an increase in cost.

## 2.4 Aiming strategies

Aiming strategies include the prediction and optimisation of the flux profile on the receiver surface. In other words, the flux distribution on the receiver is simulated using an optical modelling method and optimised such that the flux is evenly distributed over the receiver. Optimisation methods determine the positions on the receiver where each heliostat needs to aim in order to obtain a homogenised flux profile. The purpose of an aiming strategy is to have good receiver reliability and durability while keeping costs low and efficiency high (Lata *et al.*, 2008). The following section discusses published aiming strategies which have been developed, tested and implemented.

### 2.4.1 Abengoa Solar and Gemasolar: Flux distribution on vertical plates

A simple flux distribution profile is introduced in a study done by Abengoa Solar evaluating six different central receiver plant designs. The receiver design consists of 24 panels of tubes arranged in a cylindrical shape and makes use of parallel flow of the heat transfer fluid. An even flux profile is created on the central 75% of each panel (Figure 2.4) (Kelly, 2010). The aim points of each heliostat initially associated with a specific panel is moved vertically up or down the panel until the desired flux distribution is created.

At Gemasolar, the first commercial sized solar tower technology to use molten salt storage, this flux optimisation method is further improved by relating the positions of the aim points to the distance of each heliostat to the receiver. In this improved method, the closest heliostats are focused at the top and bottom aim points while further heliostats aim at the central aim points (Augsburger, 2013).

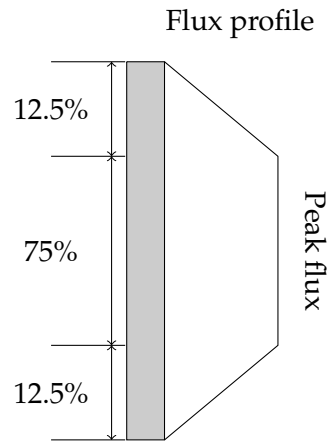


Figure 2.4: Side view of panel with optimised flux profile

### 2.4.2 Solar Two: Static and dynamic aim processing systems

The receiver of the experimental plant, Solar Two, comprised of 24 panels with 32 tubes each, is configured as an external cylinder (Tyner *et al.*, 1995). Flux on the receiver was controlled by a static and dynamic software system. A static aim processing system determined the initial aim point for each heliostat according to the orientation and errors related to the respective heliostat. A dynamic aim processing system estimated the flux density on the receiver aperture for 21 nodes on each panel. When the flux of a node surpassed the allowable flux density, the heliostat aimed at the node responsible for the high flux density was removed from operation (García-Martín *et al.*, 1999).

### 2.4.3 Plataforma Solar de Almería (PSA) CESA-1 Plant: Temperature optimisation

A closed loop automated system was developed by García-Martín *et al.* (1999) for the open cycle volumetric receiver at the Plataforma Solar de Almería (PSA) solar plant. Thin wire packages in the form of hexagonal cells make up the profile of the receiver.

Biggs and Vittitoe (1979) determined that only five aim points were necessary in this aiming strategy in order to optimise the flux distribution. Therefore, the PSA aiming strategy utilises five aim points located on the receiver and four standby points located off the receiver as illustrated in Figure 2.5.

The standby points are used to aim the heliostats away from the receiver before aiming at aim points after defocusing or during emergencies. Initially, each heliostat is assigned to one of the five aim points in such a manner as to distribute the irradiance more evenly over the receiver aperture (García-Martín *et al.*, 1999). An optimisation code called HELIOS is used to determine the initial aim points for each heliostat (Braun, 1996). Four thermocouples measure the temperature of the receiver surface, while another 36 thermocouples are placed at the back of the ab-

sorber to determine the temperature of the air at the specific points (García-Martín *et al.*, 1999). The receiver is divided into 5 zones, and the average temperature is de-

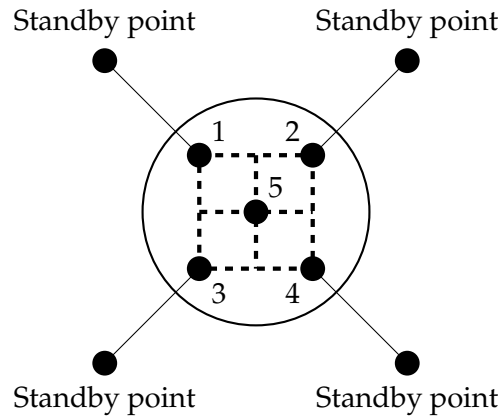


**Figure 2.5:** The receiver aim point and standby point positions (adapted from García-Martín, 1999)

termined for each zone. The heliostats are relocated to other aim points such that the average temperature is within the set limits (García-Martín *et al.*, 1999). The positions of each aim point can also be controlled to allow further adjustment to the temperatures of the zones. The objective of this real-time system is to keep the difference between the maximum and minimum temperatures below  $100^{\circ}\text{C}$  as proposed by the receiver manufacturer, L&C Steinmüller (García-Martín *et al.*, 1999).

#### 2.4.4 THEMIS solar tower: Control of flux distribution

An open loop control process that uses analytical flux prediction methods has been developed by Salomé *et al.* (2013) for the THEMIS research platform in Targasonne, France. The main purpose of this method is to uniformly distribute the flux density on flat plate receivers within the limits of the system (Salomé *et al.*, 2013).

This method uses the HFLCAL approximation model for estimating the flux distribution on the receiver (Schwarzbözl *et al.*, 2009). Aiming points are pre-defined according to the dimensions of the receiver. The Tabu meta-heuristic algorithm is used to allocate heliostats to aim points to optimise the flux distribution while minimising the amount of power lost. Heliostats producing a large image on the aperture are favoured to aim at the central aim points to reduce spillage, while heliostats producing small images are aimed at the outer aim points (Salomé *et al.*, 2013).

A similar aiming strategy was developed by Besarati *et al.* (2014) also using the HFLCAL approximation method, but incorporating a Genetic algorithm as optimisation method.

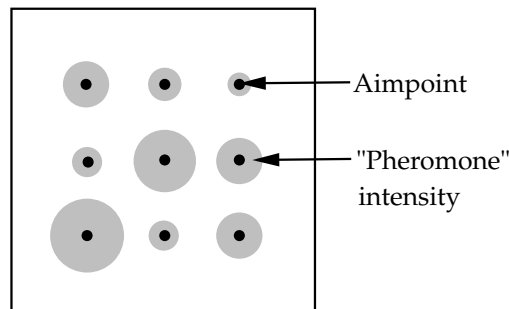


**Figure 2.6:** Representation of the possible "pheromone" intensities for a single heliostat (by author)

#### 2.4.5 Jülich solar tower test and research plant: Ant colony optimisation

An optimisation method for the Jülich solar tower test and research plant was developed using the ant colony optimisation algorithm introduced by Dorigo (Ahlbrink *et al.*, 2010b; Dorigo and Gambardella, 1997). The optimisation method uses STRAL (Belhomme *et al.*, 2009) ray tracing software instead of flux estimation. The optimization criterion for this method is to maximize the receiver output instead of the efficiency.

Ant colony optimisation uses the natural behaviour of ants in order to determine the optimal aim point for each heliostat (Dorigo and Stützle, 2004). When a good resource is found, the ants will excrete pheromones to guide other ants to the resource. Ants will follow the highest concentration of pheromones in order to find the resource.

In a similar way, each heliostat and aim point combination has its own concentration of pheromones proportionate to the receiver power (quality value). The higher the receiver power when a heliostat is aiming at a specific aim point, the more likely that heliostat will choose to aim at that aim point in the future. This method results in shorter computational time for each iteration since the heliostats have a better chance of finding the optimum solution (Belhomme *et al.*, 2013). Figure 2.6 shows an example of the pheromone intensities on all aim points for one heliostat.

#### 2.4.6 Combination of aim point and thermodynamic optimization

Specifically pertaining to open volumetric receivers, this optimisation method does not only make use of aiming strategies but of mass flow manipulation as well. After the optimal flux distribution is found through optimisation methods the maximum mass flow rate is determined for an outlet temperature as required by the storage or generation system. After the calculation of the optimal mass flow rate, the aiming strategy is run again, considering the new mass flow rate (Ahlbrink *et al.*, 2010a).

The purpose of this optimisation is to make use of the available power in the most optimal way possible during receiver operation.

### 2.4.7 BrightSource's Ivanpah solar thermal power plant: Heliostat field management

This 377 MW central receiver power plant is the largest plant of its kind in the world (BrightSource, 2013). Ivanpah makes use of the BrightSource developed SFINCS (Solar field integrated control system) as a method of heliostat field management. Optimisation of heliostat aim points is done by means of a closed-loop control system. Weather measurements in conjunction with cameras are used to provide references by which advanced algorithms can optimise the heliostat aim points in real-time (Bobinecz, 2012). The receiver consists of three parts namely the reheater (RH), evaporator and the superheater (SH), each with flux limits of  $150 \text{ kW/m}^2$ ,  $600 \text{ kW/m}^2$  and  $300 \text{ kW/m}^2$  consecutively as shown in Figure 2.7 (Koretz, 2014). The main objective of the aiming strategy is to maximize the solar energy input to the receiver within the flux limitations.

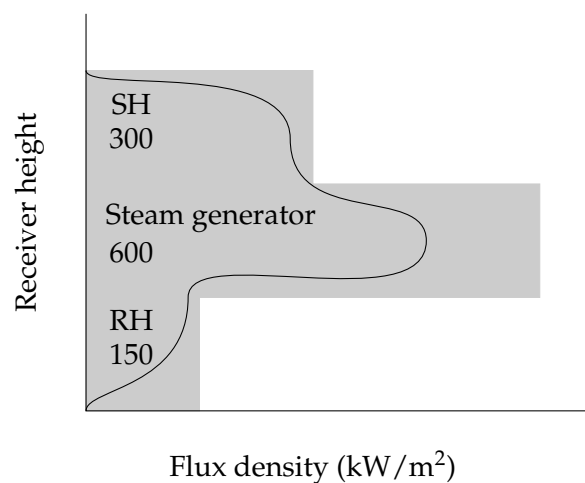


Figure 2.7: Flux distribution over the Ivanpah receiver (adapted from Koretz, 2014)

## 2.5 Conclusion

Through the literature review, it is determined that several aiming strategies exist for the different types of receivers both commercially and experimentally. It is however noted that the amount of published literature on aiming strategies, particularly strategies used in commercial plants, appears to be limited. Although the aiming strategies have been developed for larger systems, it is uncertain how they will perform on small experimental plants. The influence of flux prediction methods on aiming strategies needs to be evaluated and the various prediction methods compared with one another. The aiming strategies described in the literature review gave the insight needed to develop the research design.

In the next chapter, the research design as well as the methodology behind the analysis of the flux prediction methods and the aiming strategy is discussed.

## Chapter 3

# Method

The following section introduces the method and details each step of the research process. The basic principles and details regarding the case studies used are also presented.

### 3.1 Research design

Figure 3.1 presents a logic flow diagram of the method in this thesis leading from research to analysis and implementation. Initially a literature review was done on both the optical system and published aiming strategies. An understanding of central receiver systems and aiming strategies was necessary to develop the basic knowledge upon which this thesis is built.

A model was developed in Matlab (The Mathworks Inc., 2014) and linked to the ray tracing software tool, SolTrace (Wendelin *et al.*, 2012), to simulate the flux distribution on the receiver. Analytical methods of flux approximation were incorporated into this model due to computational expense. By comparing the flux distribution produced by the ray tracer and the analytical methods, the use of the analytical methods in the optimisation procedure was validated.

An aiming strategy was developed based on the work of Salomé *et al.* (2013) and Besarati *et al.* (2014). Their aiming strategies use the approximation of the flux distribution as a circular Gaussian distribution. The final developed aiming strategy is a combination of elements from both of these aiming strategies to produce a more robust method. To show how the aiming strategy performs for different systems, the method was applied to three case studies.

Theoretical validation of the analytical flux mapping and optimisation methods was done using the ray tracer software. However, to investigate the results of an aiming strategy on a realistic system, the strategy was implemented on an experimental test rig.

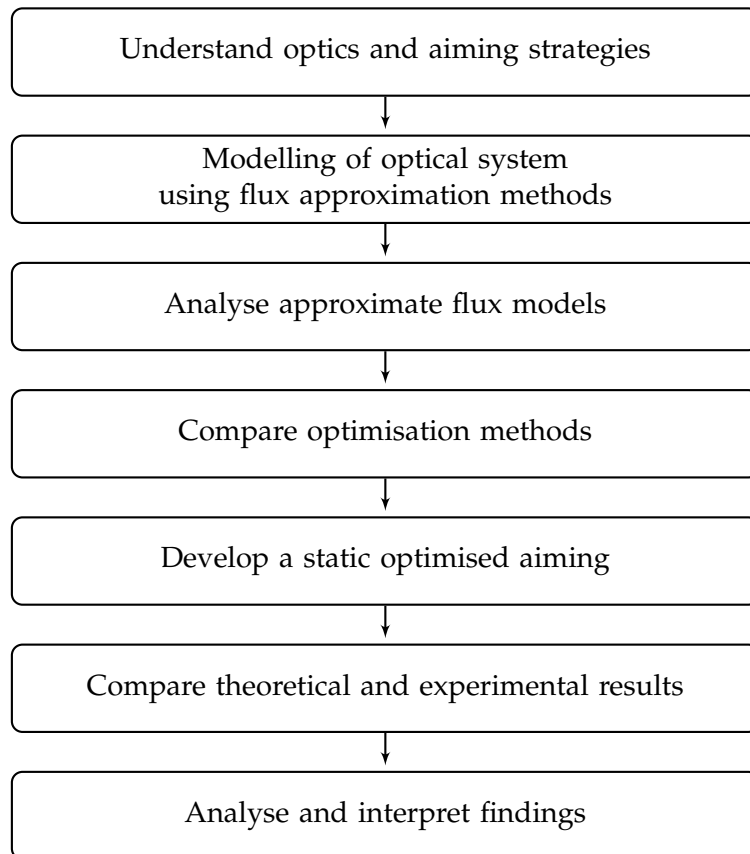


Figure 3.1: Research flow diagram

## 3.2 Methodology

Aiming strategies generally require theoretical flux distribution predictions to determine the optimal flux distribution across the receiver before operation. It is, therefore, ideal to have accurate results with low computational time as large amounts of data are processed. The following section describes the methodology of the flux mapping methods and the development of the aiming strategy.

### 3.2.1 The heliostat and receiver model

The use of ray tracing as an optical modelling tool provides flux distribution predictions accurate enough for most practical purposes. A model was developed using ray tracing to validate the analytical flux prediction methods. To simulate a specific system, the model requires various inputs. These inputs include:

- Location - Date and time; longitude, latitude and altitude
- Heliostats - Heliostat positions in the field, size and shape of heliostats, optical errors, reflectivity and type of tracking mechanism
- Receiver - Receiver position, shape and size; and optical characteristics

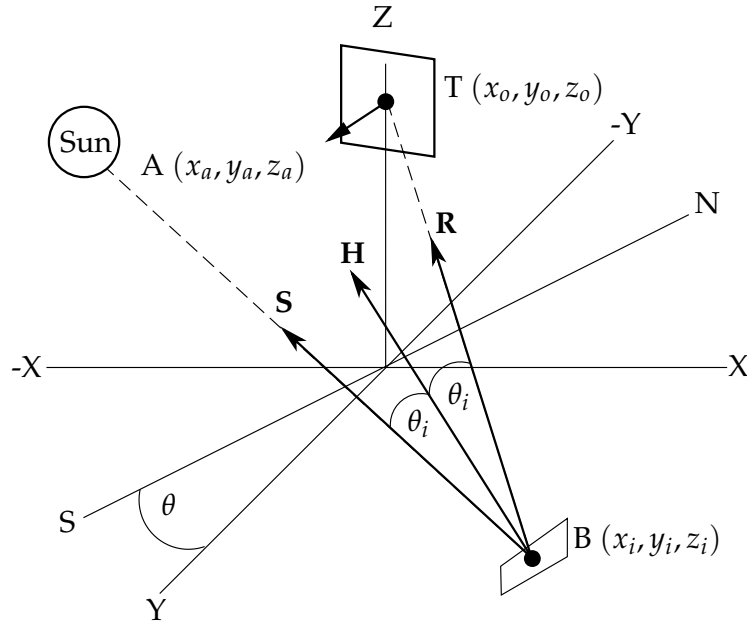


Figure 3.2: Coordinate system used in the model

The model inputs are standardised according to a specified coordinate system. The heliostats and target are positioned in a global coordinate system as depicted in Figure 3.2 with coordinates  $\mathbf{B}$  and  $\mathbf{T}$  being the corresponding positions of the heliostats and target. For a North facing field, South would be situated on the positive y-axis. However, for some smaller systems in restrictive areas, the heliostat field could be rotated with regards to North. Therefore the angle of field rotation  $\psi$  has been set in place to rotate the heliostat and receiver system accordingly.

After defining the coordinate system, the position of the sun is found using the NREL solar algorithm developed by Reda and Andreas (2004). The algorithm is used for calculating the azimuth ( $A$ ) and zenith ( $Z$ ) angles of the sun's position for the specified time. A unit vector  $\mathbf{S}$ , representing the sun's position in the coordinate system, is created from the azimuth and zenith angles using

$$\mathbf{S} = S_x \mathbf{i} + S_y \mathbf{j} + S_z \mathbf{k} \quad (3.2.1)$$

where

$$S_x = \sin Z \sin A \quad (3.2.2)$$

$$S_y = \sin Z \cos A \quad (3.2.3)$$

$$S_z = \cos Z \quad (3.2.4)$$

The vector from the origin of the coordinate system to the sun's position is known as the solar vector. The ray tracer represents the sun as a disc perpendicular to the solar vector which initiates rays in varying angular intensities relative to the sun-shape.

SolTrace allows the user to choose between a Gaussian, Pillbox or user defined sunshape. For a Gaussian sunshape, the radial intensity across the solar disk varies according to a normal distribution. Specific geographic locations have different measured values of standard deviations for Gaussian sunshapes (Collado *et al.*, 1986). However, the use of this sunshape is not recommended unless large errors are present within the rest of the system (Wendelin *et al.*, 2013).

The Pillbox sunshape has the same intensity over the entire disk and serves as an appropriate sunshape for use with lower concentrations of flux (Lovegrove and Stein, 2012). A realistic sunshape is something between a Pillbox and Gaussian shape (Wendelin *et al.*, 2013). An analysis of the different sunshapes is presented in Chapter 4.

The model is developed such that any unique central receiver system can be modelled. The position of each heliostat  $(x_i, y_i, z_i)$  in the coordinate system is imported from a comma separated value file. The position of the centre of the target  $(x_o, y_o, z_o)$  and the target aim point  $(x_a, y_a, z_a)$  is declared. The target aim point determines the position of the target normal vector. For each heliostat the unit vector between the heliostat and the target centre is calculated as

$$\mathbf{R}_i = \frac{(x_o - x_i)\mathbf{i} + (y_o - y_i)\mathbf{j} + (z_o - z_i)\mathbf{k}}{\sqrt{(x_o - x_i)^2 + (y_o - y_i)^2 + (z_o - z_i)^2}} \quad (3.2.5)$$

The unit normal vector ( $\mathbf{H}$ ) is defined as the vector bisecting the incident ray ( $\mathbf{S}$ ) and the reflected ray ( $\mathbf{R}$ ). The angle between the unit normal vector and the incident ray is equal to the angle between the unit normal vector and the reflected ray according to the law of reflection. The incidence angle is thus described as

$$\cos 2\theta_i = \mathbf{S} \cdot \mathbf{R} \quad (3.2.6)$$

The unit normal vector of the reflective area is determined by

$$\mathbf{H} = \frac{\mathbf{R} + \mathbf{S}}{2 \cos \theta_i} \quad (3.2.7)$$

The unit normal vector and the incidence angle of each heliostat is needed for modelling in both the ray tracer and analytical flux approximation methods.

### 3.2.2 Determining the flux distribution using ray tracing

A validation of the analytical flux approximation methods is done using the ray tracer. Inputs are sent to the SolTrace ray tracer using the developed Matlab simulation model. The ray tracer sends the positions of the hit points of the rays on the receiver back to the Matlab simulation model where it is evaluated and a flux map determined. The process of ray tracing is explained in Chapter 4.

### 3.2.3 Circular Gaussian flux approximation

Ray tracing is an accurate method of determining the flux distribution on a receiver. However, making this determination is computationally expensive especially with

large systems. Aiming strategies often require thousands of iterations to optimise the flux distribution. If ray tracing is required for each iteration, the optimisation method becomes impractically time consuming. In this case approximation of the flux distribution would be preferred.

Recent publications of aiming strategies have suggested the use of the HFLCAL method to approximate the flux distribution of a heliostat. HFLCAL describes the flux density profile of a heliostat as a single circular Gaussian distribution (Collado, 2010) as previously shown in Figure 2.3. Such a description allows the development of an analytical mathematical model of the flux distribution contributed by each heliostat. The individual distributions are superimposed to produce the final flux distribution produced by all heliostats.

The flux at any point  $(x, y)$  of the receiver for a single heliostat is described by

$$\text{FD}(x, y) = \frac{P_h}{2\pi\sigma_{\text{HF}}^2} e^{-\frac{(x^2+y^2)}{2\sigma_{\text{HF}}^2}} \quad (3.2.8)$$

The power provided to the receiver by a single heliostat is included in the flux density equation and can be determined by

$$P_h = I_D A_m f_{\text{at}} \rho \cos \phi \quad (3.2.9)$$

where  $I_D$  is the direct normal irradiance of the sun in  $\text{kW}/\text{m}^2$ ,  $A_m$  is the reflective area of the heliostat,  $\cos \phi$  is the cosine of the angle between the incidence rays of the sun and the heliostat normal vector,  $f_{\text{at}}$  is the attenuation factor and  $\rho$  is the reflectivity of the mirror.

The effective deviation,  $\sigma_{\text{HF}}$ , used in the flux density function is an error function which consists of the sunshape error  $\sigma_{\text{sun}}$ , the beam quality  $\sigma_{\text{bq}}$  which relates to the slope error, the astigmatic error  $\sigma_{\text{ast}}$  and the tracking error  $\sigma_{\text{t}}$ .

The combination of these four Gaussian errors in combination with the slant range  $D$  and the cosine of the angle between the receiver normal vector and the reflected ray ( $\cos \phi_{\text{rec}}$ ) gives the expression of  $\sigma_{\text{HF}}$  as

$$\sigma_{\text{HF}} = \sqrt{\frac{D^2(\sigma_{\text{sun}}^2 + \sigma_{\text{bq}}^2 + \sigma_{\text{ast}}^2 + \sigma_{\text{t}}^2)}{\cos \phi_{\text{rec}}}} \quad (3.2.10)$$

Deviations from the ideal mirror curvature is accounted for by the beam quality which could be defined as

$$\sigma_{\text{bq}}^2 = 4\sigma_{\text{SSE}}^2 \quad (3.2.11)$$

with  $\sigma_{\text{SSE}}$  as the surface slope error. The surface slope error for the HFLCAL model is found through an iterative process. First the maximum flux is measured for different solar angles. The surface slope error of the modelled distribution is then varied until the calculated peak flux matches the measured flux value (Guo and Wang, 2011).

The assumption is made that the respective heliostats in the model have a spherical surface shape with a radius twice the size of the focal length of the mirror (Igel and Hughes). The slant range is also assumed to be the same as the focal length for simplification purposes. The astigmatic error is calculated using the tangential ( $h$ ) and sagittal ( $w$ ) dimensions of the image produced by the heliostat in the receiver:

$$\sigma_{\text{ast}} = \frac{\sqrt{\frac{1}{2}(h^2 + w^2)}}{4D} \quad (3.2.12)$$

The image dimensions are calculated as:

$$h = D \left| \frac{d}{f} - \cos(\phi) \right| \quad (3.2.13)$$

$$w = D \left| \frac{d \cos(\phi)}{f} - 1 \right| \quad (3.2.14)$$

To find the total flux distribution using the analytical approximation method, the receiver needs to be divided into a grid. The smaller the size of the segments, the higher the resolution will be of the flux map. However, a good trade-off should be found between the resolution and computational expense. The model determines the flux density for each heliostat at the  $x$  and  $y$  locations in the centre of each section. The total flux density in each section is determined by the summation of the fluxes contributed by each heliostat.

### 3.2.4 Gaussian mixture model flux approximation

The first method considered to improve the analytical approximation method is replacing the circular distribution of the Gaussian model with the rotated elliptical distribution of the bivariate Gaussian model. This model consists of two standard deviation parameters,  $\sigma_x$  and  $\sigma_y$  in two dimensions. An illustration of the flux distribution created by a bivariate Gaussian model is shown in Figure 3.3.

As seen in Figure 3.4, the image reflected by an imperfect heliostat can often not be modelled accurately using a bivariate Gaussian model. In such instances the use of Gaussian mixture model (GMM) methods is suggested. Gaussian mixture models consist of several bivariate Gaussian models superimposed onto one another as seen in Figure 3.5. Using the GMM method to create a flux distribution appears to provide a better fit for images at high incidence angles and imperfect mirror surfaces. This method appears to be novel to analytical flux approximation methods for central receiver systems and no publications have been found.

The Matlab statistical toolbox includes a function which fits a Gaussian mixture model over a specific distribution. Before the function can be applied, an accurate flux density distribution is needed to fit the GMM. The flux distribution of a heliostat is first determined by the ray tracer for a specific sun position. In each case the DNI will be set to 1 kW/m<sup>2</sup>. The GMM function then tries to find the best fit for the distribution. Each flux distribution will be made up of a different number of bivariate models depending on their shape. The GMM fitting method is further

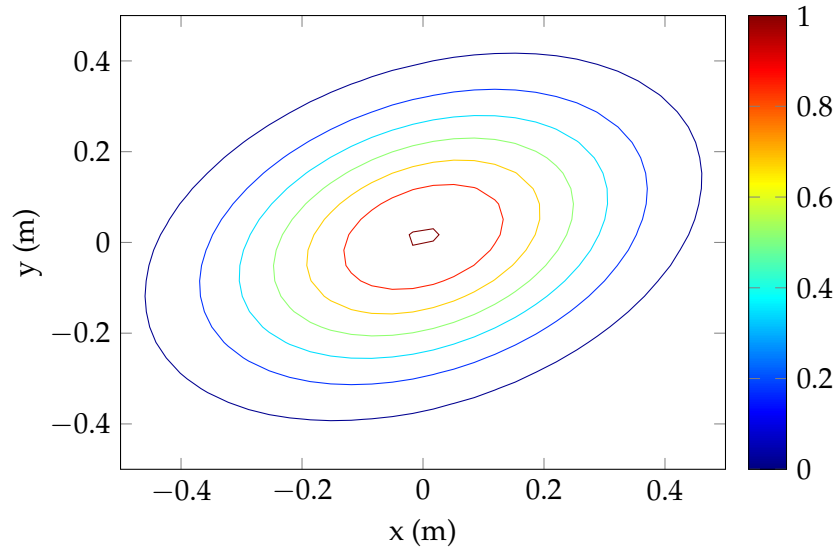


Figure 3.3: Example of contour plot of bivariate Gaussian model



Figure 3.4: Reflected image of experimental heliostat

described in Appendix A.

When the best fit is found the mean vector and the covariance matrix is determined as

$$\mu = \begin{bmatrix} \mu_x \\ \mu_y \end{bmatrix} \quad (3.2.15)$$

$$\Sigma = \begin{bmatrix} \sigma_x^2 & \rho\sigma_x\sigma_y \\ \rho\sigma_x\sigma_y & \sigma_y^2 \end{bmatrix} \quad (3.2.16)$$

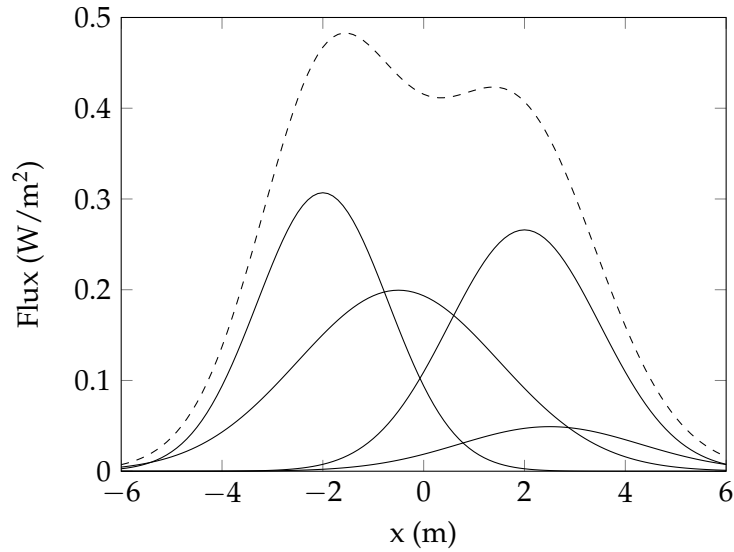


**Figure 3.5:** Example of superimposing of bivariate Gaussian models (Solid lines) to form a Gaussian mixture model (Dotted lines)

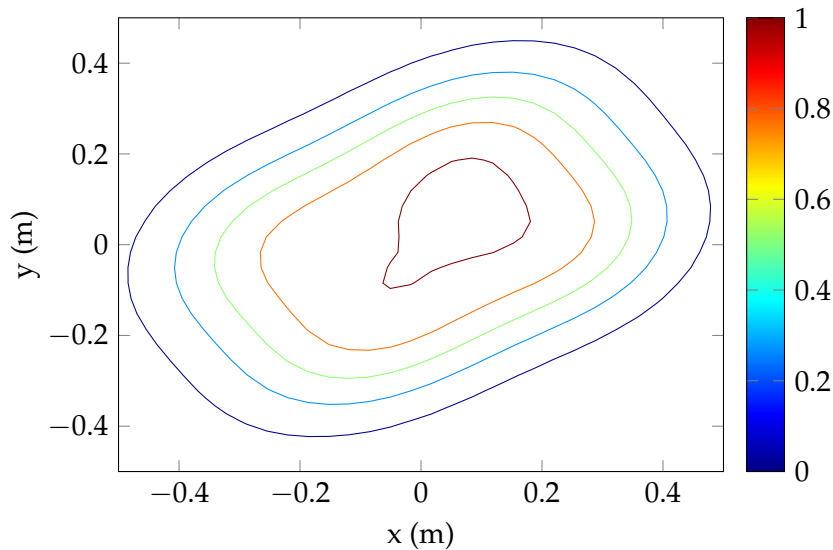


**Figure 3.6:** Example of contour plot of Gaussian mixture model

From the values obtained in these matrices the parameters  $\sigma_x$ ,  $\sigma_y$  and  $\rho$  can be found and then recorded in a database for each heliostat for specific solar positions. When the flux distribution is needed for an aiming strategy, these parameters are loaded into the Matlab model. For a number of  $t$  bivariate models, the total flux distribution model can then be calculated using

$$FD(x, y) = \sum_{n=1}^t A_n e^{B_n} \quad (3.2.17)$$

with

$$A_n = \frac{1}{2\pi\sigma_x\sigma_y\sqrt{1-\rho^2}} \quad (3.2.18)$$

and

$$B_n = \left( -\frac{1}{2(1-\rho^2)} \left[ \frac{(x-\mu_x)^2}{\sigma_x^2} + \frac{(y-\mu_y)^2}{\sigma_y^2} - \frac{2\rho(x-\mu_x)(y-\mu_y)}{\sigma_x\sigma_y} \right] \right). \quad (3.2.19)$$

The approximate flux density distribution is found by means of discretising the receiver surface and finding the flux at the locations of the sections.

### 3.2.5 The static aiming strategy

The literature review found that aiming strategies can either be predictive (open loop) or adaptive (closed loop). In either of the cases, the static optimisation of the flux is required. Although seemingly simple, the optimisation method can become highly complex. The optimisation problem in this case is to find heliostat/aim point combinations such that flux distribution is as even as possible. The ability of aim point positions to be located at any point on the receiver, introduces an infinitely large search space. To reduce the search space to a reasonable size requires fixing the aim points to certain positions. For a heliostat field with  $n$  heliostats and  $m$  aimpoints, the search space size is defined as

$$S = n^m \quad (3.2.20)$$

This type of problem appears to fall into the category of NP-HARD problems, such as the knapsack or travelling salesman problems Salomé *et al.* (2013). There exist two types of optimisation methods: algorithms considering evaluations of the functions and algorithms that call for both functions and their derivatives (Bland, 1993). Optimisation methods using a finite number of solutions such as combinatorial optimisation should be used in this case.

The developed aiming strategy is designed to obtain a certain flux density distribution on the receiver. It should be noted that this developed method considers only static aiming of the heliostats. Continuous aiming will be discussed in Chapter 8. The static aiming strategy method is an adaptation of the aiming strategies using the Tabu search method developed by Salomé *et al.* (2013) and the Genetic algorithm method by Besarati *et al.* (2014). The developed aiming strategy can be modified for each different heliostat field and receiver system.

Aim points are created in a grid form on a specified percentage area of the receiver as seen in Figure 3.7. The number of aim points, in either one- or two-dimensions, could be changed according to the needs of the system.

An objective function is required to determine the quality of the flux distribution. A flux distribution with a high quality will contain very low flux gradients over its area. The objective function for each optimisation method is discussed in Chapters 5 and 6.

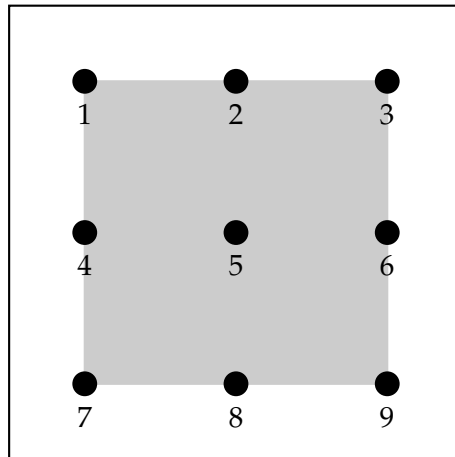


**Figure 3.7:** An example of the receiver aim point positions with the aim area in gray

The amount of power lost through the application of the aiming strategy also needs to be specified. The percentage of allowable power loss could either be specified or determined using the minimum allowable thermal power absorbed by the receiver.

$$PL_{max} = \frac{P_{max} - P_{allowable}}{P_{max}} \quad (3.2.21)$$

Depending on the amount of heliostats, the receiver size and the size of the reflective images, the specified power loss might restrict the homogenisation of the flux distribution. In this study, the effects of specifying a maximum power loss are discussed in Chapter 8.2.

The flow of the developed aiming strategy can be seen in Figure 3.8. The Matlab platform imports the data required for the performance of the aiming strategy. The heliostat and aim point positions are sent to the ray tracer, and the specific flux distribution for that time is determined. A GMM must now be fitted onto the flux density distribution of each heliostat as described previously. After determining the parameters used to build up each model, the parameters can be saved in a database. When static optimisation is required the data is imported into the Matlab simulation platform and used to determine the flux distribution.

Initially the flux distribution of all heliostats aimed at the centre of the receiver is required to determine the maximum cost function. The Tabu optimisation method is used to determine  $N_p$  random heliostat/aim point combinations known as populations. The Genetic algorithm is now performed on the acquired population to find the second generation. The best heliostat/aimpoint configuration from either the initial population or second generation is found, and a new initial population is then determined and the process repeated. If the new local best configuration is better than the global best configuration, the global best is replaced. Both optimisation methods are explained in detail in Chapter 5. The final aiming strategy is analysed in Chapter 6 and combines these optimisation methods.

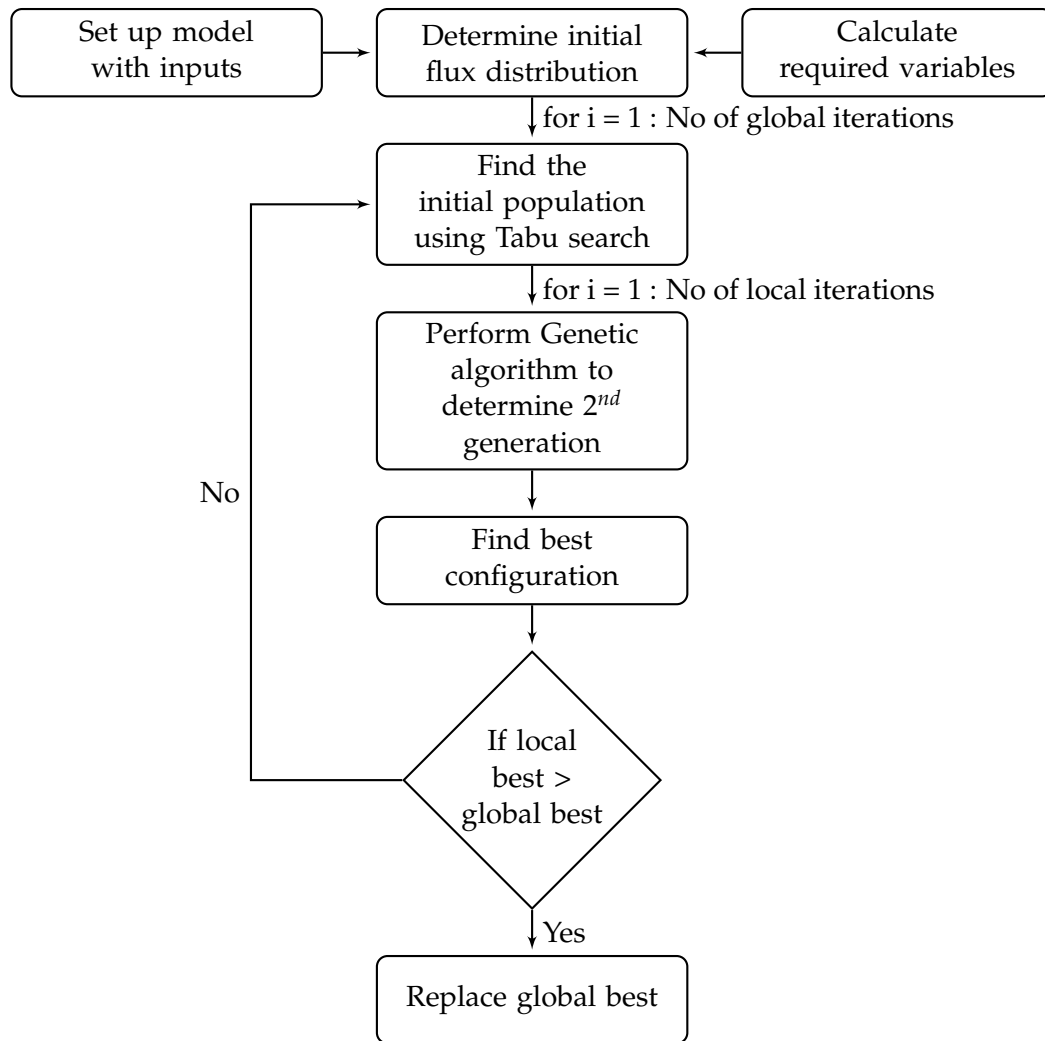


Figure 3.8: Flow diagram of combined optimisation strategy

### 3.3 Analysed systems

The following section details the characteristics of the three heliostat field and receiver systems used to analyse the aiming strategies in this thesis.

#### 3.3.1 Assumptions

The following assumptions are made regarding the considered case studies.

- The focal range is equal to the slant range for each heliostat
- The mirrors are ideal, meaning that they have a reflectivity of 1
- Surface slope errors are kept constant at 2 mrad, while tracking errors, specularity, wind loads, transmissivity and gravity loads are considered negligible.

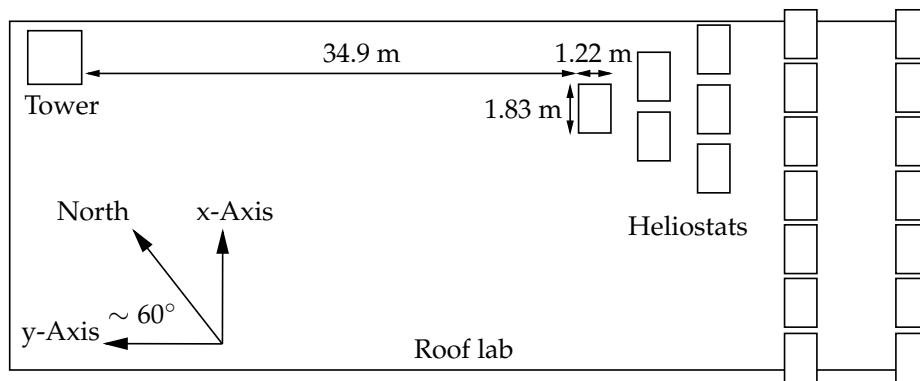


Figure 3.9: Layout of the experimental Helio40 heliostat field

### 3.3.2 Case study 1: Helio40

The Sasol Helio40 project is a small experimental heliostat and tower system built on the roof of the Mechanical Engineering Department at Stellenbosch University. This system consists of 20 heliostats arranged with 6 heliostats on the ground level and 2 sets of 7 heliostats on an upper level as seen in Figure 3.9. The space on the roof is restricted, allowing for the heliostat field to be built facing  $60^\circ$  west of north. The inputs used in this case study are provided in Table 3.1. Only vertical aim points were considered in this aiming strategy because of the small size of the heliostat field, thus representing only a small fraction of a total heliostat field aimed at a vertical segment of a cylindrical receiver.

Table 3.1: Inputs used in the Helio40 model

<b>Location</b>	Longitude	18.865
	Latitude	-33.928
	DNI	Fixed at $1 \text{ kW/m}^2$
<b>Heliostats</b>	Number of heliostats	20
	Surface slope error	2 mrad
	Aperture size	1.83 m x 1.22 m
	Angle of field rotation	$60^\circ$
<b>Receiver</b>	Position of receiver centre	[0 -1.268 12.342]
	Aim point	[0 -2.268 12.342]
	Size	1 m x 1 m
<b>Aiming</b>	Strategy	9 Vertical aim points
	Aim area	90 % of receiver
	Max power loss	@ 12h00 20 % of power
		@ 9h00 25 % of power

### 3.3.3 Case study 2: Helio100

Helio100 is a current project funded by the Technology Innovation Agency (TIA). The final layout consists of multiple heliostat field and receiver systems. These systems are in the developmental phase and will be used for further research in solar towers. For this thesis, a single heliostat field and receiver system was considered as seen in Figure 3.10 and 3.11. This system represents a small heliostat field aimed two-dimensionally at a flat plane receiver. The inputs used for this system are detailed in Table 3.2.

**Table 3.2:** Inputs used in the Helio100 model

<b>Location</b>	Longitude	18.865
	Latitude	-33.928
	DNI	Fixed at 1 kW/m <sup>2</sup>
<b>Heliostats</b>	Number of heliostats	100
	Surface slope error	2 mrad
	Aperture size	1.83 m x 1.22 m
	Angle of field rotation	0°
<b>Receiver</b>	Position of receiver centre	[0 0 10]
	Aim point	[0 -1 10]
	Size	0.7 m x 0.7 m
<b>Aiming</b>	Strategy	25 grid based aim points
	Aim area	90 % of receiver
	Max power loss	@ 12h00 15 % of power
		@ 9h00 20 % of power

### 3.3.4 Case study 3: PS10

Commissioned in 2007, PS10 is the first commercial solar tower in the world. This 11 MW tower consists of 624 heliostats as depicted in Figure 3.12. With its location in Seville, Spain, this heliostat field is classified as a South facing field. The inputs used for the modelling of this system are detailed in Table 3.3. Assumptions were made regarding this system because of a lack of information.

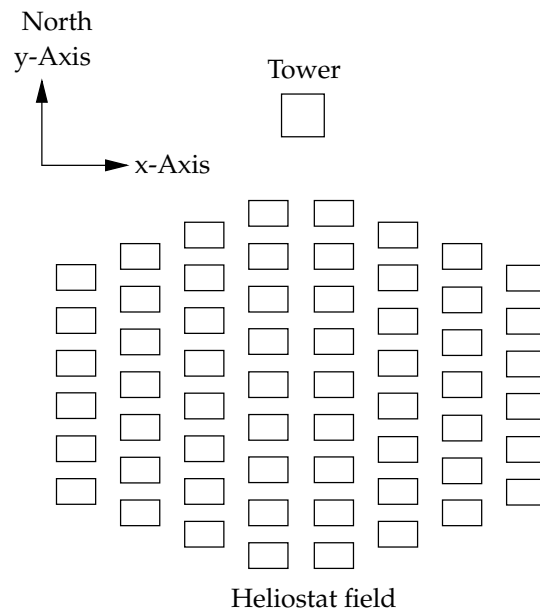


**Figure 3.10:** A proposed layout for the Helio100 system (not to scale)

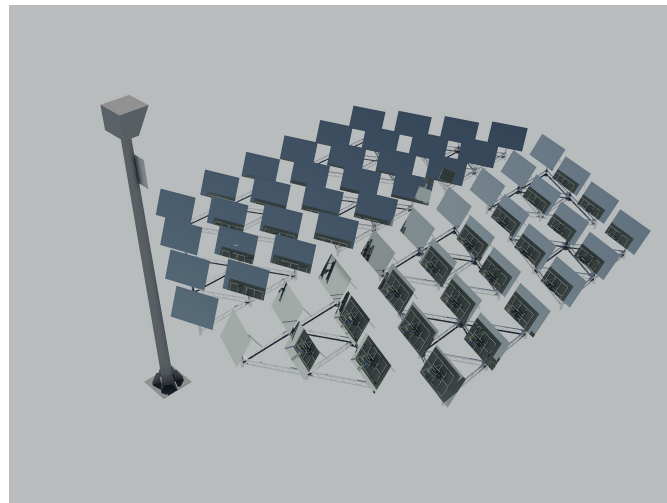


**Figure 3.11:** A proposed Helio100 layout (rendering by James Larmuth)

Table 3.3: Inputs used in the PS10 model

<b>Location</b>	Longitude	-6.254
	Latitude	37.442
	DNI	Fixed at 1 kW/m <sup>2</sup>
<b>Heliostats</b>	Number of heliostats	624
	Surface slope error	2 mrad
	Aperture size	7.82 m x 9.34 m
	Angle of field rotation	0°
<b>Receiver</b>	Position of receiver centre	[0 0 106]
	Size	14 m x 14 m
<b>Aiming</b>	Strategy	81 grid aim points
	Aim area	90 % of receiver
	Max power loss	@ 12h00 25% of power



Figure 3.12: PS10 field layout (Anon., 2008)

### 3.4 Computer specifications

All simulations are run on a standard personal computer. The computational speed of the simulations differs for different processors. The specifications of the computer are described in Table 3.4.

**Table 3.4:** Computer specifications

Processor	Intel(R) Core(TM) i7-2600 CPU @ 3.40 GHz
RAM	16 GB
System Type	64-bit Operating System

### 3.5 Conclusion

In this chapter the fundamental flux distribution prediction methods have been introduced. It is, however, important to understand what influences certain factors have on the predicted flux profiles and what level of accuracy could be expected from the predictive methods. The first step in the development of any aiming strategy is then to know the system variables and their effects on the system model.

In the next chapter the different flux prediction methods are discussed and compared.

## Chapter 4

# Analysis of flux distribution prediction methods

The performance of an aiming strategy is dependent on the accuracy with which a flux image can be predicted within the least amount of time. The computational expense and accuracy of the aiming strategy relies on the method used to predict the flux distribution on the receiver. In the following chapter, methods of flux prediction are analysed and compared. A substantial part of this chapter is based on the journal article submitted for publication: *Limitations of assuming a circular Gaussian flux density distribution for a single heliostat image* (Landman *et al.*, 2014). The work presented in this publication was done in cooperation with Willem Landman.

### 4.1 Ray tracing

One of the most accurate flux prediction methods is ray tracing. In the most basic form, ray tracing is the modelling of the physical path of photons of light in the form of rays from a specific source. It entails tracing the rays from the source to objects of either reflection or absorption. In this model, a ray is traced from the position of the sun in the coordinate system. In the ray tracing environment the sun is defined as a disc with a specific radial irradiance distribution defined as the sunshape. As a ray hits an object it is either reflected or absorbed according to the characteristics of the object. The new path of the ray is determined when a ray is reflected. Tracing continues until the ray is absorbed.

SolTrace (Wendelin *et al.*, 2012) was used as the ray tracer in this research because of its integration abilities with the Matlab simulation platform. Stages were modelled to represent objects in the ray tracer environment. For this research model, 3 stages were defined: the heliostat field stage, the target/receiver stage and the spillage stage as illustrated in Figure 4.1. Since locking of solar rays by the tower was not considered in this study, only the heliostat field was modelled in Stage 1. Rays hitting the heliostats are reflected relative to the value of the mirror reflectivity. A heliostat with a reflectivity of 0.9 will therefore reflect 90 % of the original rays. Reflected rays from Stage 1 are traced to the next stage. In this model, Stage 2 consists of the receiver, and Stage 3 represents the spillage plane, a flat plane positioned

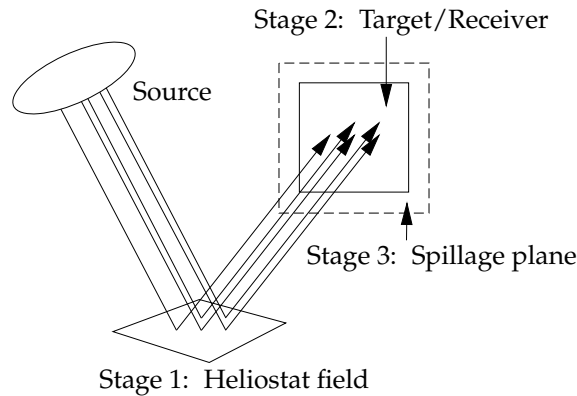


**Figure 4.1:** The three stages in the heliostat field and receiver model

just behind the receiver to absorb the rays that missed Stage 2. By calculating the amount of energy absorbed by the spillage plane, the amount of lost power can be determined. Rays which are not absorbed are neglected.

The receiver is placed in its position in the coordinate system with its normal vector directed perpendicular to the centre of the receiver plane. The model is able to handle both flat and cylindrical receivers; however, for the analysis of the aiming strategies, only a section of a cylindrical receiver was considered.

Heliostats in the field are modelled as spherical reflective planes and positioned within the coordinate system with regards to the  $x$  and  $y$  axes. At this stage the heliostats are modelled parallel to the horizon because tracking has not been incorporated. The ray tracer requires the aim point of the heliostat normal vector relative to the specific solar vector and receiver aim point position. The method used to determine the heliostat normal vector is described in Section 3.2.1.

The ray tracer positions the plane representing the heliostat to aim towards the determined aim point of the normal vector. At this point, the heliostat plane still needs to be rotated around the normal vector to account for the specific tracking mechanism. The angle of rotation around the heliostat normal vector is known as the  $z$ -rotation angle by the ray tracer. The Matlab model determines the  $z$ -rotation angle for three different tracking mechanisms: azimuth-elevation, fixed horizontal and target aligned tracking. The tracking mechanisms are explained in detail in Appendix C.

After the above mentioned inputs are sent to the ray tracer, a specified number of rays can be traced. The amount of rays used depends on the size of the system and the accuracy needed.

The ray tracer sends a comma separated value document to the Matlab model which contains the positions of each hit point in the system. The model separates the hit points that landed on the heliostats, the receiver and the spillage plane from one another. After sorting the rays, the 3D hit points are transposed to 2D points in

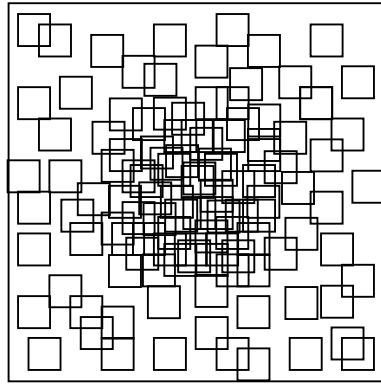


**Figure 4.2:** Illustration of binning box position over a receiver aperture

a local coordinate system. This allows the binning of the rays which hit the receiver using a binning strategy. Two binning strategies are considered for the model.

A grid or box binning strategy is the first strategy to be considered. The plane that contains the 2D positions of the ray hit points are divided into a grid. The rays within each section of the grid is added together and divided by the area of the section. This value is then multiplied with the value of the power per ray, which is an output of the ray tracer. An average flux density is therefore found for each section. By interpolating the values between the average flux densities of each section, a total flux map is found. The model makes use of the Delaunay triangulation method to produce the flux map for illustrative purposes. A detailed explanation of the Delaunay method is given in Appendix A.

The second binning strategy to be considered was developed by Landman (2013). The same method applies as for grid binning; however, the bins are randomly placed in positions that resemble a normal (Gaussian) distribution as seen in Figure 4.2. The flux in the centre of each bin is determined by adding all the rays inside the bin and dividing it by the area of the bin. Some rays may fall within various bins and will be counted in each respective bin. Due to the nature of flux maps in general it could be assumed that the biggest amount of flux lies within the centre and decreases towards the edges of the receiver. Because of the overlap of the bins, large spikes and valleys in the flux are avoided. In this thesis, the Gaussian binning strategy is used.

## 4.2 Computational expense

For the results of the ray tracer to be accurate, the number of rays used must be high enough. In this study it was determined that after 100 000 rays, minor deviation between the results of the different ray tracing executions could be found. The implementation of the ray tracer and interpretation of the results for 100 000 rays took approximately 30 seconds for a single iteration. On the other hand the analytical methods took only a fraction of a second to complete. When considering the optimisation of the flux distribution where several iterations are required, analytical

methods appear much more promising than the ray tracer. However, considering the accuracy of the analytical methods as opposed to the ray tracer, the analytical methods often do not produce results that are accurate enough. In the following sections the accuracies of the analytical methods are evaluated and the limitations of these methods highlighted.

### 4.3 The one-point fitting model

The HFLCAL approximation method described by Schwarzbözl *et al.* (2009) considers the approximation of a flux density distribution as a circular Gaussian distribution. The usability of this method was assessed by comparing results from the MIRVAL ray tracer and the HFLCAL approximation method. Although a good correlation between the results could be found for the intercepted power, the peak flux and standard deviation showed a large deviation between the ray tracer and HFLCAL method results for low surface slope errors. Schwarzbözl *et al.* (2009) state that the HFLCAL method is not an appropriate method for flux estimation when a detailed analysis of the flux distribution is required.

Following these results, Collado (2010) outlines an improvement of the HFLCAL approximation method called the one point fitting method. In the comparison done by Schwarzbözl *et al.* (2009) the same surface slope error is used for both the ray tracer and the HFLCAL approximation method. Collado's improved method adjusts the surface slope error used in the HFLCAL approximation model until the peak flux of the model closely matches the peak flux obtained from the ray tracer. In his publication, Collado compares the flux distribution obtained by the HFLCAL and UNIZAR approximation methods of 10 heliostats of the PS10 field to measured flux distributions. The radial position of the 90 % power intercept is used as an evaluation method which is determined by finding the radial distance and encompasses 90 % of the total power. Figure 4.3 shows the power over the radial distance as well as the positions of the 10 % and 90 % intercepts.

Three of the heliostats considered showed deviations of 7 %, 9 % and 9.3 % respectively between the measured and the approximate 90 % power intercepts. This could be attributed to the high incidence angles of these heliostats at the moment of measurement. The other heliostats had deviations between 3 % and 5 %. It is therefore seen that deviations between the measured and approximated results are found for high incidence angles. The results are published only for a single solar position and, therefore, do not provide enough information regarding the outcome. For this reason the following section includes a comparison of the improved HFLCAL approximation method for various cases.

### 4.4 The Landman-Grobler improvement method

The variations between the ray tracer and the HFLCAL approximation method was evaluated by Landman *et al.* (2014). It was found that for high incidence angles and large surface slope errors, the image in the sagittal plane was smaller than that of the tangential plane. However, since the HFLCAL approximation method predicts

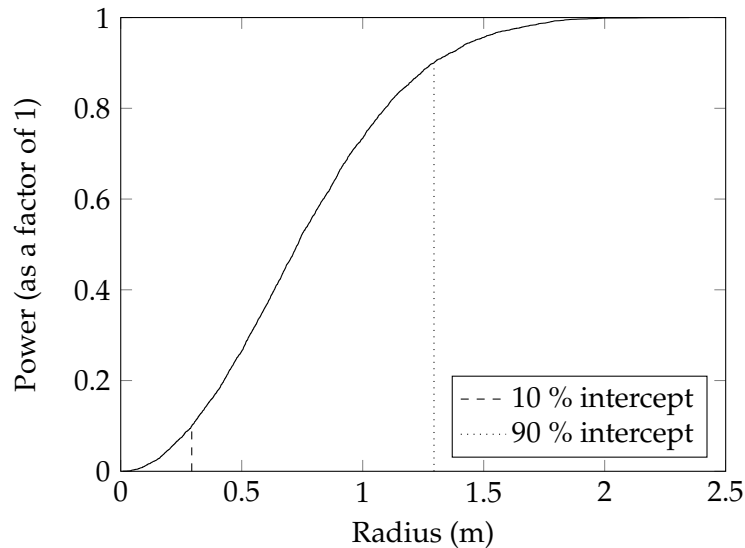


**Figure 4.3:** Standard deviations of radial images for different sunshapes

the flux distribution as a circular Gaussian distribution, the standard deviation is overestimated and a large deviation exists between the standard deviation of the ray tracer and the HFLCAL method in the sagittal plane. This phenomenon is explained in detail in Appendix B.

Landman *et al.* (2014) suggest that the standard deviation in both the sagittal and tangential plane be decreased to result in a closer fit to the ray traced image. The improvement of the HFLCAL method is done by lowering the standard deviation with regards to the increase in incidence angle by replacing the beam quality term in the equation of the standard deviation (Equation 3.2.10) with

$$\sigma_{bq}^2 = 4\sigma_{SSE}^2 \cos \phi \quad (4.4.1)$$

The effect of high incidence angles and large surface slope errors are further explained in Appendix C.

## 4.5 Analysis of a single heliostat

For this analysis a single heliostat and receiver system was modelled. The model is based on the model used by Schwarzbözl *et al.* (2009) to evaluate flux approximation using the HFLCAL method. Table 4.1 shows the inputs used in this model.

### 4.5.1 Sunshape

When modelling a system using the HFLCAL method, the sunshape is limited to a Gaussian sunshape due to the analytical nature of the model, despite that Gaussian sunshapes are the least accurate to use in most cases (Wendelin *et al.*, 2013). Ray

**Table 4.1:** Inputs used in the evaluation model

Heliostat size	1 m x 1 m
Heliostat position	[0,0,-100]
Receiver position	[0,0,0]
Normal of receiver	[0,0,-1]
DNI	1000 W/m <sup>2</sup>
Sunshape for ray tracing	Pillbox with half width of 4.65 mrad
Sunshape for HFLCAL	Gaussian with standard deviation of 2.24 mrad

tracers on the other hand allow any sunshape to be modelled. Figure 4.4 shows the normalized intensity distributions of the Gaussian, Kuiper and pillbox sunshapes. The Kuiper sunshape is often used in modelling because it is able to take on a combination of characteristics of the pillbox and Gaussian sunshape.

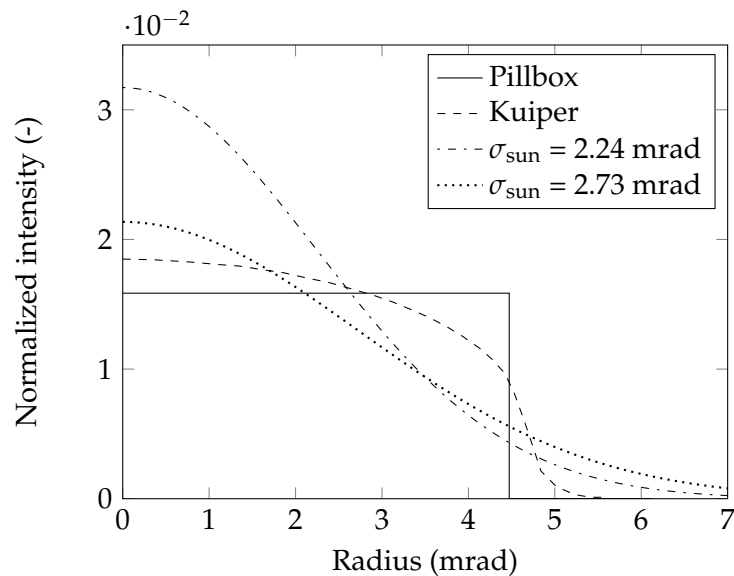


**Figure 4.4:** The normalized intensity distributions of different sunshapes (adapted from Schwarzbözl, 2009)

Since the HFLCAL model can only make use of a Gaussian sunshape, it is important to know at which standard deviation a Gaussian sunshape correlates with non-Gaussian sunshapes such as the pillbox and Kuiper sunshapes. The standard deviations of flux profiles were determined for different standard deviations of the Gaussian sunshape using the ray tracer and the HFLCAL method. They were then compared to the standard deviations of the flux profiles of the Kuiper and pillbox sunshape using ray tracing. The half-width of the pillbox image was taken as 4.65 mrad.

The standard deviations determined for the flux distributions using different sunshapes are shown in Figure 4.5. Although the standard deviations of the HFLCAL and ray tracer Gaussian sunshape were varied, the half-width of the Pillbox and standard deviation of the Kuiper sunshape were both kept constant.

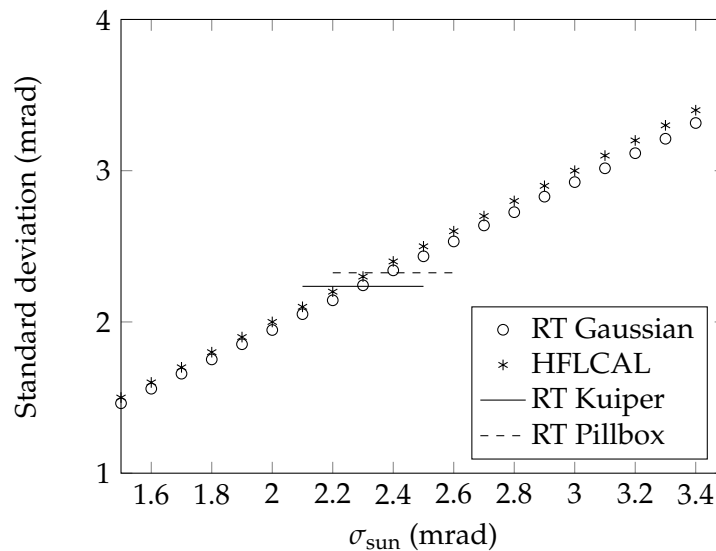


Figure 4.5: Standard deviations of radial images for different sunshapes

seen that the standard deviation of the flux profile of the Gaussian sunshape for both the ray tracer and HFLCAL method were close to one another. The standard deviation of the flux profile created using the Pillbox sunshape was close to a Gaussian sunshape with a standard deviation of 2.3 mrad. For the Kuiper sunshape, a Gaussian sunshape of 2.39 mrad had a similar flux profile standard deviation. However, the peak fluxes obtained for these similar sunshape standard deviations will differ because of the different intensities of the sunshapes. An analysis of the peak flux intensities and influencing factors of the flux profile are found in Appendix C. Up to now only the sunshape had been considered. When adding errors to the flux profile the intensity and shape will start to change.

#### 4.5.2 Surface slope errors

The surface of a mirror is never perfectly flat. Macro irregularities on the surface exist causing deviations of the normal vector at that point. This characteristic of the mirror is known as the surface slope error. Increasing the surface slope error causes a lowering of the maximum flux value, a distortion of the image and an increase in the standard deviation of the profile.

The system was evaluated at a small incidence angle of  $10^\circ$  for surface slope errors varying from 0 mrad to 5 mrad. As seen in Figure 4.6, at low incidence angles the standard deviation of the GMM method and the Landman-Grobler model was

closest to the ray tracer results followed by the HFLCAL model and finally the Collado model. The Collado method lowers the peak flux of the HFLCAL model until it matches the peak flux of the ray traced results by increasing the surface slope error. The one point fitting therefore causes a deviation from the standard deviation of the ray tracer. The GMM method was closest to that of the ray tracer model re-

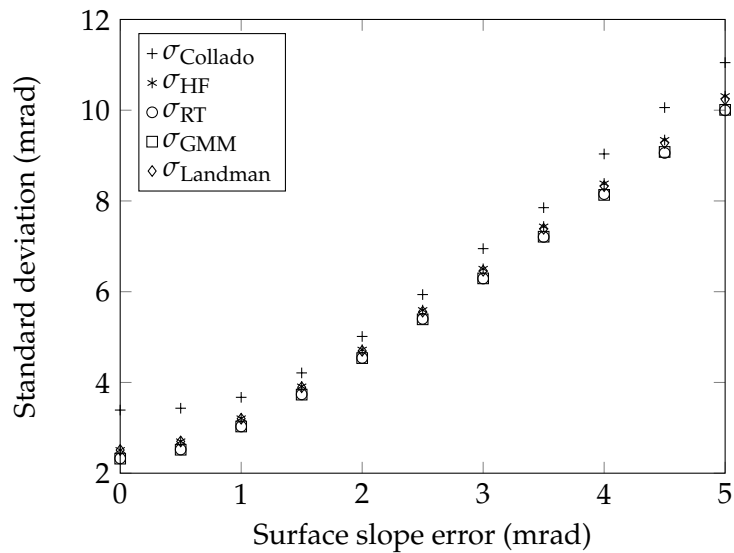


**Figure 4.6:** Standard deviation on the y-axis for a surface slope error variation at an incidence angle of  $10^\circ$

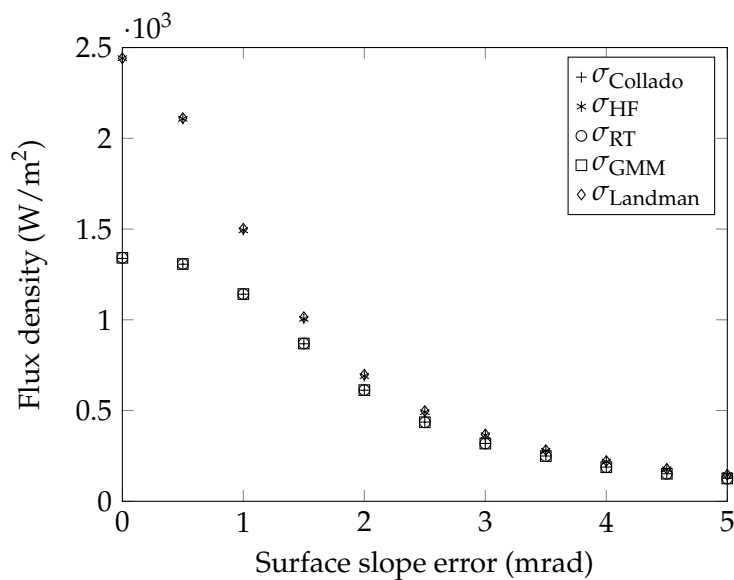


**Figure 4.7:** Peak flux for a surface slope error variation at an incidence angle of  $10^\circ$

garding both the peak flux and standard deviation. This could be attributed to the accurate fitting of each GMM to previously evaluated ray tracing results using the related heliostat characteristics. Figure 4.7 shows the peak flux values for the SSE variations. It was noticed that the HFLCAL and Landman-Grobler approximation produces a higher peak flux for the lower values of the SSE.

### 4.5.3 Incidence angle

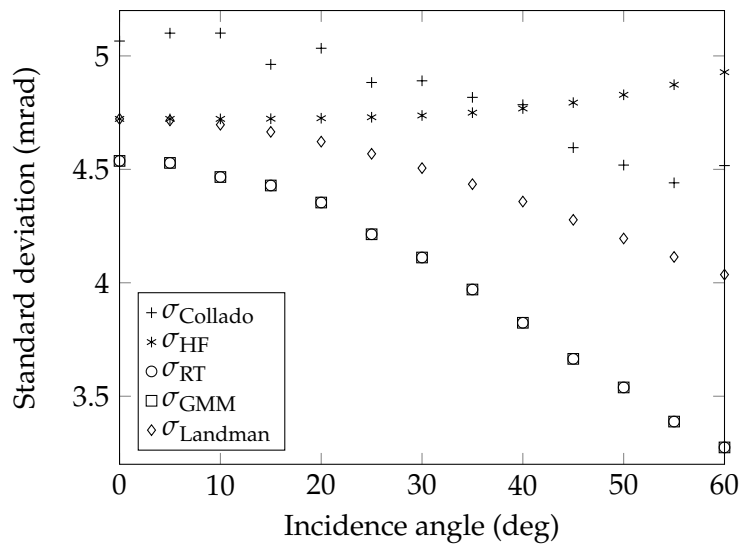
The variation of the incidence angle at a surface slope error of 2 mrad was considered. This surface slope error value was chosen because the minimum deviation caused by the surface slope errors between the approximate methods and the ray tracer exists at this value. As a result, focus was placed only on the deviations caused by the incidence angle.

Figure 4.8 shows the standard deviation of the flux profile in the sagittal plane. The standard deviation for the ray traced image became smaller as the incidence angle is increased. However, the standard deviation of the HFLCAL approximation method became larger with an increase in standard deviation. The Landman-Grobler improvement corrected this effect and followed a similar decrease in standard deviation as the ray tracer. The one point fitting method by Collado also followed a similar trend, but before an incidence angle of  $40^\circ$ , this method has a very large deviation from the ray traced results. The standard deviation of the GMM method was close to that of the ray tracer.

If the standard deviation for the tangential plane is considered as shown in Figure 4.9, it could be seen that the standard deviation increased with the increase in incidence angle for both the ray tracer and the HFLCAL approximate method. Conversely, the Collado and Landman-Grobler approximation was decreasing for the increase of the incidence angle.

## 4.6 Conclusion

It is now believed that for high incidence angles and high SSE there exists a large deviation between the flux distribution obtained by the ray tracer and the HFLCAL method. The HFLCAL method overestimates the flux density due to its inability to account for blocking and shading. However, the central limit theorem states that if a large number of errors exist in the system and when their deviations become large enough, the flux distribution will tend toward a Gaussian distribution. For small systems, such a distribution is detrimental to aiming strategies since the accuracy of flux distribution is greatly diminished. The GMM method provides an alternative approach to approximate flux distributions due to its ability to accurately fit analytical functions over numerical results.



**Figure 4.8:** Standard deviations of flux images for incidence angle variation for surface slope error of 2 mrad in the sagittal plane

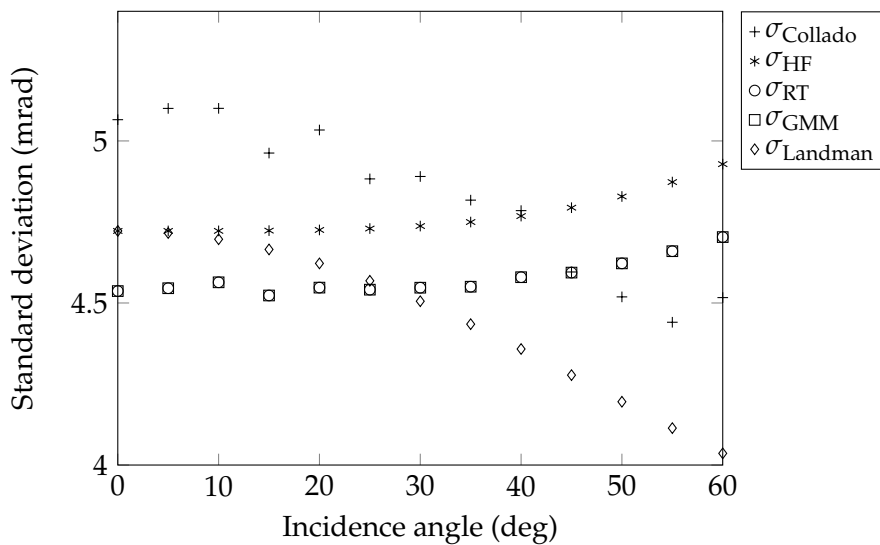


**Figure 4.9:** Standard deviations of flux images for incidence angle variation for surface slope error of 2 mrad in the tangential plane

## Chapter 5

# Optimisation methods for aiming strategies

Aiming strategies are developed based on four considerations: the heliostat and receiver system design, the method to predict the flux distribution, the optimisation method and the factors influencing the flux profile such as the time of day and DNI. Static aiming strategies depend on the method of optimisation to accurately and efficiently obtain the required heliostat/aim point combinations. In this chapter two optimisation methods are analysed: the Tabu search method and the Genetic algorithm.

### 5.1 Tabu search optimisation

The original heuristic Tabu search method was developed by Glover (1986). Flux distribution optimisation seems to be of the class of NP-HARD problems, and as a result, no exact solution can be found. Heuristic search methods providing approximate solutions for combinatorial optimisation are therefore suggested. The Tabu search algorithm is an adaptation of the hill climbing method (Burke and Kendall, 2005).

#### 5.1.1 Tabu search method

The basic principle of this strategy is to arbitrarily aim individual heliostats and evaluate their effects on the flux profile. Initially all the heliostats are aimed at the centre of the receiver. The cost function, also known as the objective function, needs to be minimised and is defined as the difference between the maximum and minimum flux on the receiver:

$$f_i = FD_{i,max} - FD_{i,min} \quad (5.1.1)$$

At each iteration a random heliostat is focussed on an arbitrary aim point. The cost function at the current iteration is then compared to the cost function of the previous iteration. If the cost function is improved and the power loss within the set bounds, the aim point for the specific heliostat is accepted. If not, the heliostat will go back to its previous aim point and a different heliostat is aimed at an arbitrary

**Figure 5.1:** Algorithm for the Tabu optimisation method

aim point. This procedure continues until the maximum amount of iterations is reached or the cost function converges.

Convergence might require a large amount of iterations or might not be reached at all. To improve the time needed for the function to converge, a Tabu chart is created. The maximum height and width of each heliostat image is determined by using the equations of Igel and Hughes (1979):

$$h = 2d_h \sin^2\left(\frac{\phi}{2}\right) + \beta_s r / 2 \quad (5.1.2)$$

$$w = 2d_w \sin^2\left(\frac{\phi}{2}\right) + \beta_s r / 2 \quad (5.1.3)$$

with  $d_h$  and  $d_w$  as the height and width of the heliostat respectively,  $\phi$  the incidence angle,  $\beta_s$  the subtending angle and  $r$  the heliostat radius of curvature. The percentage of the image area allowed over the edge of the receiver is set. A Tabu chart is set up by screening each heliostat/aim point combination to determine the amount of spillage produced when a heliostat is aimed at a specific aim point. The Tabu chart, as seen in Figure 5.2, is a matrix where the columns represent each heliostat, and the rows are the individual aim points.

Initially the matrix values are set to zero. If the spillage is more than the allowable limit, the value in the cell representing the heliostat/aim point combination is changed to one. When the heliostat/aim point combinations are chosen at random in the optimisation process, the heliostat/aim point combinations in the Tabu chart with a value of one will be forbidden. Figure 5.3 shows an example of a forbidden (left) and an acceptable (right) heliostat/aim point combination. The algorithm is summarised below:

```

SET Heliostat aim points = (0,0,0)
Calculate f_max using Equation 5.1.1
Calculate h and w using Equations 5.1.2 and 5.1.3
Generate the Tabu matrix
FOR i = 1:Number of iterations
Choose heliostat at random and aim at arbitrary aim point
Calculate f_i using Equation 5.1.1
IF f_i < f_max
f_max = f_i
ELSE
Move heliostat back to previous aim point
END
END

```

		Heliostats				
		1	2	...	n-1	n
Aimpoints	1	1	1	...	0	1
	2	1	0	...	0	0
	⋮	⋮	⋮	⋮	⋮	⋮
	m-1	1	0	...	1	1
	m	1	1	...	0	1

Figure 5.2: An example of the Tabu chart

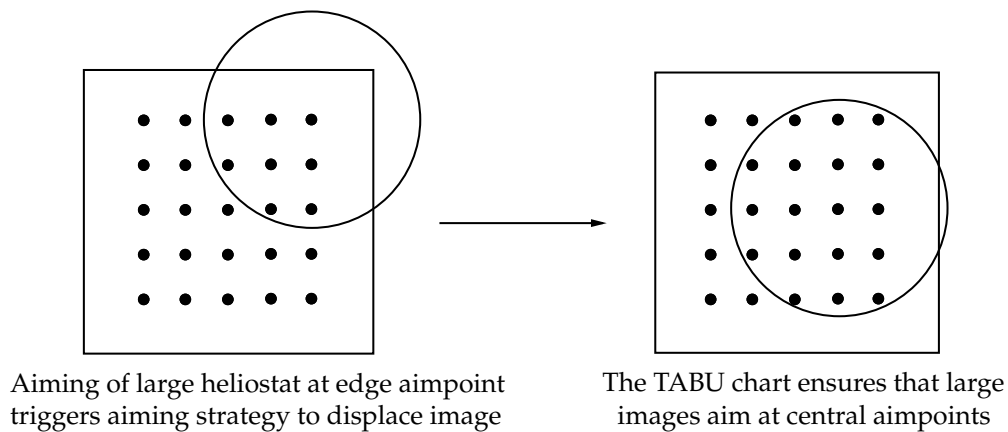


Figure 5.3: Illustration of the positioning of heliostats according to the Tabu model

### 5.1.2 Results

The Tabu search method was evaluated using the Helio40 and Helio100 heliostat fields. For each test the Collado adaptation of the HFLCAL approximation method was used in the aiming strategy. The objective of these tests was to determine the advantages and disadvantages of using the Tabu search method in conjunction with the adapted HFLCAL method as described in the published work of Salomé *et al.* (2013).

The first analysis was done for the Helio40 system at noon of the southern hemispheric summer solstice: 21 December 2014. The number of aim points was specified as nine vertical points over 90 % of the area with a maximum power loss of 20 %. These values have been determined through an iterative process to produce the best trade off between the homogeneity of the flux and the power loss.

Figures 5.4 and 5.5 show the flux distribution for central aiming on the left, illustrating that the Collado method aptly approximated both the peak flux and standard deviation of the ray tracer flux profile. After applying the Tabu search method, the peak flux was lowered by 50.9 % and the flux gradient significantly reduced as shown on the right of Figures 5.4 and 5.5. A final power loss of 19.6 % was determined for the Collado approximation and 20.7 % for the ray tracer.

The final maximum flux obtained by the Collado method was overpredicted by 1 % when compared to the ray tracer results.

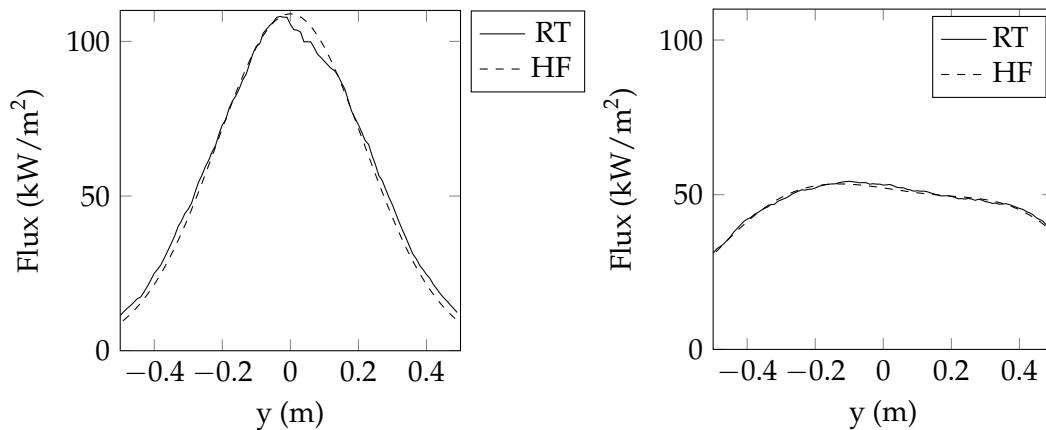


**Figure 5.4:** Flux map of the Helio40 system on 21 December at 12h00 before (left) and after (right) Tabu optimisation for the Collado approximation (HF) and the ray tracer (RT)

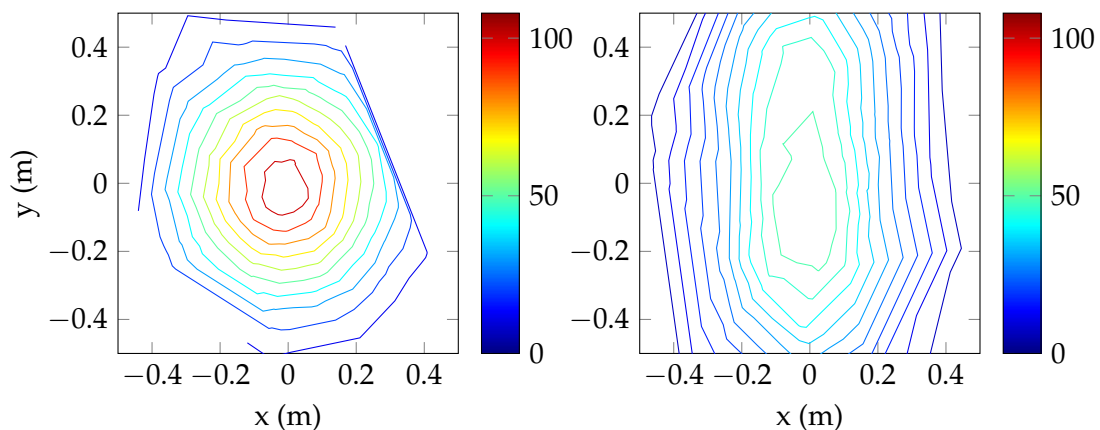


**Figure 5.5:** Contour plot of the Helio40 system on 21 December at 12h00 before (left) and after (right) Tabu optimisation

The Tabu search was then applied for 9h00 on the same day. For this time of day it can be assumed that the start up of the system is being implemented. At this time, large images and low fluxes are being dealt with because of high incidence angles in combination with low DNI values.

A higher risk of thermal stress exists because of a low receiver material temperature. As a result, a higher power loss limit can be accepted at this time of day. A peak flux limit relative to the outer and inner temperatures of the receiver material would have to be set to avoid excessive thermal gradients. For this research, homogeneity of the flux was prioritised, and flux limitations were not taken into account. An allowable power loss of 25 % was assumed in this test. Although the test was not based on realistic values, it provides a representation of how the aiming strategy would be implemented for a real life case at start up. Figures 5.6 and 5.7 show that the ray traced image already had a lower flux gradient and peak flux value. The flux profile of the Collado model indicated a poor correlation to the ray traced results likely due to of the high incidence angles.

After the implementation of the aiming strategy, the flux profile determined by the ray tracer had a lower flux gradient and peak flux. The maximum power loss for both the ray tracer and the Collado methods was below the limit at 24.5 % and 24.6 % respectively. The Collado method underestimated the peak flux by 21 %. An underestimation of the peak flux by the approximate method of this magnitude could be detrimental to a system because the actual flux might be higher than is allowed. It is thus suggested that a circular Gaussian flux distribution should not be used at high incidence angles. This result ties in with the findings from Chapter 4.

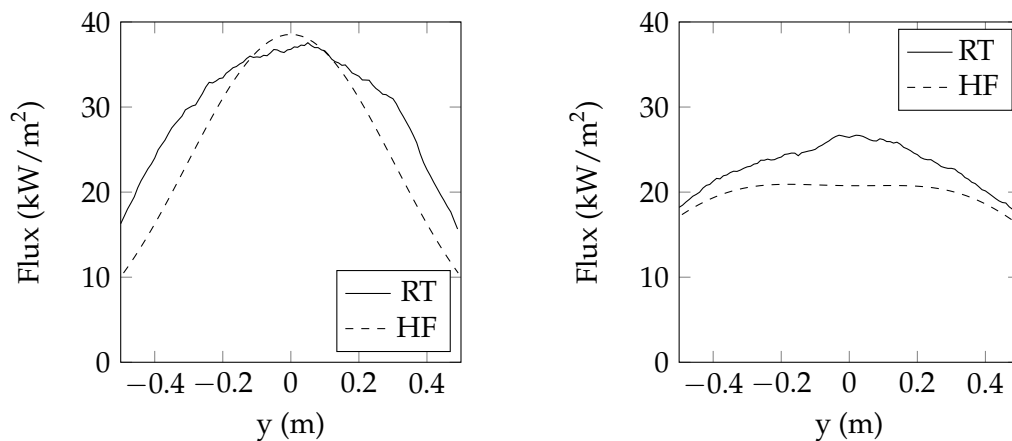


**Figure 5.6:** Flux map of the Helio40 system on 21 December at 9h00 before (left) and after (right) Tabu optimisation

The Helio100 heliostat field was also evaluated for the 21st of December 2014 at 12h00 and 9h00. The optimum aim area was determined as 75 % of the total area for 15 % maximum power loss at 12h00 and 20 % maximum power loss at 9h00. The aiming strategy was first run for 12h00. From the graph on the left of Figure 5.8 it can be seen that the Collado model adequately approximated the flux profile. The figure on the right of Figures 5.8 and 5.9 shows that the aiming strategy produced a low gradient homogenised flux profile as required, and the peak flux lowered by 86 %. For this test the determined power loss of the ray traced profile was 15.5 %

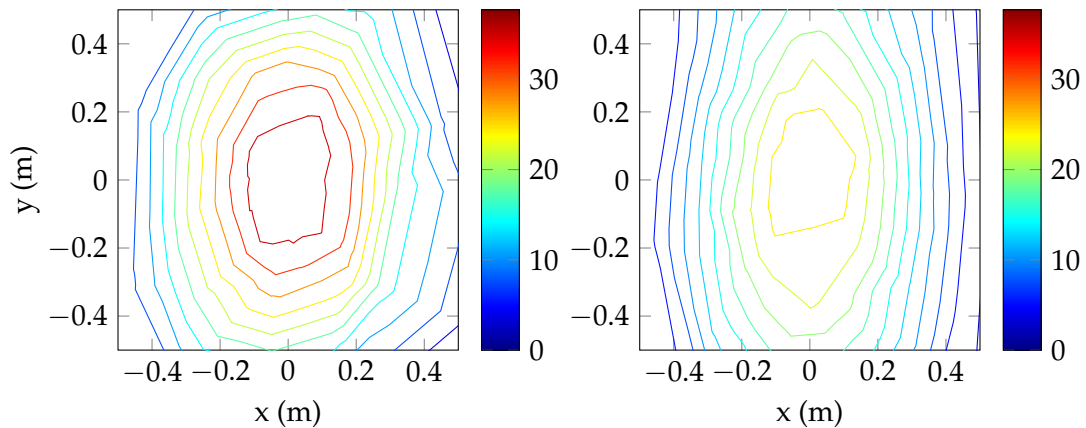


**Figure 5.7:** Contour plot of the Helio40 system on 21 December at 9h00 before (left) and after (right) Tabu optimisation

as opposed to the 14.9 % power loss obtained for the Collado approximation. The final peak flux was overestimated by 3.9 % by the Collado approximation method.

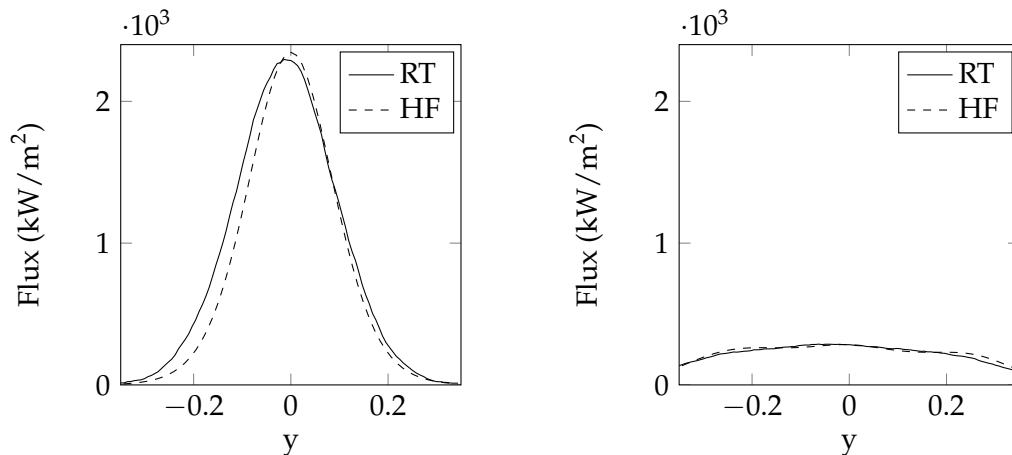


**Figure 5.8:** Flux map of the Helio100 system on 21 December at 12h00 before (left) and after (right) Tabu optimisation

At 9h00 the Helio100 aiming strategy showed similar results to the previous test at 12h00. Figures 5.10 and 5.11 show the flux distributions before and after the implementation of the aiming strategy. As opposed to the Helio40 system that experiences low flux gradients early in the morning, the Helio100 system experiences high flux gradients. After the aiming strategy, the flux was lowered by 69 % and a power loss of 20 % and 20.4 % was obtained for the approximate method and the ray tracer results respectively. The peak flux was overestimated by 9 % by the approximate method.

The high initial flux gradients can be attributed to the Helio100 system experiencing incidence angles below  $35^\circ$  at this time of day. The high peak flux values

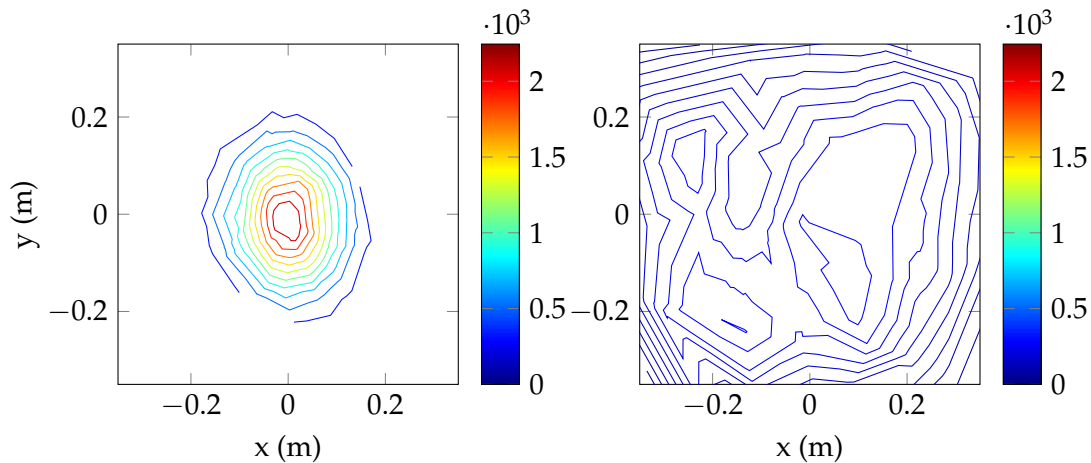


**Figure 5.9:** Contour plot of the Helio100 system on 21 December at 12h00 before (left) and after (right) Tabu optimisation

contributed by each heliostat makes it difficult to obtain an even flux distribution without a considerable amount of lost power.

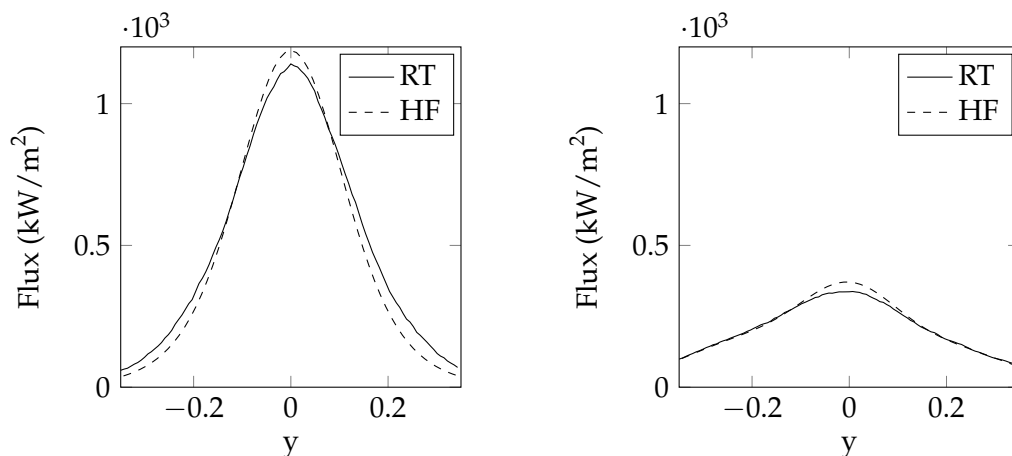


**Figure 5.10:** Flux map of the Helio100 system on 21 December at 9h00 before (left) and after (right) Tabu optimisation

### 5.1.3 Analysis of the Tabu method

The Tabu method provided a computationally inexpensive method of obtaining a homogenised flux distribution. Approximately 0.7 seconds to 0.8 seconds are required per iteration. The method allows the restriction of maximum power loss, which is important when the system is sensitive to the amount of power input. One of the problems with this method, however, is the low probability of finding a suitable solution on the first run. The optimisation often results in a local solution where the peak flux is somewhere other than the centre of the receiver or the flux

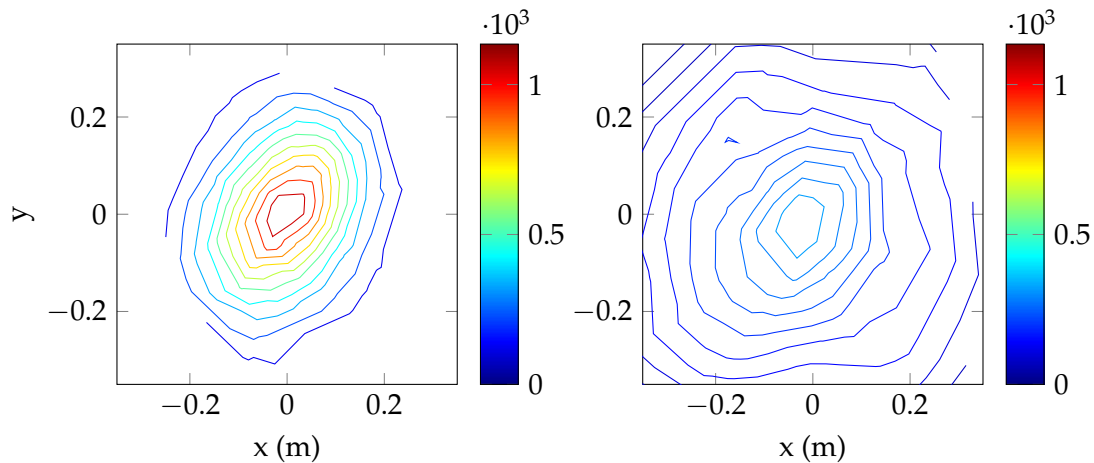


**Figure 5.11:** Contour plot of the Helio100 system on 21 December at 9h00 before (left) and after (right) Tabu optimisation

distribution is not homogenised properly. For this reason it is suggested that the method be run several times and the best solution out of the runs used.

## 5.2 Genetic algorithm

The Genetic algorithm is a non-deterministic method of optimisation designed for large search spaces (Goldberg and Holland, 1988). As for the Tabu search method, this optimisation method is based on random selection of the surveying field, but the process requires a large amount of calculations and there is no guarantee that a global optimum will be found (Arora, 2012).

### 5.2.1 Genetic algorithm method

The optimum heliostat/aim point configuration is found through several steps. First, the populations are determined as vectors containing a random aim point for each heliostat. A number of populations ( $N_p$ ) are created, each with unique heliostat/aim point combinations. Figure 5.12 shows the matrix containing the information of the populations. The number referring to a specific aim point is recorded in the matrix for each heliostat.

The fitness function at each iteration is defined as the difference between the maximum cost function and the cost function of the current heliostat/aim point configuration:

$$F_i = f_{max} - f_i \quad (5.2.1)$$

where

$$f_i = FD_{i,max} - FD_{i,min} \quad (5.2.2)$$

represents the cost function. The value of the maximum cost function is determined when all heliostats are aiming at the centre of the receiver. Since a higher fitness function results in a better design, the fitness function should be maximised. The lowest fitness function exists when all the heliostats are aimed at the centre of the

		Populations				
		1	2	...	Np-1	Np
Heliostats	1	4	6	...	2	9
	2	4	7	...	3	1
	⋮	⋮	⋮	⋮	⋮	⋮
	n-1	5	2	...	9	8
	n	9	3	...	7	1

**Figure 5.12:** An example of randomly generated populations

receiver.

A mating pool is selected from the population to produce offspring. By increasing the probability of the fitter populations to partake in the mating pool, fitter offspring can be ensured. The first step is to add the fitness function values of each population:

$$Q = \sum_{j=1}^{Np} F_j \quad (5.2.3)$$

The probability of each population is found by dividing the respective fitness functions by the sum of all the fitness functions ( $Q$ ).

$$P_j = \frac{F_j}{Q} \quad (5.2.4)$$

The candidates of the mating pool are chosen according to the determined probabilities. Offspring are produced by performing a certain number ( $I_{max}$ ) of crossovers and mutations. Probability values  $P_c$  and  $P_m$  are set to control whether a crossover or mutation will be performed. Besarati *et al.* (2014) specified the values of  $P_c$  and  $P_m$  as 0.9 and 0.2 respectively.

A random number is generated for each crossover. If the number is larger than the probability value  $P_c$ , the crossover is performed. After a random heliostat number and two populations are chosen, the respective aim points pertaining to the chosen heliostat in the different populations are swapped.

For mutation, another random number is chosen and compared with the mutation probability. If the random number is larger than  $P_m$ , the mutation is performed. A heliostat from any population is chosen at random. The aim point pertaining to this heliostat is replaced with a random aim point.

The fitness function of each of the new offspring is calculated, at which point the candidate from either the first generation of populations or the offspring with the highest fitness function is determined and recorded. A new mating pool is then selected, and the process is repeated for a fixed number of iterations or until convergence has been reached. In this way, for every new generation the best candidate will replace the previous best candidate if it has a higher fitness function.

The algorithm is summarised below:

```

Determine N_p populations
Calculate F_i using Equation 5.2.1 and P_j
using Equation 5.2.3 for each population
FOR i = 1:Number of iterations
Choose M_p populations for mating pool
Generate random number $c$
IF c > P_c
Perform crossover
END
Generate random number $m$
IF m > P_m
Perform mutation
END
Determine F_i for each of the offspring
Record best population
Determine new populations
END

```

### 5.2.2 Self-modifying algorithm

Besarati *et al.* (2014) introduce a self-modifying algorithm to the optimisation method. Optimisation methods often produce a flux distribution where the peak flux is close to the edge of the receiver. The self-modifying algorithm reduces the flux radially outward from the centre of the receiver. The method for 2D aim points requires the number of vertical and horizontal aim points to be equal.

Firstly the aim points are sorted into squares. The central aim point will form square one, with its surrounding aim points forming square two and so forth as shown in Figure 5.13. The aim point with the largest flux density in the outer most square is determined. The flux density of this aim point needs to be smaller than the minimum flux density of the aim points in the inner square for the desired radial flux distribution. If the maximum flux on the outer square is larger than the minimum flux on the inner square, a random heliostat aimed at the aim point with maximum flux will be placed onto the aim point representing the minimum flux.

The process is repeated for these two squares, until the flux on the outer square is lower than that of the inner square. When this requirement has been met, the inner square becomes the outer square and the square of aim points contained within

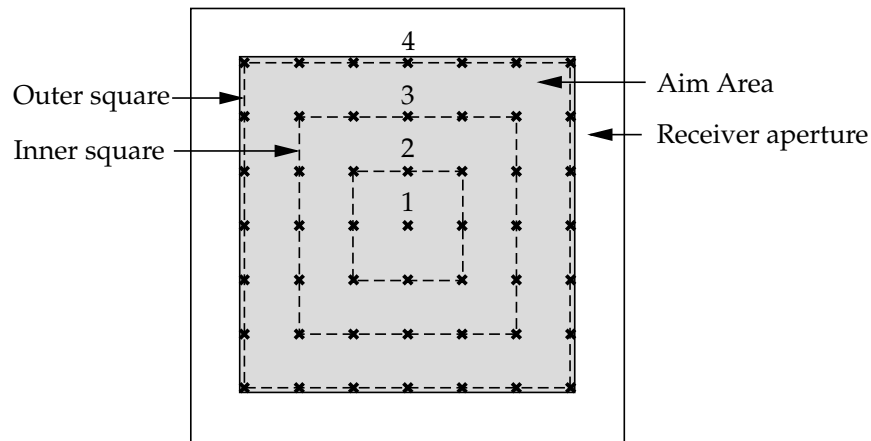


**Figure 5.13:** The receiver surface with the various aim point squares on the aim area

the new outer square becomes the inner square. The entire process is restarted for the newly determined squares.

The heliostats are paired for a vertical or horizontal aiming strategy. The outer two heliostats form the first pair and so forth. The process is implemented based on pairs instead of squares.

### 5.2.3 Results

The Genetic algorithm was implemented for the Helio40 system using the adapted HFLCAL approximation method by Collado (2010). Contrary to the TABU search method, the Genetic algorithm uses random initial guesses of the heliostat/aim point configurations.

Firstly the Helio40 heliostat field was considered at 12h00 of the 21st of December 2014. The results are shown in Figures 5.14 and 5.15. A decrease in the peak flux of 49 % was obtained, similar to the results of the Tabu method for the same inputs. The power loss of both the approximate method and ray tracer were under the set limit. A negligible deviation was present between the peak flux values of the ray tracer and the approximate method.

Thereafter, the aiming strategy was run for 9h00 as seen in Figures 5.16 and 5.17. The peak flux was decreased by 26 % and the final peak flux underestimated by 15 % by the approximate method. Although the maximum power loss was set to 25 %, the final power loss only reached 20 %. Using more iterations or a larger population group will improve the results but significantly increase the computational expense. Obtaining the current solution required twice as much computational time as the Tabu optimisation for the same system. It can be seen from both the Tabu method and the Genetic algorithm implementations at 9h00, that the Collado method is inappropriate for use at high incidence angles.

The Genetic algorithm optimisation for the Helio100 system produced similar results to the Tabu method. However, the self-modifying algorithm ensured that

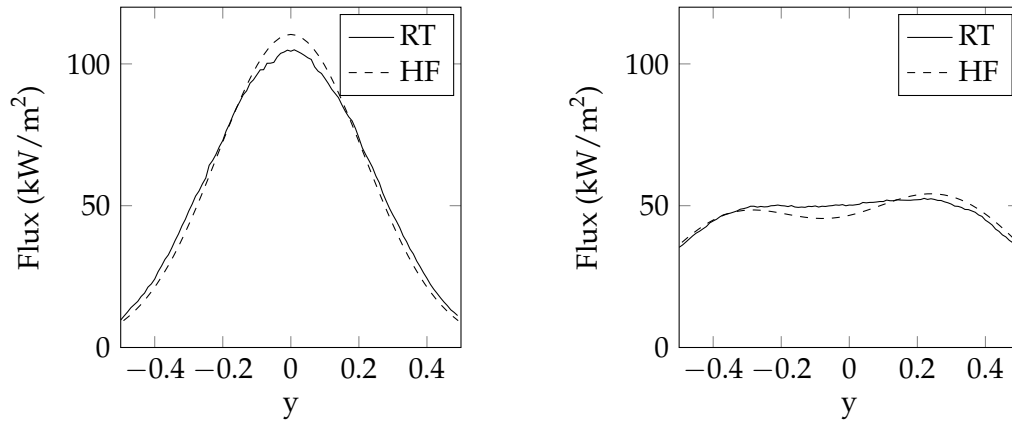


**Figure 5.14:** Flux map of the Helio40 system on 21 December at 12h00 before (left) and after (right) GA optimisation

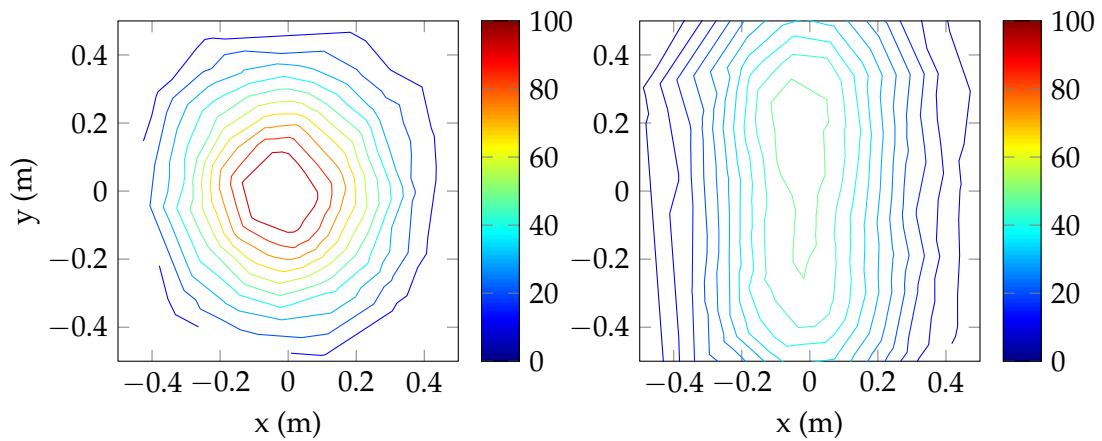


**Figure 5.15:** Contour plot of the Helio40 system on 21 December at 12h00 before (left) and after (right) GA optimisation

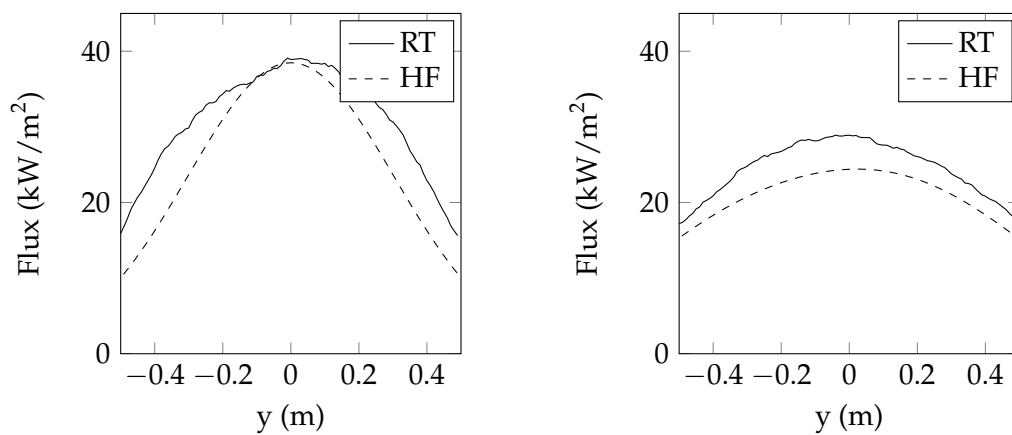


**Figure 5.16:** Flux map of the Helio40 system on 21 December at 9h00 before (left) and after (right) GA optimisation

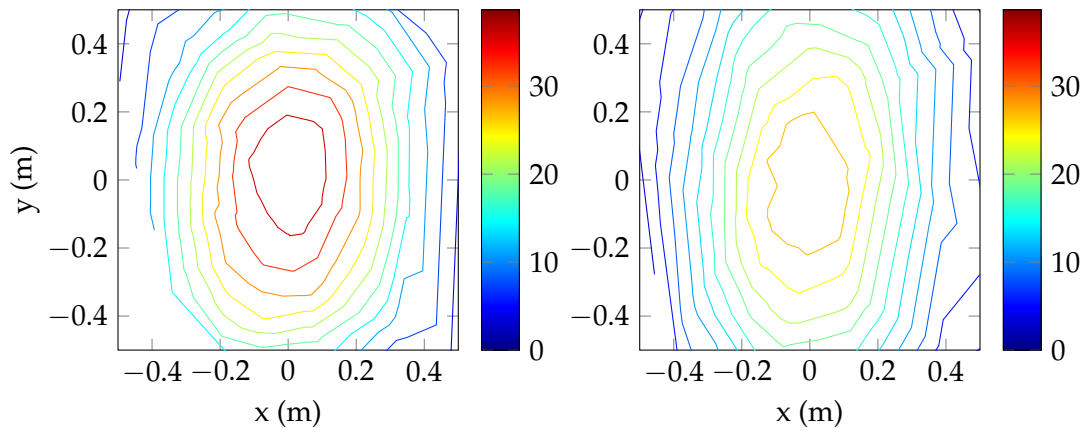


**Figure 5.17:** Contour plot of the Helio40 system on 21 December at 9h00 before (left) and after (right) GA optimisation

the flux decreased radially from the centre of the target, thereby producing an improved result. Figures 5.18 and 5.19 show the results obtained. As with the optimisation of the Helio40 flux profile at 9h00, the final power loss was much lower than the maximum specified value, indicating an incomplete optimisation process. For this heliostat system the Genetic algorithm was six times slower than the Tabu method. Similar results were obtained at 9h00 as seen in Figures 5.20 and 5.21.

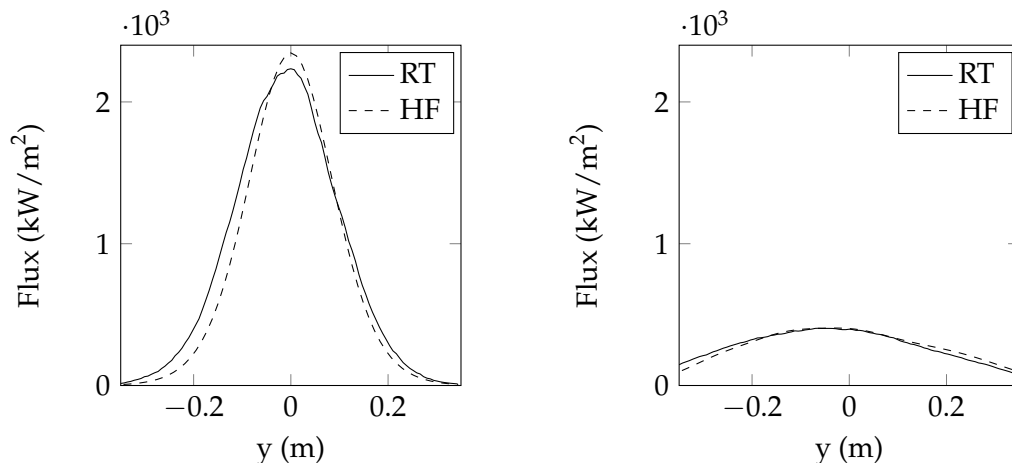


**Figure 5.18:** Flux map of the Helio100 system on 21 December at 12h00 before (left) and after (right) GA optimisation

#### 5.2.4 Analysis of the Genetic Algorithm

Through several tests it was found that the Genetic algorithm produces adequate final results if the initial guess is already close to an appropriate solution. However, due to the restrictions placed on the optimisation and the arbitrary nature of determining the initial populations, no solution is often found. To produce satisfactory results more frequently, the number of guesses needs to be increased, which would

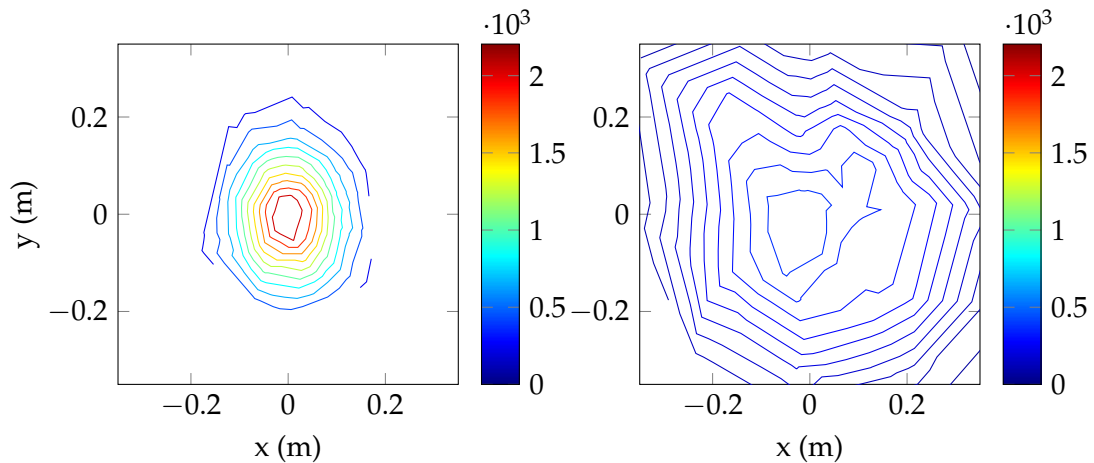


**Figure 5.19:** Contour plot of the Helio100 system on 21 December at 12h00 before (left) and after (right) GA optimisation

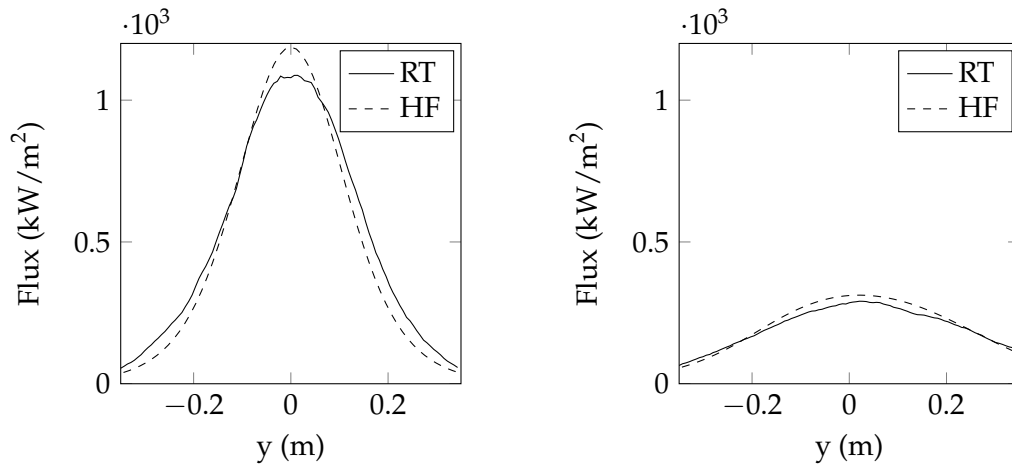


**Figure 5.20:** Flux map of the Helio100 system on 21 December at 9h00 before (left) and after (right) GA optimisation

lead to a higher computational expense. An improvement of the initial guesses is also suggested.

In cases where the maximum power loss was set too low or the aim area too large, finding appropriate random guesses became difficult. Such a circumstance significantly increases the computational expense. In the method described by Besarati *et al.* (2014), no provision is made for power loss limitations so that computational expense is not an issue. While the self-modifying algorithm improved the amount of spillage and the overall flux distribution, it also increased the peak flux.

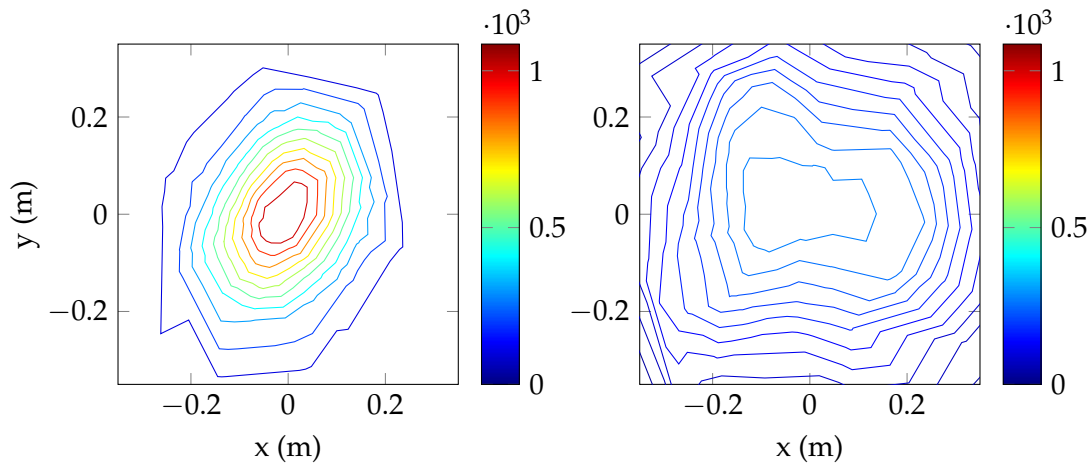


**Figure 5.21:** Contour plot of the Helio100 system on 21 December at 9h00 before (left) and after (right) GA optimisation

### 5.3 Conclusion

The Tabu search method shows promising results for aim point optimisation in both one- and two-dimensional cases. However, the use of the Collado approximation method at high incidence angles did not provide accurate results on the final homogenisation. By adding the Tabu chart, an approximate solution could be obtained faster. One major concern of this method is that it tends to fall into a local minimum at times. A way of avoiding a local minimum would be to run the optimisation several times and choose the best result.

The Genetic algorithm overcomes local optima by optimising a number of guesses and then choosing the best result. This method, however, requires more computational time than the Tabu method. When constraints are chosen such that it becomes difficult to find initial guesses within the constraints, the computational time is further extended. For the results in the published works of Besarati *et al.* (2014), the maximum power loss was not taken into account, making random guesses easily obtainable.

In the following chapter a new aiming strategy is created by merging the two methods and improving certain aspects. The flux approximation method is changed to the GMM method to improve the accuracy of the predicted flux distribution.

## Chapter 6

# Aiming strategy results

The optimisation method described in this section is a combination of the Tabu search and Genetic algorithm optimisation methods. The final aiming strategy was designed to specifically focus on the advantages of each method and to allow the optimisation methods to complement one another. Case studies were done on three different systems to point out the improvements made to the optimisation methods previously discussed.

### 6.1 Improvements on previous methods

In the previous chapter, two optimisation methods were tested and analysed. It was found that the Tabu method provided adequate results in most cases, but the strategy sometimes resulted in poor flux distributions. For the Genetic algorithm, the final results were dependent on the initial guesses of the heliostat/aim point combinations which are determined randomly. To compliment both methods, the Tabu method was put in place and run several times at low iterations to provide appropriate guesses to the Genetic algorithm. Thereafter the Genetic algorithm chooses a fraction of the newly created population in its mating pool and preforms the necessary calculations.

The cost function was improved to not only consider the minimum and maximum flux points, but all the flux densities represented by the aim points. The total objective function can thus be described in Equation 6.1.1 as the sum of the differences between the maximum flux density and the flux density represented by each aim point.

$$G = \sum_{i=1}^m (FD_{max} - FD_i) \quad (6.1.1)$$

The self-modifying algorithm was also added to this strategy to create a radial decrease in the flux distribution from the centre of the receiver. The GMM method is used as the flux approximation method in the final aiming strategy. This allowed a more accurate approximation of the flux distribution to ensure that the final predicted flux distribution closely represents the ray tracer results. This method is described in Section 3.2.4 and Appendix A.

## 6.2 Assumptions

Three case studies were done to test the functionality of the aiming strategy. The transmissivity, tracking error and specularity were not taken into account due to a lack of information. For all three cases the reflectivity of the heliostats and the receiver were kept at 0.93 and 0.07 respectively. All heliostats were considered spherical with the radius taken as twice the focal length of the heliostat. The focal length was assumed equal to the respective slant range. A pillbox sunshape was assumed for the Helio40 and Helio100 cases. Although for the PS10 case, a Gaussian sunshape with a standard distribution of 2.51 mrad was used as measured at the site of Plataforma de Solar de Almeria (Collado *et al.*, 1986).

## 6.3 Combined optimisation for case study 1: Helio40

The combined optimisation aiming strategy was first run for 12h00 on 21 December 2014. Figures 6.1 and 6.2 show that the method produced the required results. Compared to the results from the Tabu search and Genetic algorithm, the flux distribution was more evenly spread over the aim area. This also resulted in a lower final peak flux. The method was as computationally expensive as the Genetic algorithm, but did not fall into a local minimum as the Tabu method did.

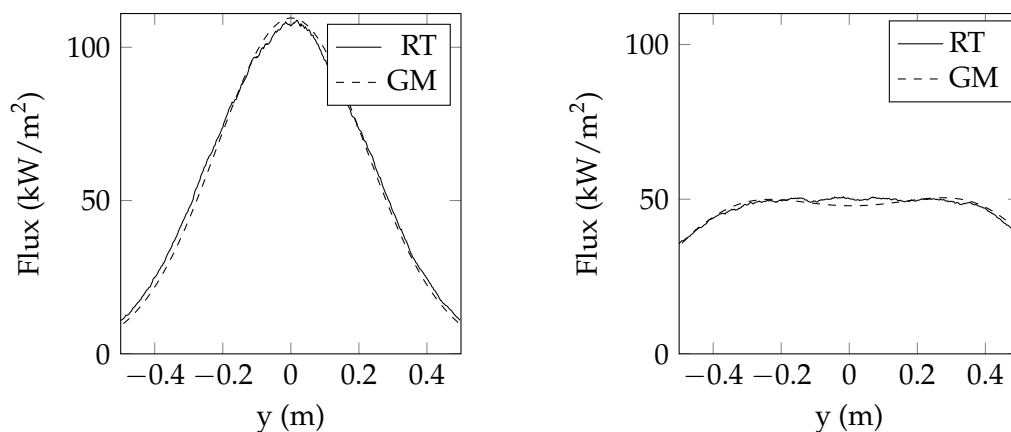


**Figure 6.1:** Flux map of the Helio40 system on 21 December at 12h00 before (left) and after (right) combined optimisation for the ray tracer (RT) and Gaussian mixture model (GM)

The flux profiles obtained by the GMM method and the ray tracer correlate better with one another than the flux profiles of the Collado method and the ray tracer. This ensures that the final result was as close to realistic as possible. An underestimation of the peak flux of 1.2 % was found in the final results.

The aiming strategy was then run for 9h00. As seen in Figures 6.3 and 6.4, the method produced similar results to that of the Tabu search and Genetic algorithm. However, the final flux profile gave a much better correlation to the results obtained from the ray tracer. Only 4 % deviation existed between the peak flux values determined for the GMM method and the ray tracer.

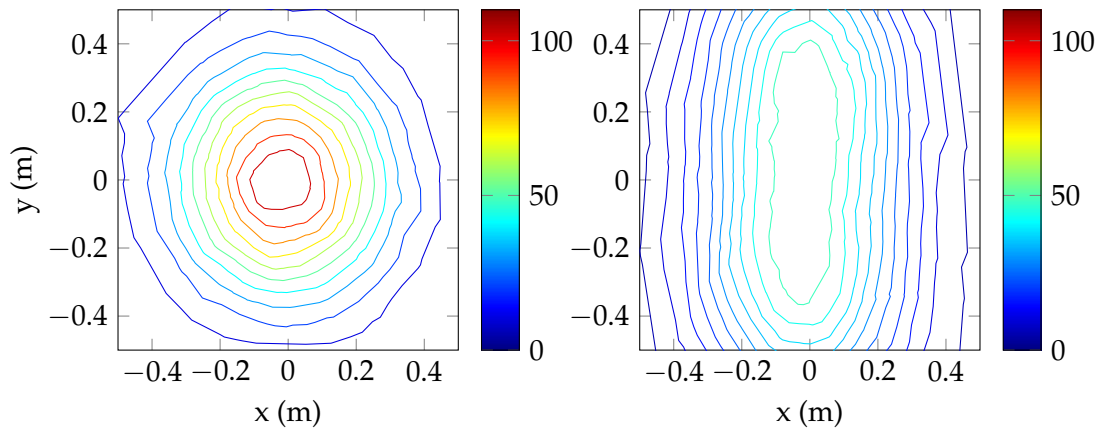


**Figure 6.2:** Contour plot of the Helio40 system on 21 December at 12h00 before (left) and after (right) combined optimisation

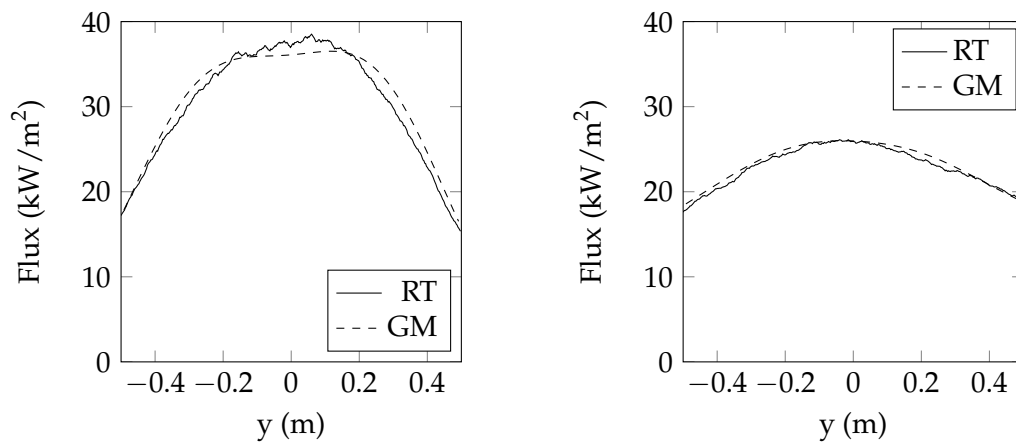


**Figure 6.3:** Flux map of the Helio40 system on 21 December at 9h00 before (left) and after (right) combined optimisation

#### 6.4 Combined optimisation for case study 2: Helio100

The combined optimisation was run for the Helio100 system at 12h00 and 9h00. The first run at 12h00 showed a decrease in the peak flux of 88 % for a maximum power loss of 15 % as shown in Figures 6.5 and 6.6. The peak flux calculated for the GMM method had a deviation of only 2.7 % from the ray traced determined value. Similar results to the Tabu method were observed, which found an improvement in the radial distribution was found. The final flux profile for the combined optimisation method was also more homogenised than the results obtained from the Genetic algorithm.

Running the optimisation method at 9h00 provided significantly better results than both the Tabu search and Genetic algorithm. As Figures 6.4 and 6.4 indicate, significant homogenisation of the flux distribution took place over 75 % of the receiver

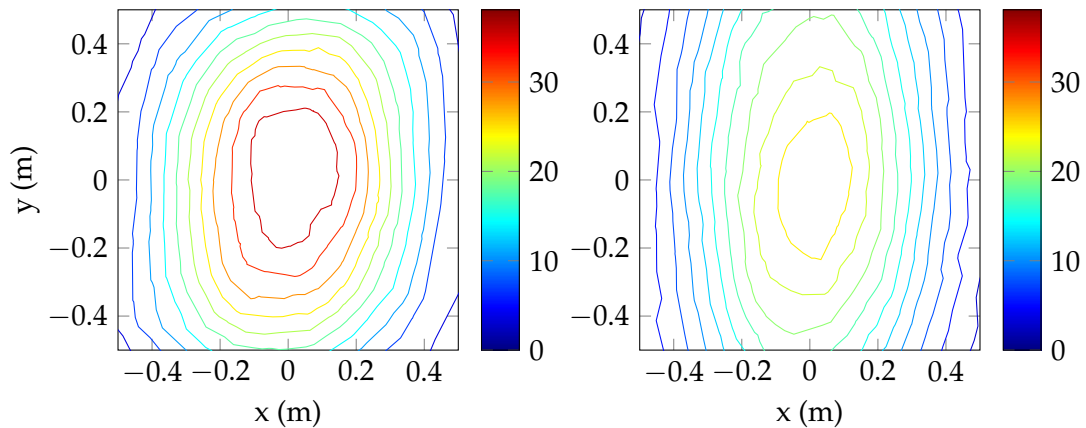


**Figure 6.4:** Contour plot of the Helio40 system on 21 December at 9h00 before (left) and after (right) combined optimisation

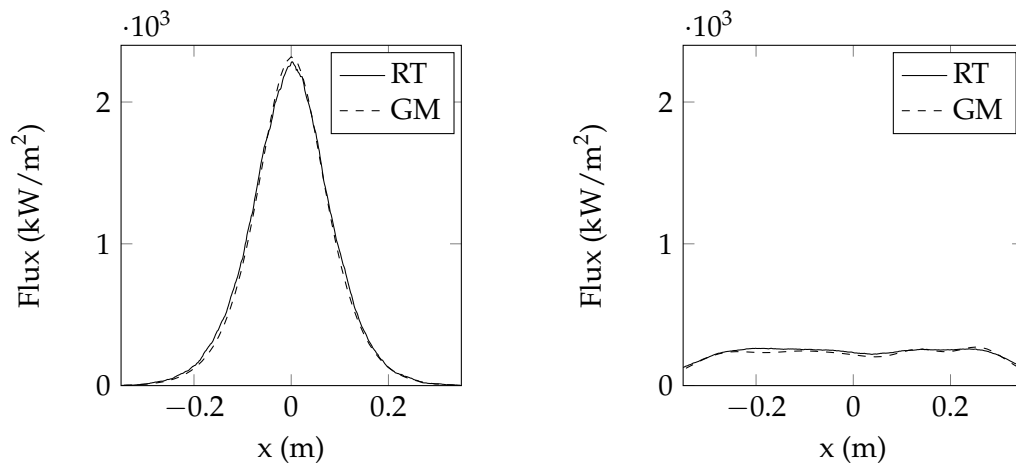


**Figure 6.5:** Flux map of the Helio100 system on 21 December at 12h00 before (left) and after combined optimisation (right)

area. The method introduced a flux loss of 79 % with a maximum power loss of 20.6 %. Contrary to the Collado method, which overestimated the peak flux by between 7 % and 15 %, the GMM method had a maximum overestimation of 3.2 % for this specific run.

## 6.5 Combined optimisation for case study 3: PS10

The heliostat field of the PS10 system is considerably larger than the experimental Helio40 and Helio100 systems. A test run of the combined aiming strategy was done to investigate how the strategy would perform on such a large system. The PS10 system consists of 624 heliostats. The GMM method of each of these heliostats had to be determined for the time the test was run i.e. 12h00 December 2014. Determining the GMM method parameters took roughly 17 hours for a single solar position. Furthermore, the combined aiming strategy took roughly 12 hours to

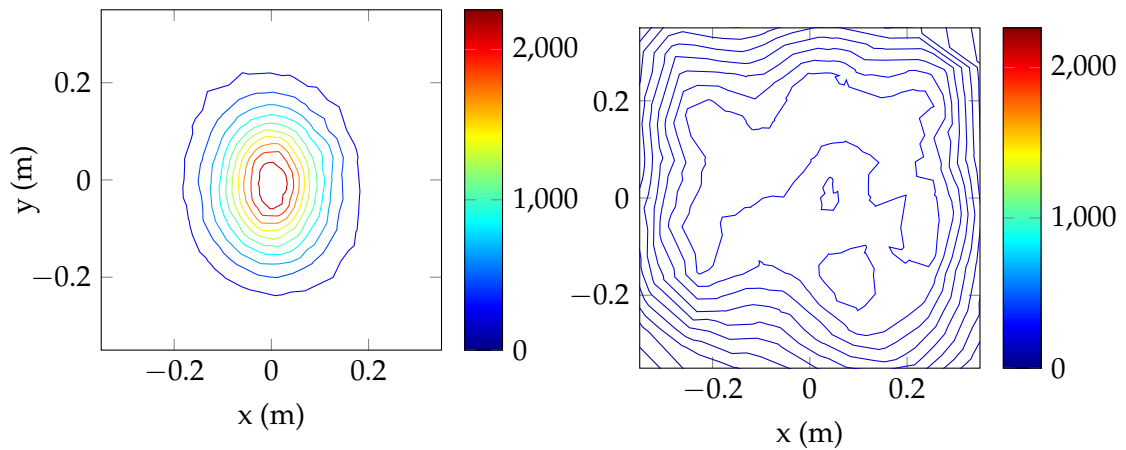


**Figure 6.6:** Contour plot of the Helio100 system on 21 December at 12h00 before (left) and after combined optimisation (right)

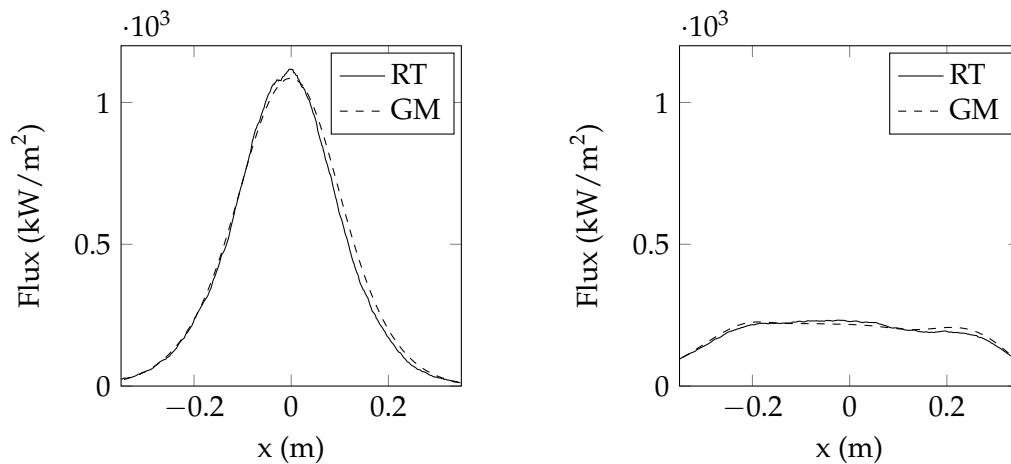


**Figure 6.7:** Flux map of the Helio100 system on 21 December at 9h00 before (left) and after (right) combined optimisation

complete. The excessive computational time can be attributed to the specifications of the computer used as a processor for the strategy.

The combined aiming strategy was run for an aim area of 75 % with a maximum power loss of 25 %. The peak flux was lowered by 91 % with a final power loss of only 21.2 %. Figures 6.5 and 6.5 show that the flux profile was homogenised over the required area. The GMM also correlated well with the ray traced profile.

Although the combined optimisation method produced the required results, the method was computationally expensive. Further studies will need to be done to determine how effective the combined method would be on a faster processor.

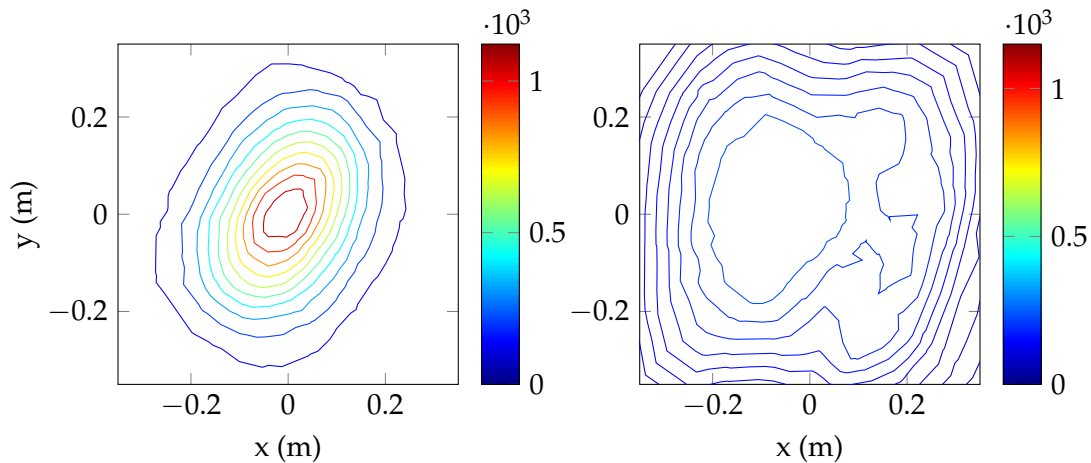


**Figure 6.8:** Contour plot of the Helio100 system on 21 December at 9h00 before (left) and after (right) combined optimisation

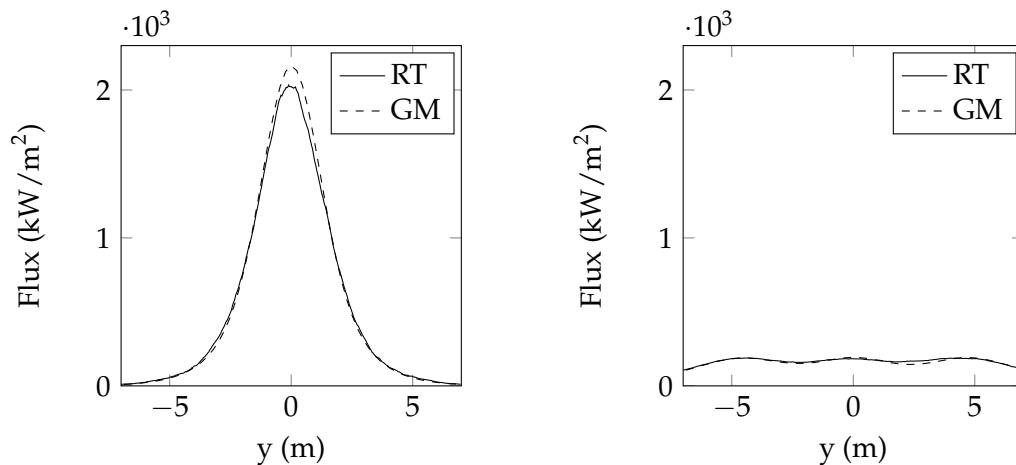


**Figure 6.9:** Flux map of the PS10 system on 21 December at 12h00 before (left) and after (right) combined optimisation

## 6.6 Conclusion

The results obtained from the combined method show significant improvement to either the Tabu search or Genetic algorithm on their own. Local minima were avoided by introducing the Tabu search method to determine the initial guesses. The combination of the different advantages of the original optimisation methods created an aiming strategy that was more robust and requires the same computational expense as the Genetic algorithm. In addition to the advantages of the optimisation method, the use of the GMM method provided more realistic and trustworthy results than the circular Gaussian flux approximation methods. To understand how the static aiming strategy would behave in a realistic environment, the strategy was implemented on an experimental heliostat field. The following chapter describes the experimental setup and the experimentation results.

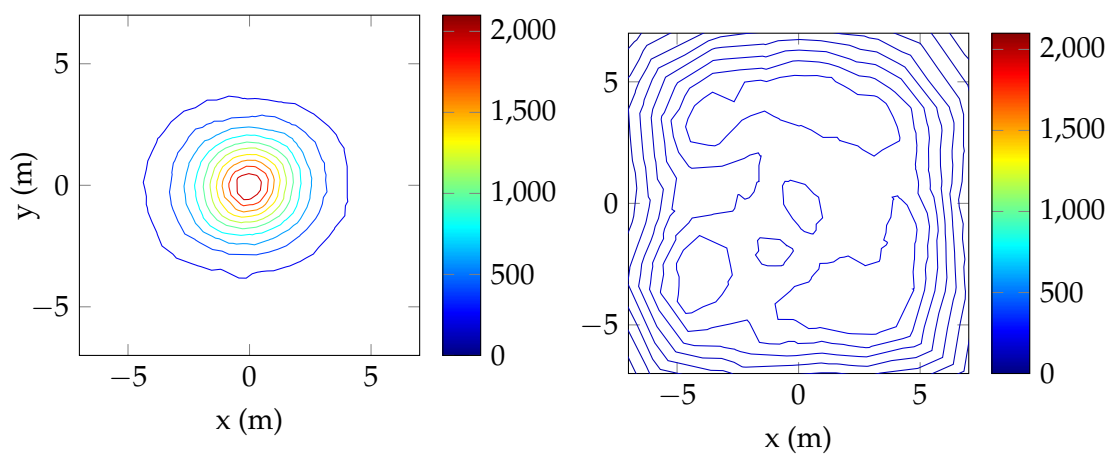


**Figure 6.10:** Contour plot of the PS10 system on 21 December at 12h00 before (left) and after (right) combined optimisation

## Chapter 7

# Experimentation

Thus far only theoretical analyses of the aiming strategy have been done. To get an idea of the deviations that could exist in practice, experimental results for the aiming strategy need to be obtained. The experimentation was also used to validate the method of using a photo of a reflected image and a flux sensor to approximate the experimental flux distribution values. A method of obtaining the parameters for the GMM method using a photograph was introduced as well.

### 7.1 Experimental setup

The main goal of the experimental setup was to measure the flux distribution across the receiver. For this setup two flux sensors, a Lambertian target and an SLR camera were used as shown in Figure 7.1. Table 7.1 details the instrumentation used in this setup. The Helio40 system was used for both the single heliostat and optimised aim point experiments. The heliostat surfaces in this system were not ideal, so the images obtained were irregular. An example of these warped surfaces is shown in Figure 7.2.

**Table 7.1:** List of experimental instrumentation

Target	1 m x 1 m
Flux sensor 1	VatellCorp TG 1000-0 with AMP-15 amplifier S/N: 9627
Flux sensor 2	HukseFlux SBG01 S/N: 1596
Data acquisition unit	National Instruments C-DAQ 9181 S/N: 16615BD
SLR Camera	Nikon D5100 S/N: 50902398
Lens	70-200 mm Nikon S/N: 3678032
Neutral density filter	Kenko Pro1D 8(W) 52 mm

A Lambertian target positioned 3.3 m above the floor with an area of 1 m<sup>2</sup> was used in the tests of single heliostats. To obtain more than one consistent measurement of flux, two sensors were used. One sensor was placed in the centre of the target; the other was placed one sixth of the target width to the right of the centre. Photos were taken of reflective light on the target using a neutral density filter.

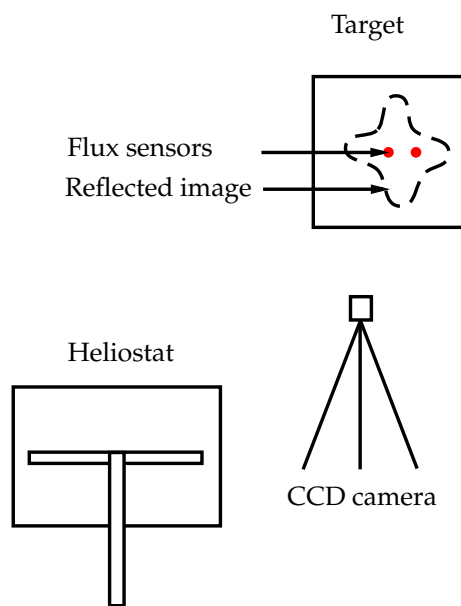


**Figure 7.1:** Experimental setup



**Figure 7.2:** A Helio40 heliostat showing warping of the reflected image

Each image was calibrated such that the correct amount of light enters the camera to avoid saturation. The data acquisition unit recorded the flux of both sensors at the time of experimentation. The DNI was also recorded for scaling purposes of the image.

The image was processed by cropping and squaring the target using Matlab image processing software. The colour of the image was converted to gray scale to ascribe an intensity value to each pixel relative to the brightness of the pixel. The intensity values were scaled according to the measured flux values to produce a flux density distribution.

The following section describes the experiments that were conducted. The first experiment compared the flux measurements to the converted photographic image to determine the relationship between the light intensity and the flux distribution. The second experiment demonstrated the method of determining the parameters of an analytical GMM through a captured image. The third experiment investigated the implementation of an aiming strategy on an experimental system.

## 7.2 Experimental flux distribution models

In the previous chapters, the approximate methods were compared with the ray tracer. The ray tracer was assumed to be validated and close to accurate. It was, however, necessary to determine how the proposed aiming strategy would perform in an experimental environment. The next set of experiments were conducted to validate the method used to obtain a suitable flux distribution through photography and to determine the factors influencing aiming strategies, which are not taken into account by theoretical modelling.

### 7.2.1 Correlation of image intensities and flux measurements

An experiment was required to verify that the flux distribution obtained from image processing correlated with the measured flux distributions from the flux sensor. In other words, it needs to be determined whether the flux distribution linearly correlated with the intensity of the image pixels.

This experiment used a single heliostat initially positioned at the centre of the target. Figure 7.3 is a photo taken of the reflected image, which was processed using the method described above. The heliostat was allowed to drift while flux measurements were taken every second. The processed image values were scaled such that the maximum and minimum pixel values represented the maximum and minimum measured values respectively. Thereafter the measured values were plotted against the values obtained from the image processing as shown in Figure 7.4.

A good correlation was found between the measured and approximated flux values although deviations were present in some areas of the plot. The deviations could be attributed to a non-Lambertian surface or the fact that the flux sensor has a measurement accuracy of  $\pm 3\%$ . The results obtained from this experiment showed an

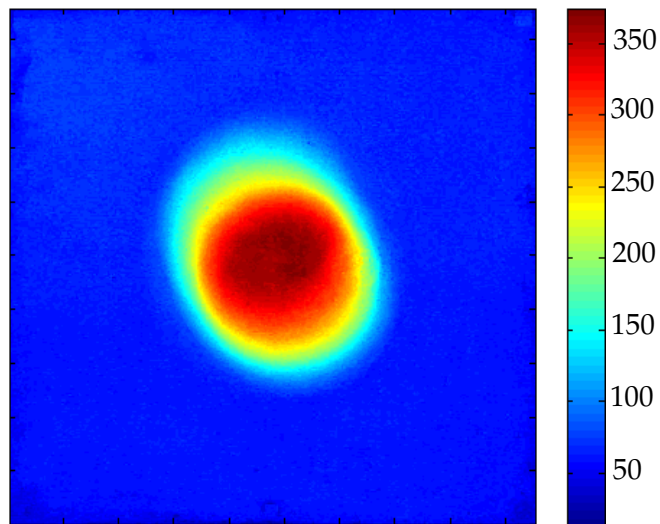


Figure 7.3: Flux image of a single heliostat created by image processing

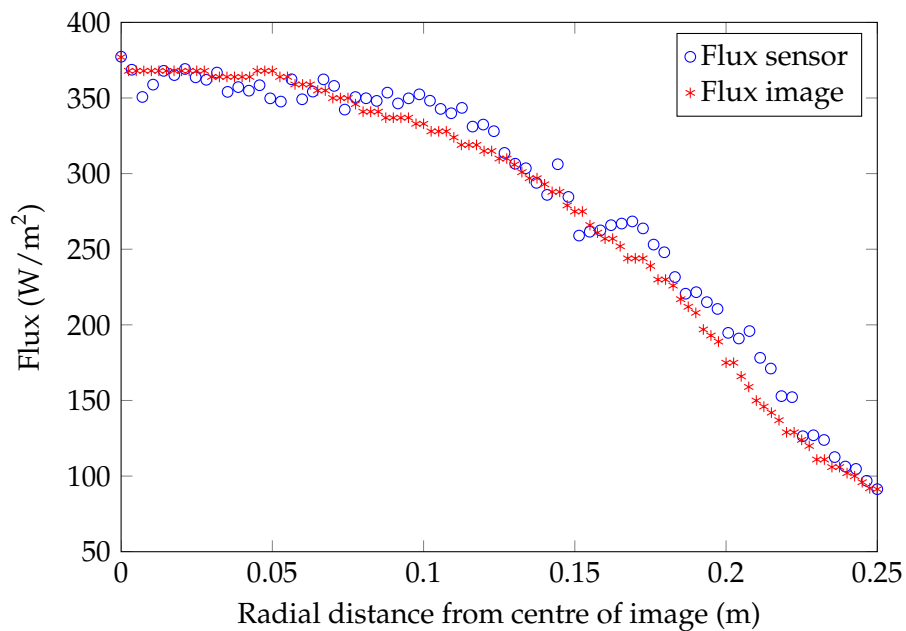


Figure 7.4: Comparison of measured flux from flux sensor and interpolated flux from image processing

appropriate correlation between the measured and approximated values. As a result, the flux distribution was assumed to be linearly related to the intensities of the pixel values of the photographed image.

### 7.2.2 Fitting of the GMM to reflected image

This experiment introduces the method of characterising a heliostat facet using a photo of a reflective image and a flux sensor. The outcome of this experiment determined the GMM parameters of a heliostat at a certain incidence angle and compared the GMM method results with the HFLCAL approximation method.

A photo was taken of the reflective image of the front heliostat of Helio40. The heliostat was purposefully bent to create an imperfect reflective image. In other words, the image was made to approximate a circular Gaussian distribution. To determine the parameters needed for the analytical GMM function, the density at each point of the target was required. The flux distribution of the image is approximately linear to the intensities of the pixels. The image on the left of Figure 7.5 shows the processed reflective image scaled according to the measured flux.

To find the GMM which fits the reflective image, the intensity values of each pixel were used. Using the Akaike Information Criterion (AIC), the appropriate amount of bivariate Gaussians required for the GMM method was determined (The Mathworks Inc., 2014). For this image, 7 bivariate Gaussians were used. The image on the right of Figure 7.5 shows the final GMM determined for the experimental image.

The results show that the determined GMM was closely related to the measured

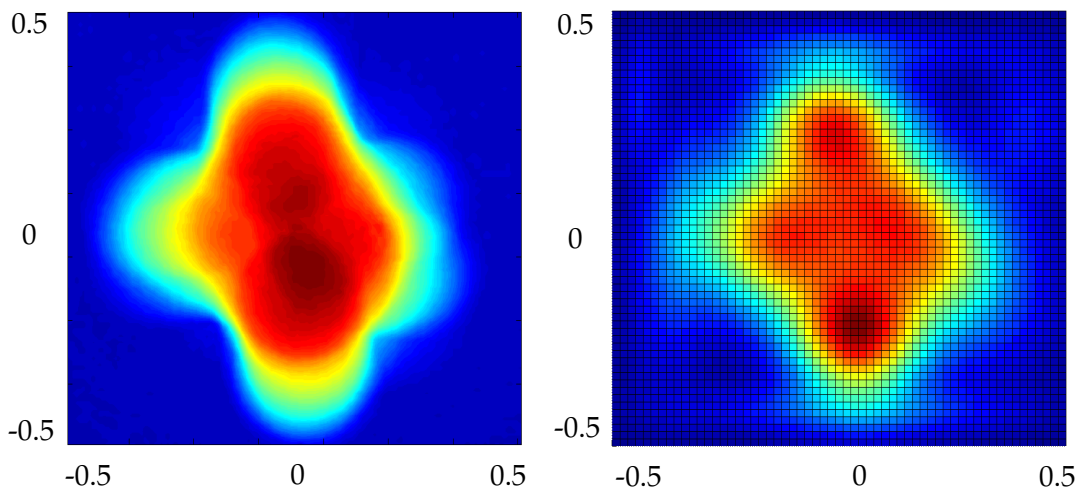


**Figure 7.5:** Processed flux image (left) and GMM determined for the experimental image (right)

flux distribution. It should be noted that the GMM fitting process is stochastic in nature, thereby producing some deviations from the actual results.

### 7.2.3 Optimised aim point results

To test how the aiming strategy would perform in reality, the proposed aiming strategy was implemented on the Helio40 system. A test of the full mirrors was

impossible because of several limitations. Because safety was a concern, a large area of the heliostats had to be covered up to avoid excessive reflections on nearby buildings. A reflective area with a diameter of 30 cm was used for each heliostat. The system was also incomplete at the time of testing, so only 9 heliostats were available. For this test, a Lambertian target 13 m above the ground was used with an area of  $2 \text{ m}^2 \times 2 \text{ m}^2$  with no flux measurement devices. Therefore only the ratio of intensity values relating to the flux were considered. However, an infrared camera was used to provide temperature measurements.

Five vertical aim points were used over 75 % of the height of the target. Figure 7.6 shows the processed flux distribution images before and after the aiming strategy was implemented. Both the peak flux and flux gradients were shown to be reduced after the aiming strategy. Poorly calibrated tracking systems and wind loads had an effect on the heliostat images and are discussed in the next chapter. Figure 7.7

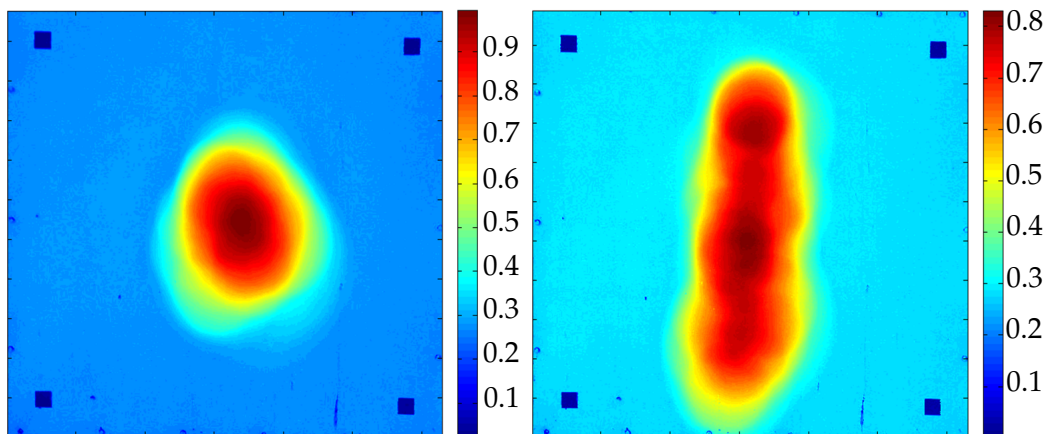


**Figure 7.6:** Flux distribution of aiming strategy before (left) and after (right) the aiming strategy was implemented

shows the infrared measurements at the time of experimentation. The image at the top left shows all the heliostats aimed at the centre of the target. The maximum temperature is measured as  $24.9 \text{ }^\circ\text{C}$ . The image at the top right shows the target with the aiming strategy implemented. The area where the flux is homogenised and the temperature now evenly distributed at approximately  $23 \text{ }^\circ\text{C}$ . The bottom left image shows the temperature measurement after the heliostats were allowed to drift for three minutes. Within this amount of time there was no significant decrease in the temperature. After another three minutes with no heliostats aimed at the target, the temperature dropped by  $2 \text{ }^\circ\text{C}$  as seen in the bottom right image.

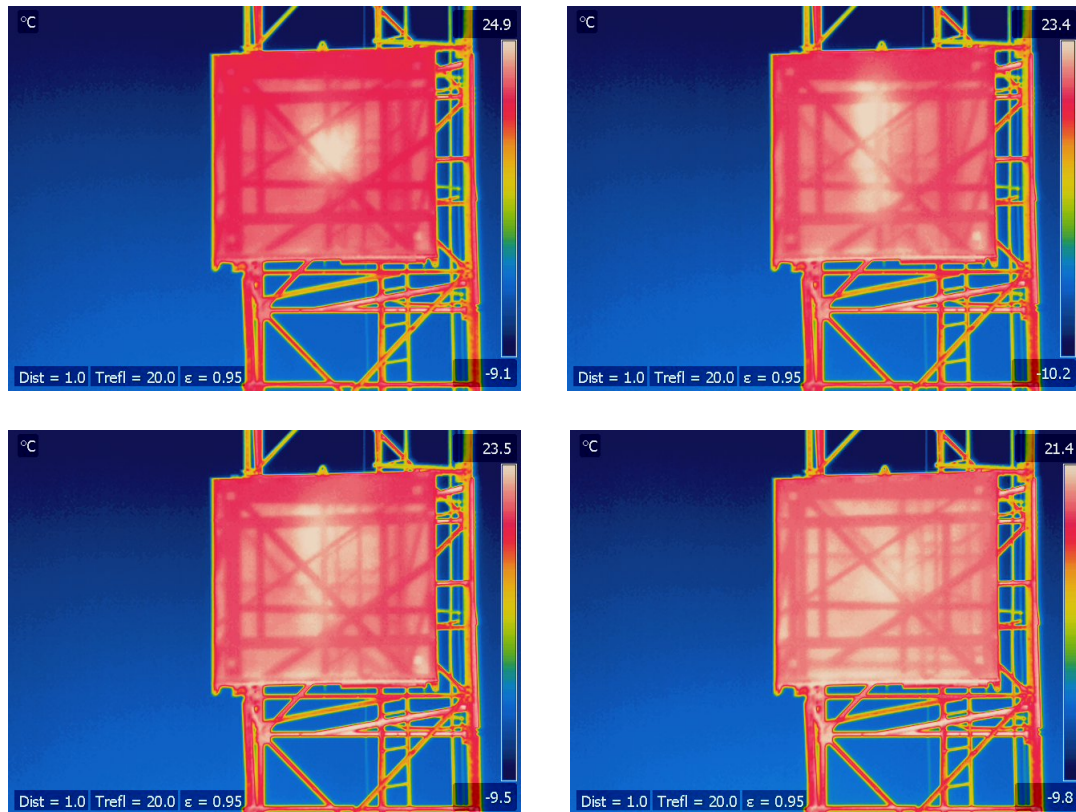


**Figure 7.7:** Thermal measurements for central aiming (top left), 5 point aiming strategy (top right), after three minutes (bottom left) and after six minutes (bottom right)

### 7.3 Conclusion

The purpose of the final experiment was to investigate aiming strategies on actual heliostat systems and the factors influencing these strategies. It was found that flux distributions could be experimentally determined using image processing and a single flux sensor. This method can also be used to determine the GMM for an experimental heliostat. The implementation of the aiming strategy on an experimental system produced appropriate results with some deviations.

The factors that influenced the aiming strategy theoretically and experimentally are described in the next chapter.

## Chapter 8

# Analysis and discussion

From the theoretical and experimental research conducted, trends, influences and problems relating to aiming strategies were observed. The purpose of this chapter is to analyse and discuss these findings.

### 8.1 Factors affecting static aiming strategies

Factors such as the number of aim points, heliostats and iterations, as well as the size of the receiver influence the outcome of the optimisation. The following section discusses the findings regarding these factors.

#### 8.1.1 Number of aim points and iterations

There exists a relationship between the number of aim points and iterations; a higher number of aim points will require a higher number of iterations for the strategy to converge to an appropriate solution. However, at some point increasing the number of aim points and iterations will not produce a significant improvement to the results. In such cases it is necessary to determine an ideal balance between the number of these variables and the computational time available.

For small heliostat fields of between 10 and 100 heliostats it was determined through experience that a suitable amount of aim points is less than 50 % of the total amount of heliostats. For example, for the Helio100 system with 60 heliostats, less than 30 aim points are satisfactory. Having more aim points will introduce unnecessary complexity and increase the computational expense without producing better results.

#### 8.1.2 Number of heliostats and receiver size

The proposed aiming strategy was developed as the first of its kind in STERG. As such it has not yet been developed to the point of being 'smart' enough to detect when the aiming strategy will produce a very uneven flux distribution, but it does not lower the flux gradient enough or cause too much spillage. In the case, where poor results are obtained, the following manual adjustments could be made:

- When a small amount of heliostats are aimed at the target, an uneven flux distribution could be found if the aim area is too large. In this case it is necessary for the user to either lower the aim area (as illustrated in Figure 3.7) or reduce the size of the receiver.
- If after optimisation the flux gradient is still too high, the maximum specified power loss should be increased to allow better homogenisation.
- Spillage could be reduced by either reducing the aim area or by reducing the specified maximum power loss limit.

If a maximum power loss is specified, the appropriate aim area can be determined through an iterative process. First the aiming strategy is run for an aim area of 90 % at an unconstrained spillage. The power loss after optimisation is then determined. If the power loss is higher than the maximum specified power loss, the aim area is decreased. This process is repeated until the calculated power loss is within an appropriate error margin of the specified maximum power loss.

Some systems require homogenisation over a specific area of the receiver. In such cases the spillage could be increased until the required homogenisation is obtained.

## 8.2 Factors affecting dynamic aiming strategies

Although the static optimisation of a flux distribution is a once off execution, the reality is that a number of factors can affect the aiming strategy during dynamic aiming. These factors include image drift, direct normal irradiation and reflectivity, tracking errors and wind loads, off-line heliostats and cloud cover. Although the scope of this project does not include these factors, it is still important to discuss their effects.

### 8.2.1 Image drift

Image drift occurs when the heliostats are in a stationary aiming position while the sun is still in motion. The motion of the reflective images is relative to the motion of the sun. This effect is illustrated in Figure 8.1.

Since the parasitic power used by the drives should be minimised, in theory it would be ideal to allow the heliostats to drift such that the drives are used as little as possible. Such a scenario is not a feasible option though with the vertical aiming of a section of a cylindrical receiver as represented by the Helio40 system, because the reflective image would not be reflected perpendicularly onto the surface of the receiver. Hence, for vertical aiming it is suggested that the drives frequently adjust the heliostats according to the system.

For 2D aiming on a flat surface, allowing the heliostats to drift may be plausible. As the composite image drifts towards the edge of the surface, the heliostats closest to the edge of the surface could be repositioned to aim at the area on the surface which no longer has heliostats aiming at it. This method would, however, compromise the flux distribution on the receiver. An algorithm adjusting the heliostats

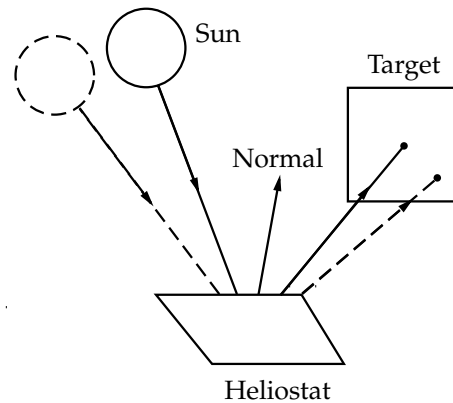


**Figure 8.1:** An illustration of drift affecting the position of the aimpoint on the target for a stationary heliostat

such that the flux stays homogenised while lowering the use of parasitic power is required. This method is beyond the scope of this thesis and is suggested for future work.

### 8.2.2 Direct normal irradiation and reflectivity

Deviation in the direct normal irradiation increases or decreases the flux density and power of the reflective images of the heliostats. At a very high DNI, even when using an aiming strategy, the peak flux may still be too high. A solution is to aim some of the heliostats at stand-by positions away from the receiver aperture for the duration of the high DNI or a new aim point optimisation could be implemented using the new DNI value.

The reflectivity of the mirrors can also have adverse effects on the flux distribution. The influence of the reflectivity of a single heliostat on the flux distribution is relative to its flux profile. The probability of the reflectivity of a single heliostat having an effect of the final flux distribution becomes more important the lower the number of heliostats in the system and the greater the influence of the flux profile of the specific heliostat on the final flux distribution.

### 8.2.3 Wind loads and tracking errors

During the experimental tests of the proposed aiming strategy, a wind speed between 8 m/s and 21 m/s was measured at the Stellenbosch Sonbesie weather station. Imperfect manufacturing of these prototype heliostats caused wind load to have an adverse effect on the experimental aiming strategy results. After the implementation of the aiming strategy some heliostats did not track correctly even though the system was manually calibrated before aiming. Tracking errors were attributable to inaccurate reference points of the tracking mechanisms, uneven heliostat foundations or delays in the micro controller (Escobar-Toledo *et al.*, 2012).

To investigate the effects of tracking errors on the flux distribution of a static he-

liostat/aim point configuration, a simulation was run introducing a Gaussian error model to each heliostat/aim point combination. Standard deviations between 1 % and 8 % of the width of the receiver were chosen for the Gaussian error distribution. A random  $x$  and  $y$  offset was determined for each heliostat according to the Gaussian probability pertaining to the specific standard deviation.

The image on the left of Figure 8.2 shows the heliostats aimed at their allocated aim points obtained from the combined aiming strategy. The actual aim points of each heliostat were found after an error was applied to the aim position of each heliostat the actual aim points of each heliostat (Figure 8.2, right).

Fifty simulations were run for each variation of the standard deviation with a unique set of errors at every iteration. The homogenisation factor and power loss was determined for each iteration. A homogenisation factor is a unitless value which provides a measure of the quality of the aiming strategy for a single run. It is determined as the objective function with all heliostats aimed at the centre of the receiver ( $G_{max}$ ) divided by the objective function for the final heliostat/aim point configuration ( $G_j$ ).

$$H_F = \frac{G_{max}}{G_j} \quad (8.2.1)$$

where

$$G_j = \sum_{i=1}^m (FD_{max} - FD_i) \quad (8.2.2)$$

with  $i$  the aim point number. The higher the homogenisation factor, the better the flux homogenisation for the specific aim point configuration. The aim point configuration was determined with no errors. A power loss of 18.7 % and a homogenisation factor of 38.5 was obtained for the ideal strategy results. The homogenisation factors and power loss for the iterations considering the tracking errors are illustrated in Figures 8.3 and 8.4 respectively.

The homogenisation factors for the 1 % and 2 % cases were close to the ideal case, and for some iterations the homogenisation factor was improved. On the other hand, large deviations were encountered for the cases of 3% and above. Similarly the power loss stayed below the maximum limit for most of the 1 % to 3 % cases. For larger standard deviations the power loss will become excessively high.

As indicated by Figures 8.3 and 8.4, tracking errors play a significant role when it comes to the sensitivity of the system. These findings throw into question the relationship between the heliostat tracking errors and receiver efficiency. From the results it can be seen that a low cost heliostat might introduce large deviations from the ideal flux distributions, compromising the efficiency of the system. For this reason when designing a heliostat field and receiver system, the tracking mechanism costs of the heliostats should be weighed against the thermal efficiency of the receiver system.

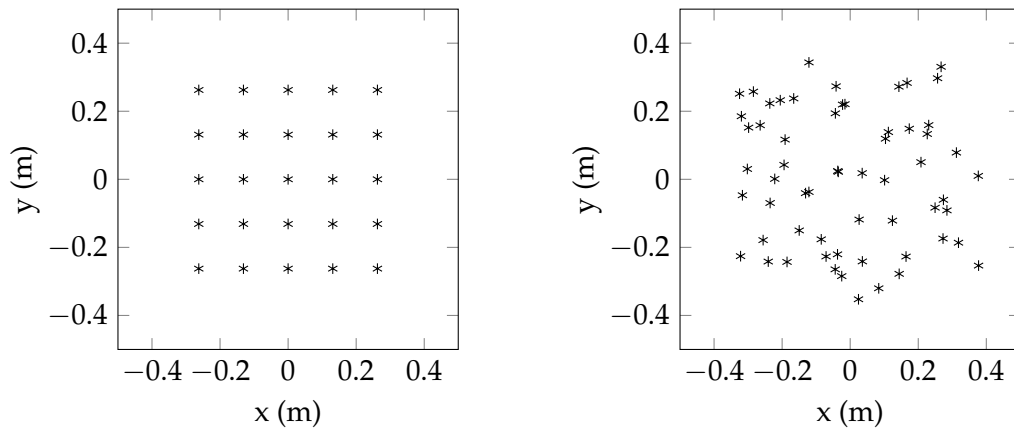


**Figure 8.2:** Aim point positions (left) and an example of the simulated aim positions of the heliostats (right)

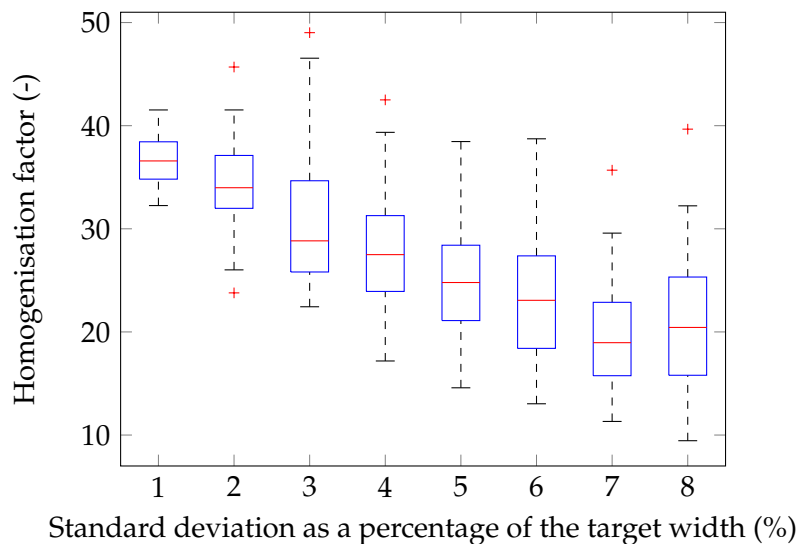


**Figure 8.3:** Statistical representation of homogenisation factors for various standard deviations of tracking errors

### 8.2.4 Cloud cover and off-line heliostats

The current aiming strategy does not consider cloud cover, although it can be implemented. If after a certain time period the affected heliostats can be determined through weather measurements, the specified heliostats can be omitted from the aiming strategy and a new heliostat/aim point configuration determined. Similarly any off-line heliostats can be omitted automatically from the aiming strategy until they become on-line. In theory these practices will work well. However, factors such as mass flow rate of the HTF, flux and spillage limitations need to be considered properly.

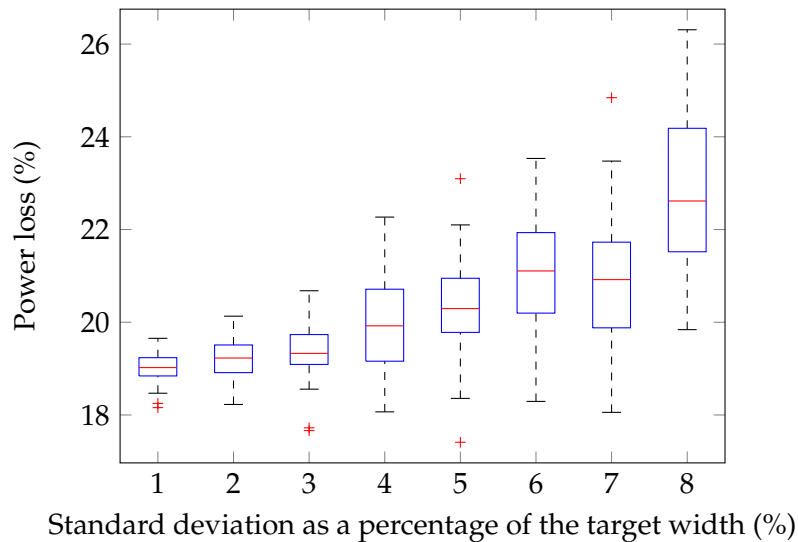


**Figure 8.4:** Statistical representation of power loss for various standard deviations of tracking errors

### 8.3 Dynamic aiming

The following section discusses some methods of continuous aiming determination of heliostat/aim point configurations over the period of operation.

#### 8.3.1 Open loop versus closed loop control

The method of dynamic aiming can operate through the use of open or closed loop control. For closed loop control, weather and temperature measurement devices can be used to provide feedback regarding the current state of the system for dynamic aiming (García-Martín *et al.*, 1999; Bobinecz, 2012). Closed loop systems offer better resources for aiming strategies because real time measurements can be used to determine the aim points of a homogenised flux profile.

#### 8.3.2 Continuous aiming of static heliostat/aim point configurations

Considering an ideal system with open loop control, the heliostat/aim point configurations need to be altered as the position of the sun changes. The time required between the adjustments of the heliostat/aim point configurations are dependent on the effects that the solar position will have on the flux distribution on the receiver. Simulations were run using the Heliol00 system to investigate the effects of using the same heliostat/aim point configuration for different solar positions.

It was concluded that static aiming of the heliostats was required only every hour of the day since little deviation occurred in the homogeneity of the flux during that time. It should be noted that the increase in DNI over time caused an increase in the magnitude of the flux. Therefore the time between each change of the heliostat/aim point configurations depends on the flux limitations set on the system.

Explicit flux limitations were not addressed in this thesis and are suggested for future work. The transition between different heliostat/aim point configurations were also not considered in this research.

## 8.4 Implementation of the proposed aiming strategy

As a final outcome a method of implementation is suggested. The steps are detailed as follows:

- Step 1: The flux profile of each heliostat for different solar positions is determined. This is either done using a coordinate measuring machine and ray tracing software or by photography and image processing.
- Step 2: The parameters of the GMM method are determined using a fitting procedure and recorded in a database for each considered solar position.
- Step 3: The static aiming strategy is then run for each solar position using the recorded parameters. The optimum heliostat/aim point configurations determined by the optimisation method is recorded.
- Step 4: During operation, the next heliostat/aim point configuration is determined.

## 8.5 Conclusion

The factors influencing aiming strategies were identified and analysed through simulation and experimentation. While generally out of scope these factors are unavoidable in experimental work. It is therefore suggested that these factors be further researched in future work.

## Chapter 9

# Conclusions

The objective of investigating and developing an aiming strategy was delivered. The following chapter summarises the findings and contributions made. Conclusions drawn from the developed aiming strategy and suggestions for future work are also included.

### 9.1 Summary of findings

The literature review revealed that few papers have been published on aiming strategies and optimisation methods of flux distributions on central receiver systems. Existing studies often do not contain detailed information regarding the strategies and the implementation thereof on the physical system.

Two papers were found considering analytical approximate methods of flux prediction. These methods introduced a computationally inexpensive method of flux distribution optimisation as opposed to ray tracing. An analysis was done to determine whether the considered analytical methods deviated from the ray traced results.

At high incidence angles and high surface slope errors, the flux images were found to be elliptical because of the position of the sun relative to the mirror surface. Circular Gaussian approximation methods are unable to accurately approximate elliptical images and cannot model imperfect mirrors. When considering small experimental systems, the heliostat images are often far from perfect, resulting in even larger deviations between the predicted flux and the real flux image.

The advantages and disadvantages of the Tabu search and Genetic algorithm optimisation methods were determined through analysis. The Tabu search method provided appropriate results in most cases, but often ended up in a local minimum. The computational speed of the method was low but was further increased by the addition of the Tabu chart. On the other hand, the simulations of the Genetic algorithm produced similar results but frequently did not produce a result due to arbitrary method by which the initial populations are determined. A local minimum was avoided by optimising a number of populations and choosing the best result. Finding an appropriate set of initial guesses was often difficult because of

the restrictions placed on the optimisation. The flux distribution was further improved by the addition of the self-modifying algorithm.

Through experimentation it was found that wind loads and tracking errors affected the final results of the implementation of the aiming strategy. Nevertheless, appropriate results were obtained in both the distribution of flux and temperature.

## 9.2 Conclusions

Aiming strategies offer a cost free improvement to central receiver systems. This study developed the first aiming strategy for STERG for implementation on the Helio40 and Helio100 systems. The versatility of the strategy hopefully allows its implementation on almost any small experimental system. The combination of the Tabu search and Genetic algorithm used in the flux optimisation process, was found to produce more robust and reliable results than the separate algorithms.

Circular Gaussian flux approximation methods produce large deviations at high incidence angles and high surface slope errors. On the other hand, the GMM method fitted the actual flux profile very well. It is suggested that the GMM method be used to improve the accuracy of the flux predictions. The method of fitting a GMM to a flux profile appears to be a novel method of predicting the flux distribution over a receiver.

The performance and quality of the homogenisation of the static aiming strategy results depends on the amount of aim points, number of iterations, area of homogenisation and maximum allowable power loss. A trade-off between these factors and computational expense is required. For the Helio40 system, a requirement of 90 % homogeneity was specified. Nine aim points were found to be the optimum number for this system with a maximum power loss of 15 % for 12h00 and 20 % for 9h00.

Although the aiming strategy produced the required results in the theoretical simulations, factors such as wind loads and tracking errors had a significant effect on the practical aiming strategy results. It was concluded that the cost of the heliostat tracking mechanisms influences the efficiency of the thermal output of the receiver. Therefore, the cost of each heliostat should be weighed against the thermal power output for the considered aiming strategy.

## 9.3 Summary of contributions

The paper titled *A review of aiming strategies for central receivers* was submitted and presented at the Southern African Solar Energy Conference in January 2014 (Grobler and Gauché, 2014). This paper reviewed published aiming strategies both experimentally and commercially.

The journal article *Limitations of assuming a circular Gaussian flux density distribution for a single heliostat image* was also written and submitted to the ASME Journal

of Solar Energy Engineering in collaboration with Willem Landman regarding the limitations of assuming a circular Gaussian flux distribution (Landman *et al.*, 2014). This paper presented high incidence angles in combination with high surface slope errors as limitations to the use of circular Gaussian distributions.

The findings of the aforementioned paper lead to the development of a novel flux prediction method based on the actual profile of the mirror. The method fits several bivariate Gaussian models over a measured flux distribution and calculates the parameters relating to the fit. The parameters are then stored and used in an analytical function for aim point optimisation. This method is especially useful in small experimental heliostat fields where large inaccuracies are present.

The developed aiming strategy provided a better understanding of flux prediction models and optimisation algorithms in STERG. It is also the first aiming strategy at the research group and will be implemented in the Helio40 and Helio100 systems.

An improved objective function was developed to consider the flux densities of all the aim points instead of only the lowest and highest flux densities as presented in some studies. For this reason, the objective function considers the distribution of the flux as opposed to the deviation of the maximum and minimum flux which often still leads to uneven distributions.

The homogenisation factor was also introduced to be able to compare performance within and between aiming strategies.

## 9.4 Suggestions for further research

Because this is the first study in the field of aiming strategies for Stellenbosch University, many topics can be addressed in the future. The following prioritised ideas for further research are suggested:

- An in depth study regarding dynamic aiming. This study should include aiming at start up, operation and shut down. It would also be useful to consider realistic flux and power limits.
- Physical modelling of the receiver with regards to heat and mass transfer.
- A study regarding the use of calibration targets to determine the flux approximation models.
- Further studies on aiming strategies for full cylindrical and cavity receivers would be of value. Such a study would also require a study on surrounding fields when full cylindrical receivers are considered.
- Factors influencing the concentration system and the entire plant such as cloud cover, wind loading and tracking mechanisms as well as the the implementation of real time measuring devices would also be of value.

- The trade-off between heliostat costs and the efficiency of the thermal output is another topic that requires more attention. Such research would contribute to central receiver systems in general.

# Appendices

## Appendix A

# Supporting mathematical functions

The simulation model used to develop the aiming strategy makes use of several mathematical functions. The Delaunay triangulation method and the Gaussian mixture model fitting are from the Matlab library. These functions as well as the vector rotation function are discussed in the following section.

### A.1 Delaunay triangulation

When modelling a system using a ray tracer, the output is a matrix describing the positions of the absorbed points on the target/receiver. These points on their own have no value unless the points in between them are found. A method called Delaunay triangulation also known as height interpolation is used to approximate these points as shown in Figure A.1. Initially the points are connected in a 2 dimen-

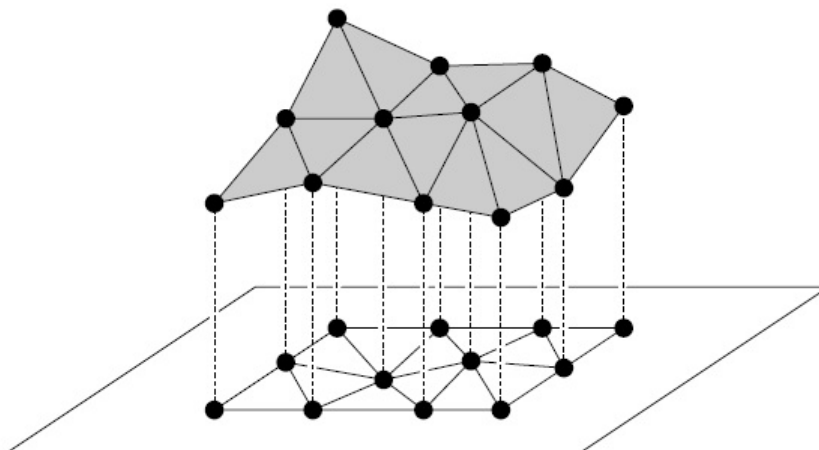
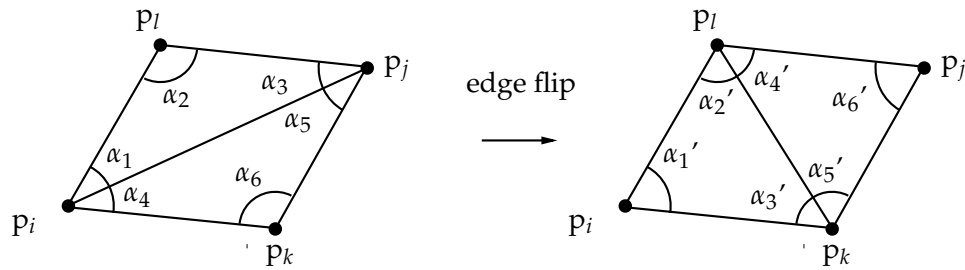


Figure A.1: Delaunay triangulation (de Berg *et al.*, 2008)

sional (2D) plane to form triangles. The points are then raised to the height of each



**Figure A.2:** Edge flip of two triangles (Adapted from de Berg *et al.*, 2008)

point respectively. The 2D space now becomes a 3 dimensional (3D) space with 3D triangles representing a polyhedral terrain. The real surface is approximated as a continuous function through the creation of discrete linear sections. The triangles are not just randomly created, however. To find the best representation of the surface, the connections that form the triangles need to be evaluated. Figure A.2 shows four points that have been connected to form two triangles in two different ways. The image on the left produces a bad representation of the real surface since points  $p_i$  and  $p_j$  are too far apart. By flipping the edge, the values of two points which are closer together are taken, which produces a better interpolated value of the surface. The function works by looking at the angles of each triangle; it searches for triangles where the smallest angle is a maximum for different connections of the points.

## A.2 Vector rotation

When modelling a heliostat field and receiver system, a 3D global coordinate system is used. A flat target plane can not be described in a 2D manner even though the plane is technically a 2D object. Since it would be very hard to describe the aim points in the 3D environment, a method needs to be implemented where 2D aim points could be transposed into 3D aim points in the 3D coordinate system.

Figure A.3 shows the process through which the aim points go to get from 2D aim points to 3D aim points. First the aim points are described in the  $x$ - $y$  plane. The normal vector for this plane points in the positive  $z$  direction. This vector is rotated to point in the positive  $x$  direction using a function called Vectorota, developed by Landman for the Matlab environment. The normal vector is then positioned to aim in the same direction as the target aim point. By adding the coordinates of the centre of the target to the coordinate of the plane we can position the plane in the correct position. All the points on the plane will now be positioned correctly in the 3D environment.

## A.3 Gaussian mixture model fitting

As described in Section 3.2.4, the Gaussian mixture model is used to determine the flux density using statistical models. In the case described in the thesis, the flux density distribution is required from thousands of data points. The data points are

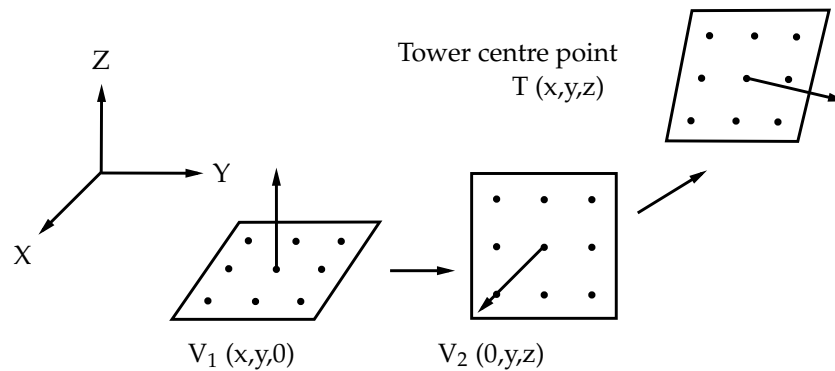


**Figure A.3:** Vector rotation of aim points

created through the ray tracing procedure described in Section 4.1 and represent packets of energy with a certain magnitude landing on the target at a certain position. These positions as well as the magnitude of each data point are important in order to further determine the flux distribution on the entire surface.

The top left figure in Figure A.3 is an arbitrary example of the data points that might exist on a target. The fitting procedure uses a Monte Carlo method in combination with the expectation maximization algorithm to find the approximate model fitting the actual data the best. The Gaussian mixture model consists of one or more bivariate Gaussian models called components. The number of components varies according to the distribution of the data. The maximum number of components is chosen manually. The larger the maximum number of components, the more complex the final function becomes, which significantly increases the computational time. The accuracy of the estimated function and the complexity of the function need to be weighed against one another. It was found that using between 4 and 6 components is sufficient for flux distribution fitting.

The first step in the fitting process is to fit a random single bivariate model to the data. The expectation maximization algorithm is used to determine the parameters that will best approximate the given data. The expectation step uses the randomly determined function to calculate the likelihood. The likelihood is defined by the probability that the estimated values are equivalent to the given data. In the maximization step, new parameters are estimated using the likelihood determined in the previous step. The expectation and maximization steps are iterated until convergence or the maximum amount of iterations are reached.

After the best approximate parameters are determined for a single bivariate function as seen in the top right of Figure A.3, the Akaike Information Criterion (AIC) is determined. This criterion produces a value representing the quality of a fit for a given dataset. The number of components for the fitting is increased and the parameters estimated. The AIC is determined for the new set of parameters. The lower the AIC value, the better the fit. The parameters which produced the lowest AIC value are then used in the modelling of the flux distribution. The bottom two

figures of Figure A.3 shows the fit for 2 (left) and 3 (right) components.

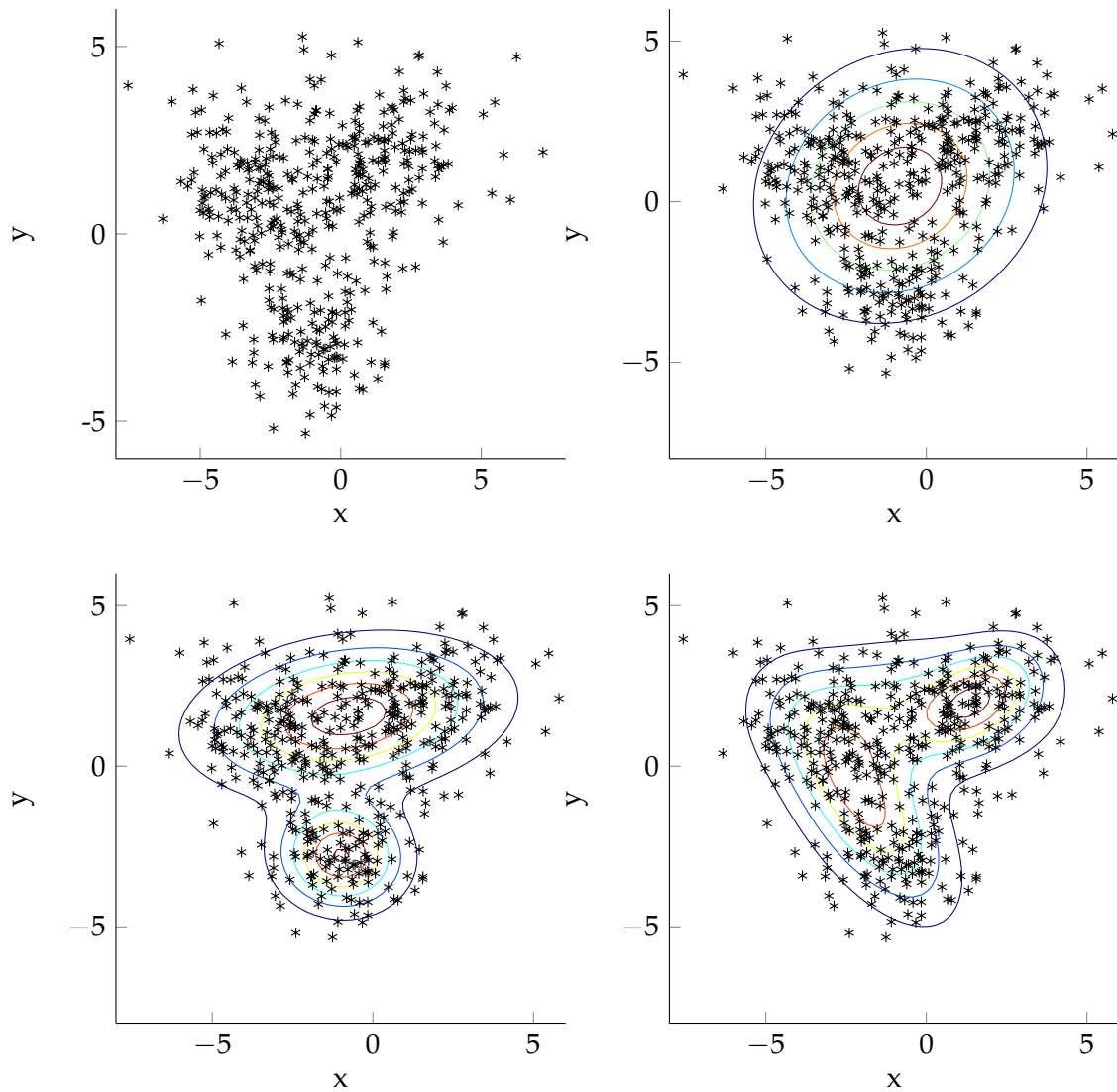


**Figure A.4:** Gaussian model fitting procedure

## Appendix B

# Factors affecting the flux profile

In Chapter 4 approximate methods were compared with one another for the variation in different factors. In this section the influences of factors such as the sunshape, surface slope error and incidence angle are looked at in more detail. Understanding the effects of certain errors on the final flux distribution results will ensure a better aiming strategy design.

### B.1 Sunshape

The incident sunshape is a representation of the radial distribution of the incoming solar rays (Buie, 2000). The apparent size of the solar disc has been measured by several researchers over the past few decades and approximates 9.3 mrad (Djafer *et al.*, 2008). Due to the large size of the light particles, the light particles are distributed to the circumsolar aureole through scattering (Buie *et al.*, 2003). An image of the solar aureole is shown in Figure B.1 with the solar disc blocked out. If one



**Figure B.1:** Photograph of the solar aureole with the solar disc blocked out (Fleet, 2013)

presumes that the solar disc contains all of the power, overestimation of the final

flux distribution could occur (Noring *et al.*, 1991). The circumsolar ratio to obtain an indication of the sunshape distribution, which is defined as

$$CSR = \frac{I_{CS}}{I_{CS} + I_d} \quad (\text{B.1.1})$$

where  $I_{CS}$  refers to the circumsolar radiation and  $I_d$  the direct radiation (Buie, 2000). A phenomenon called limb darkening is found on the solar disc due to the wavelength variation of the radial distance of the solar disc which decreases the brightness of the limb region of the sun (Raponi *et al.*, 2011).

The amount of solar flux reaching the receiver will depend on the incident sunshape, atmospheric scattering and the reflectance and area of the concentrator system (Pettit *et al.*, 1983). Several incident sunshapes are considered in the SolTrace ray tracer, such as the Gaussian, Pillbox and user defined sunshapes. The pillbox sunshape has an even intensity over a half-width of 4.65 mrad. For concentrators with a low concentration ratio this shape is sufficient. When a high concentration ratio is considered (> 10 000), more accurate sunshapes need to be used (Lovegrove and Stein, 2012).

An analysis is done to see how the sunshape affects the final flux profile results. Since the pillbox sunshape is accurate enough for many different cases, we will compare the flux profile of a pillbox sunshape with that of a Gaussian sunshape. For this test a Gaussian sunshape with a standard deviation of 2.51 mrad is assumed; this is the sunshape measured at the PS10 field in Seville Spain (Collado, 2010). Figure B.1 shows the flux profile of an ideal heliostat at a very small incident for the Gaussian sunshape (left) and the pillbox sunshape (right). It could be seen that both of these profiles take on the shape of the modelled sunshape and have different peak fluxes respectively.

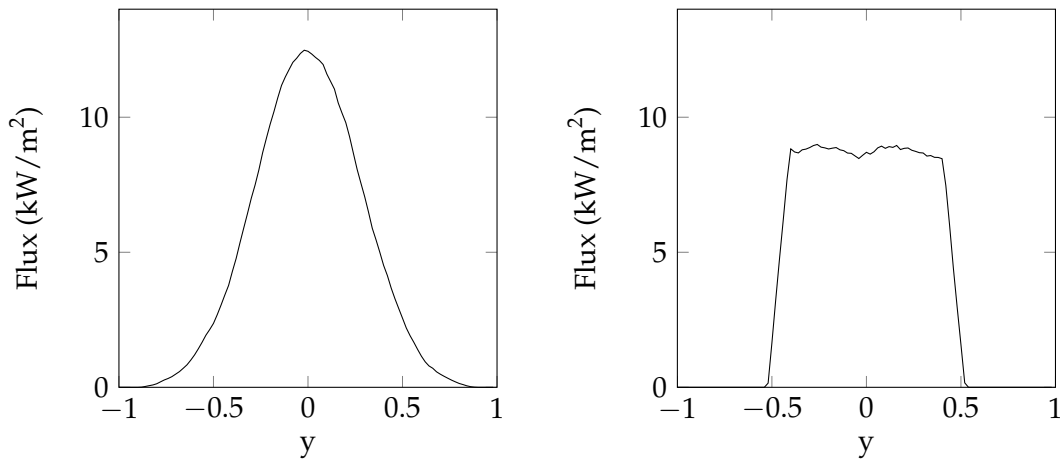


**Figure B.2:** Flux distribution of ideal heliostat with Gaussian sunshape (left) and pillbox sunshape (right)

## B.2 Surface slope error

The surface slope error is characterised as a normally distributed error. Therefore an increase in the surface slope error of the Gaussian flux profile will not cause the shape to deviate from the Gaussian shape since the sunshape was originally normally distributed. For the pillbox profile, an increase in the surface slope error transforms the shape into a normal distribution due to the domination of the surface slope error after a certain magnitude.

Figure B.2 shows that a surface slope error of 0.5 mrad is already changing the shape of the profile. At a surface slope error of 1 mrad, as in Figure B.2, the sur-

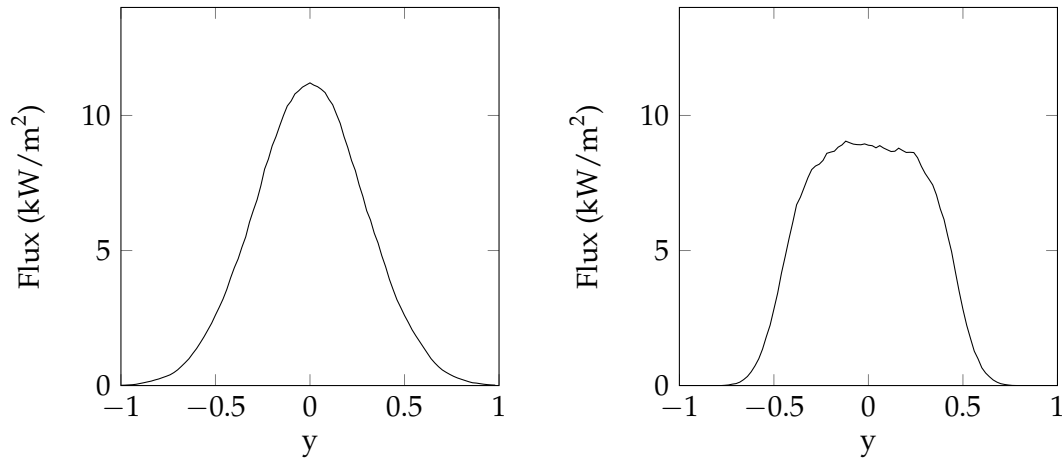


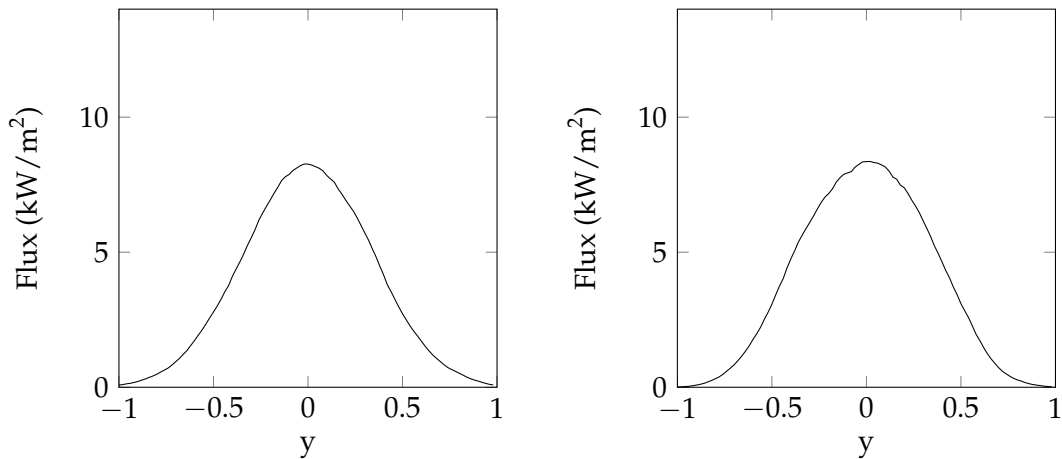
**Figure B.3:** Flux distribution of heliostat with surface slope error of 0.5 for Gaussian sunshape (left) and pillbox sunshape (right)

face slope error dominates enough for the flux profiles of both sunshapes to have approximately the same shape. Further increase of the surface slope error will only reduce the magnitude of the flux and increase the standard deviation but will not change the shape of the profile.

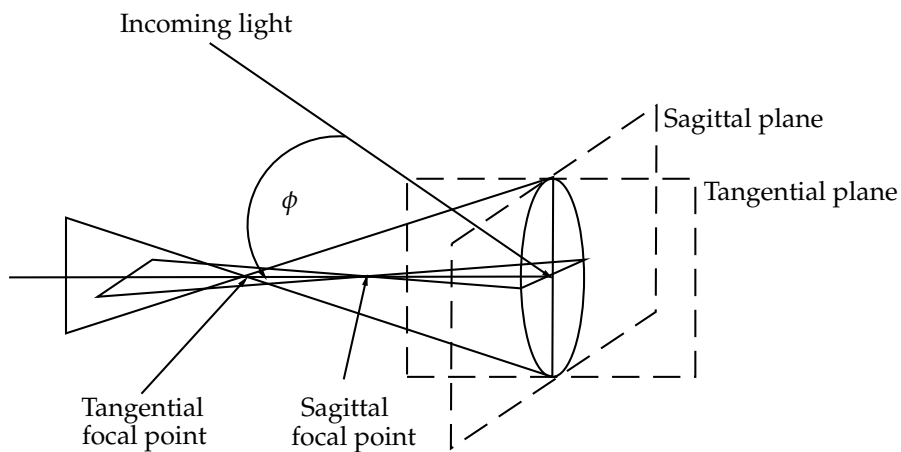
## B.3 Incidence angle

Increasing the incidence angle causes the flux to lower and the standard deviation to increase as shown in Figure B.3. This is attributed to the optical aberration of astigmatism (Igel and Hughes). When the angle of incidence is small the image is very well focussed since the focal points of the tangential and sagittal planes are close together. As seen in Figure B.5, when the incidence angle is increased, the focal length of the tangential plane becomes larger with the focal length in the sagittal plane becoming smaller. In other words, the two planes are no longer focussing close to one another causing a deformation of the image.

It is, therefore, expected that as the angle of incidence increases, the standard deviation of the profile will also increase. This is not the case for images with large incidence angles and surface slope errors. Figure B.3 shows that the image has a



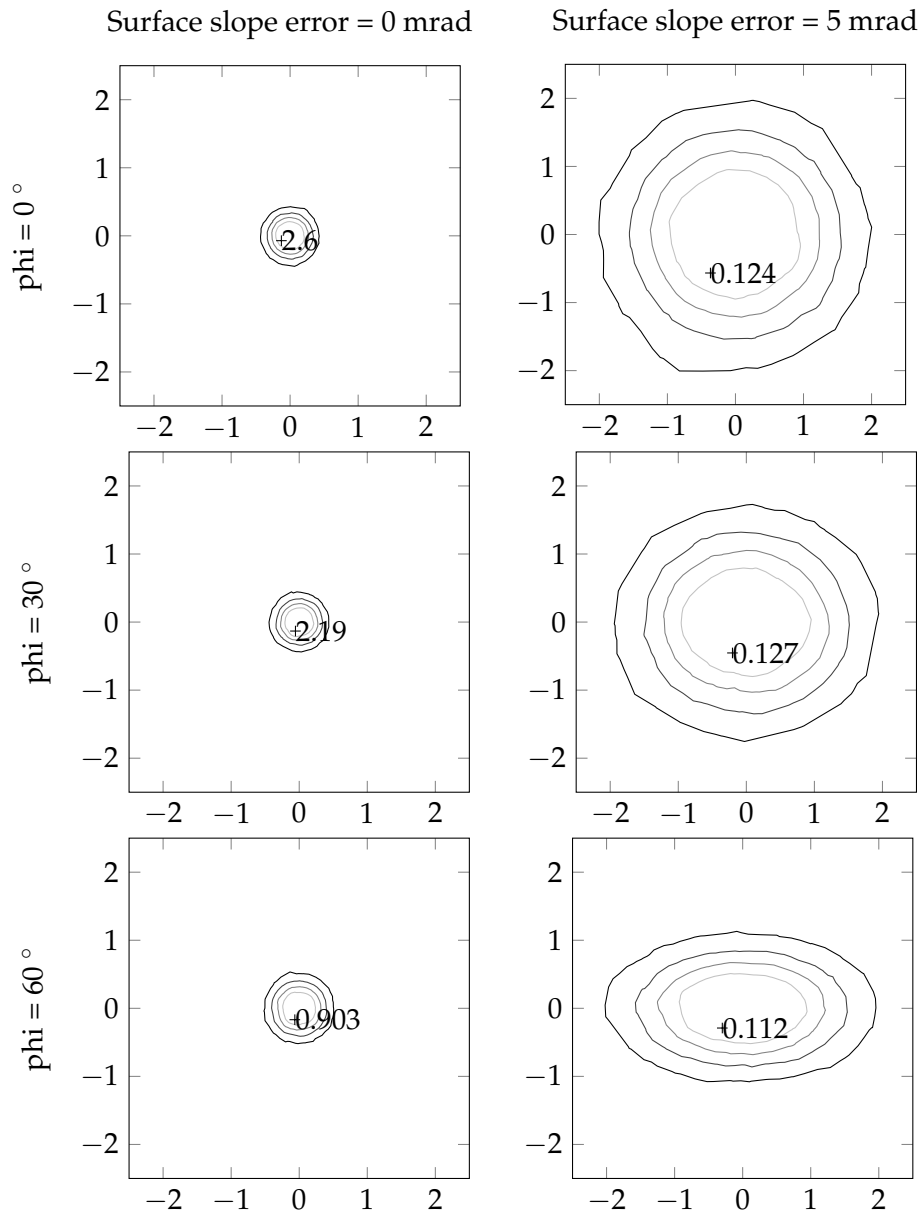
**Figure B.4:** Flux distribution of heliostat with surface slope error of 1 for Gaussian sunshape (left) and pillbox sunshape (right)



**Figure B.5:** Illustration of optical aberration of astigmatism

reduction in the standard deviation in a single plane. This phenomenon cannot be attributed to aberration of astigmatism, but rather to the bidirectional reflectance distribution function mainly caused by the surface slope error. For a mirror with a surface slope error cone of  $\sigma_{SSE}$ , the half width of the reflected error cone is twice that of the original size according to Snell's Law (Wendelin *et al.*, 2013).

From Figure B.7 it is seen that for low incidence angles the reflected image at a slant range of  $d$  has the same dimensions in both the sagittal and tangential planes. As the incidence angle increases, the vertical distance between the horizontal plane and the sun ( $d \cos \phi$ ) becomes smaller. Although this does not have an effect on the image dimension in the tangential plane, the dimensions in the sagittal plane are reduced. This could be attributed to the reduction of the height of the reflected surface slope error cone.

**Figure B.6:** Flux profiles for various surface slope errors and incidence angles

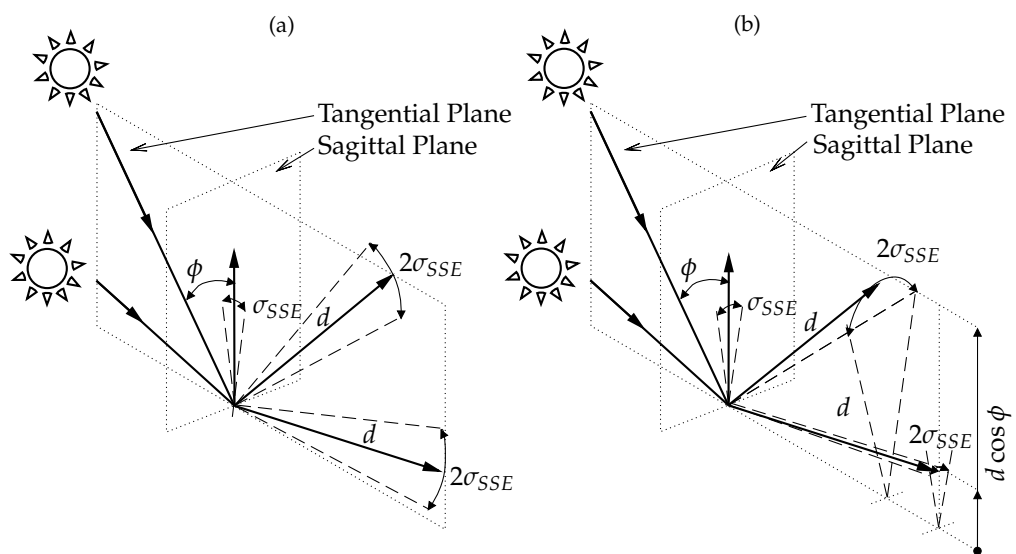


**Figure B.7:** Image size for the tangential plane (a) and the sagittal plane (b) at small and large incidence angles (Courtesy of Landman *et al.*, 2014)

## Appendix C

# Tracking methods

Three tracking methods are included in the aiming strategy simulation model: azimuth elevation, fixed horizontal and target aligned tracking. For consistency throughout this thesis, only the azimuth elevation tracking method was used in the aiming strategy simulations. The following section provides details on these tracking methods.

### C.1 Azimuth elevation tracking

The most common tracking method is the azimuth elevation method (Guo *et al.*, 2011). The primary (azimuth) axis is a fixed axis in the vertical position as shown in Figure C.1. Generally this axis allows rotation around the heliostat pylon. The secondary (elevation) axis is perpendicular to the primary axis and parallel to the reflective surface. This type of tracking mechanism allows ground coverage by the reflective area at a maximum of 58% in order to avoid collision of the heliostats during operation (Schramek and Mills). Schramek and Mills suggest a tracking method where the horizontal axis is fixed. This method, known as fixed horizontal tracking, is able to cover a maximum of 76% of the ground. The method is to be discussed in the following section.

### C.2 Fixed horizontal tracking

In fixed horizontal tracking, primary rotation occurs around a horizontal axis (Figure C.2). Secondary rotation occurs around the axis perpendicular to the primary axis. Besides the lowered risk of collision, the ability to integrate with linear drives is also an advantage of this method.

### C.3 Target aligned tracking

The primary axis in target aligned tracking is pointed towards the centre of the target as seen in Figure C.3. The secondary rotation occurs around the axis perpendicular to the primary axis and parallel to the mirror surface. The positions of the axes allow the heliostat normal to move within the tangential plane (Chen *et al.*, 2004).

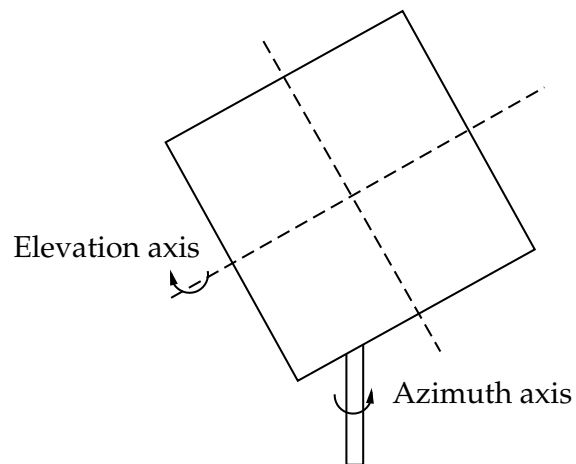


**Figure C.1:** Azimuth elevation rotational axes

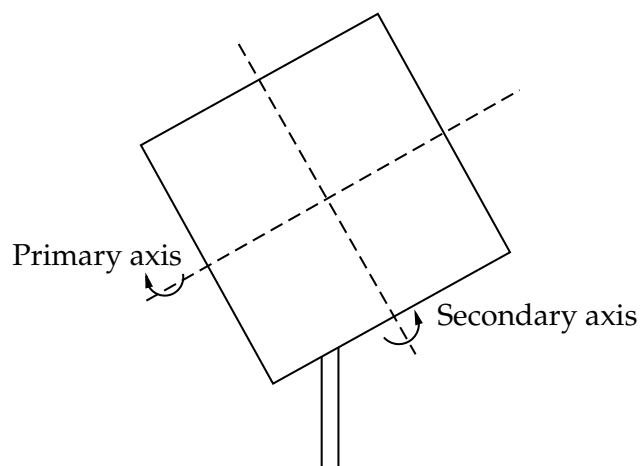


**Figure C.2:** Fixed horizontal rotation axes

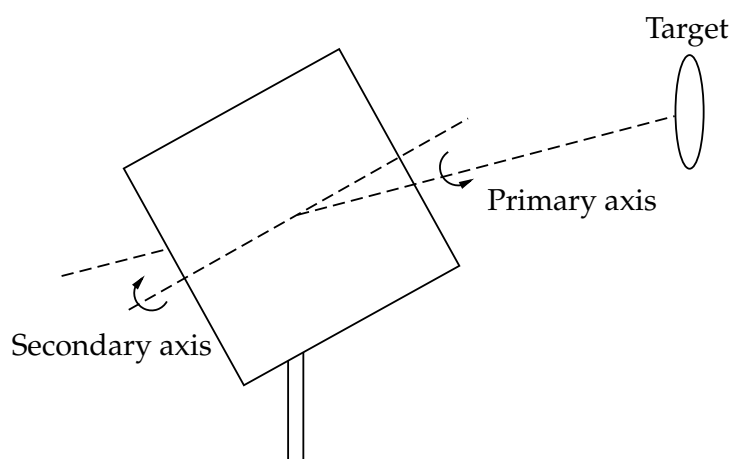


**Figure C.3:** Target aligned rotational axes

# List of References

- Ahlbrink, N., Andersson, J., Diehl, M. and Pitz-Paal, R. (2010a). Optimized operation of an open volumetric air receiver. *Proceedings of the 16th SolarPACES conference, September 2010, Perpignan, France.*
- Ahlbrink, N., Belhomme, B., Flesch, R., Quinto, D.M., Rong, A. and Schwarzbözl, P. (2010b). STRAL: Fast ray tracing software with tool coupling capabilities for high-precision simulations of solar thermal power plants. *Proceedings of the 16th SolarPACES conference, September 2010, Perpignan, France.*
- Anon. (2008). An industry report on solar thermal energy. Available at: [www.solar-thermal.com](http://www.solar-thermal.com)
- Arora, J.S. (2012). *Introduction to optimum design*. 3rd edn. Academic press, Oxford.
- Augsburger, G. (2013). *Thermo-economic optimisation of large solar tower power plants*. Ph.D. thesis, École polytechnique fédérale de Lausanne.
- Augsburger, G. and Favrat, D. (2013). Modelling of the receiver transient flux distribution due to cloud passages on a solar tower thermal power plant. *Solar Energy*, vol. 87, pp. 42–52.
- Barbir, F., Veziroglu, T. and Plass, H. (1990). Environmental damage due to fossil fuels use. *International Journal of Hydrogen*, vol. 15, no. 10, pp. 739–749.
- Barlev, D., Vidu, R. and Stroeve, P. (2011). Innovation in concentrated solar power. *Solar Energy Materials and Solar Cells*, vol. 95, no. 10, pp. 2703–2725.
- Behar, O., Khellaf, A. and Mohammedi, K. (2013). A review of studies on central receiver solar thermal power plants. *Renewable and Sustainable Energy Reviews*, vol. 23, pp. 12–39.
- Belhomme, B., Pitz-Paal, R. and Schwarzbözl, P. (2013). Optimization of heliostat aim point selection for central receiver systems based on the ant colony optimization metaheuristic. *Journal of Solar Energy Engineering*, vol. 136, no. 1, p. 011005. ISSN 0199-6231.
- Belhomme, B., Pitz-Paal, R., Schwarzbözl, P. and Ulmer, S. (2009). A New Fast Ray Tracing Tool for High-Precision Simulation of Heliostat Fields. *Journal of Solar Energy Engineering*, vol. 131, no. 3, p. 031002.
- Berenguel, M., Rubio, F., Valverde, A., Lara, P., Arahall, M., Camacho, E. and López, M. (2004). An artificial vision-based control system for automatic heliostat positioning offset correction in a central receiver solar power plant. *Solar Energy*, vol. 76, no. 5, pp. 563–575.
- Besarati, S.M., Goswami, D.Y. and Stefanakos, E.K. (2014). Optimal heliostat aiming strategy for uniform distribution of heat flux on the receiver of a solar power tower plant. *Energy Conversion and Management*, vol. 84, pp. 234–243.

- Biggs, F. and Vittitoe, C.N. (1979). Helios model for the optical behavior of reflecting solar concentrators. *NASA STI/Recon Technical Report N*.
- Bland, J.A. (1993). Nonlinear optimization of constrained functions using tabu search. *International Journal of Mathematical Education in Science and Technology*, vol. 24, no. 5, pp. 741–747.
- Bobinecz, M. (2012). Ivanpah solar electric generating facility. *Proceedings of Engineering and construction contracting conference, September 2012, San Antonio, Texas*.
- Bode, S.J. and Gauché, P. (2013). Review of optical software for use in concentrating solar power systems. *Proceedings 1st Southern African Solar Energy Conference, May 2013, Stellenbosch, South Africa*, pp. 1–8.
- Boese, F.K., Merkel, A., Stahl, D. and Stehle, H. (1981). A consideration of possible receiver designs for solar tower plants. *Solar Energy*, vol. 26, no. 1, pp. 1–7.
- Braun, K.P. (1996). HELIOS: Simulation of the incident flux distribution of the TSA receiver. *Internal report, PSA*.
- BrightSource (2013). Ivanpah updates.  
Available at: [www.ivanpahsolar.com](http://www.ivanpahsolar.com)
- Buie, D. (2000). Flux Distributions on a Linear Absorber. In: *ANZSES Solar 2000 Conference*, pp. 1–7. Brisbane, Australia.
- Buie, D., Monger, A.G. and Dey, C.J. (2003). Sunshape distributions for terrestrial solar simulations. *Solar Energy*, vol. 74, pp. 113–122.
- Burke, E. and Kendall, G. (2005). *Introductory tutorials in optimisation, decision support and search methodology*. Springer, Montreal, Canada.
- Chen, Y.T., Kribus, A., Lim, B.H., Lim, C.S., Chong, K.K., Karni, J., Buck, R., Pfahl, A. and Bligh, T.P. (2004). Comparison of two sun tracking methods in the application of a heliostat field. *Journal of Solar Energy Engineering*, vol. 126, no. 1, p. 638.
- Collado, F.J. (2010). One-point fitting of the flux density produced by a heliostat. *Solar Energy*, vol. 84, no. 4, pp. 673–684.
- Collado, F.J., Gomez, A. and Turégano, J.A. (1986). An analytic function for the flux density due to sunlight reflected from a heliostat. *Solar Energy*, vol. 37, no. 3, pp. 215–234.
- de Berg, M., van Kreveld, M. and Overmars, M. (2008). Delaunay triangulation. In: *Computational Geometry: Algorithms and Applications, 2000*, 3rd edn, chap. 9, pp. 191–218. Springer-Verlag, New York.
- Denholm, P. and Hummon, M. (). Simulating the value of concentrating solar power with thermal energy storage in a production cost model. Tech. Rep..
- Djafer, D., Thuillier, G. and Sofia, S. (2008). A comparison among solar diameter measurements carried out from the ground and outside earth's atmosphere. *The Astrophysical Journal*, vol. 676, pp. 651–657.
- Dorigo, M. and Gambardella, L. (1997). Ant colony system: a cooperative learning approach to the travelling salesman problem. *Evolutionary Computation, IEEE*, vol. 1, no. 1, pp. 53–66.

- Dorigo, M. and Stützle, T. (2004). *Ant colony optimization*. The MIT Press, Cambridge, Massachusetts.
- Escobar-Toledo, M., Arancibia-Bulnes, C., Peña-Cruz, M., Riveros-Rosas, D., Cabanillas, R. and Estrada, C. (2012). Analysis of heliostat image drift. In: *Proceedings of the 18th SolarPACES conference, September 2012, Marrakesh, Morocco*.
- Fleet, R. (2013). Glows, bows and haloes.  
Available at: <http://www.dewbow.co.uk/index.html>
- Gallego, A.J., Fele, F. and Camacho, E.F. (2014). On the optimization of irradiance distribution in solar tower plants with flat receivers. *Proceedings of the European Control Conference (ECC)*, pp. 2496–2501.
- Garcia, P., Ferriere, A. and Bezia, J. (2008). Codes for solar flux calculation dedicated to central receiver system applications: A comparative review. *Solar Energy*, vol. 82, no. 3, pp. 189–197.
- García-Martín, F., Berenguel, M., Valverde, A. and Camacho, E. (1999). Heuristic knowledge-based heliostat field control for the optimization of the temperature distribution in a volumetric receiver. *Solar Energy*, vol. 66, no. 5, pp. 355–369.
- Glover, F. (1986). Future paths for integer programming and links to artificial intelligence. *Computers & Operations Research*, vol. 13, pp. 533–549.
- Goldberg, D. and Holland, J. (1988). Genetic algorithms and machine learning. *Machine learning*, vol. 3, no. 2-3, pp. 95–99.
- Grobler, A. and Gauché, P. (2014). A review of aiming strategies for central receivers. *Proceedings of the 2nd SASEC conference, January 2014, Port Elizabeth, South Africa*.
- Guo, M. and Wang, Z. (2011). On the analysis of an elliptical Gaussian flux image and its equivalent circular Gaussian flux images. *Solar Energy*, vol. 85, no. 5, pp. 1144–1163.
- Guo, M., Wang, Z., Zhang, J., Sun, F. and Zhang, X. (2011). Accurate altitude-azimuth tracking angle formulas for a heliostat with mirror-pivot offset and other fixed geometrical errors. *Solar Energy*, vol. 85, no. 5, pp. 1091–1100.
- Ho, C. and Iverson, B. (2012). Review of central receiver designs for high-temperature power cycles. *Proceedings of the 18th annual SolarPACES conference, September 2012, Marrakesh, Morocco*.
- Igel, E.A. and Hughes, R.L. (). Optical analysis of solar facility heliostats. *Solar Energy*, vol. 22, pp. 283–295.
- Intergovernmental panel on climate change (2011). IPCC Special report on renewable energy sources and climate change mitigation. Tech. Rep., Cambridge, UK and New York, USA.  
Available at: <http://srren.ipcc-wg3.de/report>
- IRENA (2012). Renewable energy technologies: cost analysis series. Volume 1: Power sector issue 2/5, Concentrating solar power. Tech. Rep., IRENA.  
Available at: [www.irena.org/Publications](http://www.irena.org/Publications)
- Kelly, B.D. (2010). Advanced thermal storage for central receivers with supercritical coolants. Tech. Rep., Abengoa Solar Inc.  
Available at: <http://www.osti.gov/scitech/biblio/981926>

- Kolb, G.J., Ho, C.K., Mancini, T.R. and Gary, J.A. (2011). Power tower technology roadmap and cost reduction plan. Tech. Rep., Sandia National Laboratories (SNL), Albuquerque, NM, and Livermore, CA, USA.  
Available at: <http://www.osti.gov/servlets>
- Kolb, G.J., Jones, S.A., Donnelly, M.W., Gorman, D., Thomas, R., Davenport, R. and Lumia, R. (2007). Heliostat cost reduction study. Tech. Rep., Sandia National Laboratories.  
Available at: <http://www.osti.gov/bridge>
- Koretz, B. (2014). Solar field layout and aiming strategy.
- Landman, W. (2013). Correspondence.
- Landman, W., Grobler, A., Gauché, P. and Dinter, F. (2014). Limitations of assuming a circular Gaussian flux density distribution for a single heliostat image. *Journal of Solar Energy Engineering*.
- Lata, J.M., Rodríguez, M. and de Lara, M.A. (2008). High flux central receivers of molten salts for the new generation of commercial stand-alone solar power plants. *Journal of Solar Energy Engineering*, vol. 130, no. 2.
- Liao, Z., Li, X., Xu, C., Chang, C. and Wang, Z. (2014). Allowable flux density on a solar central receiver. *Renewable Energy*, vol. 62, pp. 747–753.
- Lovegrove, K. and Stein, W. (2012). *Concentrating solar power technology principles, development and applications*. Woodhead publishing Ltd, Cambridge.
- Noring, J., Grether, D. and Hunt, A. (1991). Circumsolar radiation data: the Lawrence Berkeley Laboratory reduced data base.  
Available at: <http://rredc.nrel.gov/solar/pubs/circumsolar/title.html>
- Pettit, R., Vittitoe, C.N. and Biggs, F. (1983). Simplified calculational procedure for determining the amount of intercepted sunlight in an imaging. *Journal of Solar Energy Engineering*, vol. 105, pp. 101–107.
- Pitz-Paal, R., Dersch, J. and Milow, B. (2005). European concentrated solar thermal roadmapping (ECOSTAR): roadmap document.
- Raponi, A., de Bernardis, P. and Sigismondi, C. (2011). *The measurement of solar diameter and limb darkening function with the eclipse observations*. Ph.D. thesis, Università de Roma.
- Reda, I. and Andreas, A. (2004). Solar position algorithm for solar radiation applications. Tech. Rep..
- Rodríguez-Sánchez, M., Venegas-Bernal, M., Marugán-Cruz, C. and Santana, D. (2013). Thermal, mechanical and hydrodynamic analysis to optimize the design of molten salt central receivers of solar tower power plants. *Proceedings of the International Conference on Renewable Energies and Power Quality, March 2013, Bilbao, Spain*.
- Romero, M., Buck, R. and Pacheco, J.E. (2002). An update on solar central receiver systems, projects, and technologies. *Journal of Solar Energy Engineering*, vol. 124, no. 2, p. 98.
- Salomé, A., Chhel, F., Flamant, G., Ferrière, A. and Thiery, F. (2013). Control of the flux distribution on a solar tower receiver using an optimized aiming point strategy: Application to THEMIS solar tower. *Solar Energy*, vol. 94, pp. 352–366.
- Schmitz, M., Schwarzbözl, P., Buck, R. and Pitz-Paal, R. (2006). Assessment of the potential improvement due to multiple apertures in central receiver systems with secondary concentrators. *Solar Energy*, vol. 80, no. 1, pp. 111–120.

- Schramek, P. and Mills, D.R. (). Heliostats for maximum ground coverage. *Proceedings of the 15th SolarPACES conference, September, Berlin, Germany*, , no. 2004, pp. 701–713.
- Schwarzbözl, P., Pitz-Paal, R. and Schmitz, M. (2009). Visual HFLCAL - A Software Tool for Layout and Optimisation of Heliostat Fields. *Proceedings of the 15th SolarPACES conference, September 2009, Berlin, Germany*.
- Stine, W. and Geyer, M. (2001). Power from the sun.  
Available at: [www.powerfromthesun.net/book](http://www.powerfromthesun.net/book)
- The CSP Alliance (2012). The economic and reliability benefits of CSP with thermal energy storage: Recent studies and research needs. Tech. Rep..  
Available at: <http://www.csp-alliance.org/cspa-report/>
- The Mathworks Inc. (2014). Matlab 2014.
- Tyner, C., Sutherland, J. and Gould, W. (1995). Solar two: A molten salt power tower demonstration. *VDI BERICHTE*, pp. 53–53.
- US Energy Information Administration (2011). International energy outlook 2011.  
Available at: [www.eia.gov](http://www.eia.gov)
- Vant-Hull, L.L. (2002). The role of allowable flux density in the design and operation of molten-salt solar central receivers. *Journal of Solar Energy Engineering*, vol. 124, no. 2, p. 165.
- Wendelin, T., Dobos, A. and Lewandowski, A. (2013). SolTrace: A Ray-Tracing Code for Complex Solar Optical Systems.  
Available at: <http://www.nrel.gov/docs/fy14osti/59163.pdf>
- Wendelin, T., Lewandowski, A. and Dobos, A. (2012). SolTrace.  
Available at: <http://www.nrel.gov/csp/soltrace/>
- World Bank (2012). Turn down the heat: why a 4°C warmer world must be avoided. Tech. Rep., Potsdam Institute for Climate Impact Research and Climate Analysis, Washington DC, USA.  
Available at: <http://documents.worldbank.org>
- Zavoico, A. (2001). Solar power tower design basis document. Tech. Rep., Sandia National Laboratories, San Francisco, USA.